Process Modeling of Ultrasonic Additive Manufacturing

Dissertation

Presented in Partial Fulfillment of the Requirements for the Degree
Doctor of Philosophy in the Graduate School of The Ohio State
University

By

Gowtham Venkatraman, B.S., M.S.

Graduate Program in Mechanical Engineering

The Ohio State University

2022

Dissertation Committee:

Professor Marcelo J. Dapino, Advisor

Professor Amos Gilat

Professor Antonio Ramirez

Professor Hanna Cho

© Copyright by

Gowtham Venkatraman

2022

Abstract

Ultrasonic additive manufacturing (UAM) is an additive manufacturing technology which combines ultrasonic metal welding, CNC machining, and mechanized foil layering to create large gapless near net-shape metallic parts in solid state. Its integration with subtractive processes enables the creation of complex design features such as heat exchangers. The low formation temperature of the UAM process allows the integration of temperature−sensitive components, smart materials, cooling channels, organic polymers, and electronics into metal matrices. UAM is currently limited to niche applications, as resource-intensive trials are required to evaluate the feasibility of joining new material combinations due to a lack of process models in the literature with predictive ability to establish process-property relationships. The key thrusts of this research are to characterize the energy flow in the UAM process, investigate the role of cold working and friction on UAM bond strength, and develop an energy-based model for process-property relationships of UAM builds. Analytical and finite element (FE) models are used to describe the state of stress under plastic deformation in UAM. An empirical model is developed between the estimated energy of plastic deformation, a driver of bond quality in UAM, and the measured strength of the weld interface in shear. In-situ measurements are conducted using a Doppler velocimetry to monitor the in-situ vibration dynamics of the foil during UAM and to characterize energy losses associated with friction. Each objective is accompanied by analytical, finite element, or experimental findings to aid and supplement the effort.

Intellectual merit: A framework for modeling the flow of energy in the UAM process from the input electrical energy to the weld interface microstructure is developed. This framework enables the development of process-property relationships for UAM. This is also used to develop a figure of merit which can be used to optimize the different components of the UAM process to reduce wasted energy not used for bond formation. In-situ process monitoring systems are also developed to enable quality monitoring and closed-loop process control. This work is expected to dramatically improve the attractiveness and adoption of the UAM process for structural light-weighting applications in the aerospace and automobile industries by improving process predictability and consistency. The development of a quantitative understanding of the role of system compliance on weld power and part strength empowers improved fixture and workpiece design for improved UAM part quality. Analysis techniques novel to the field of UAM were used to quantify the energy storage in the weld microstructure. A calibrated thermal model was built that is capable of predicting the weld temperatures as a function of weld parameters, which reduces trial-and-error in the design of process parameters to embed temperature-sensitive materials in metal matrices using UAM.

This is dedicated to my parents.

Acknowledgments

I would like to thank my advisor, Prof. Marcelo Dapino, for his continuous mentorship, support, and guidance to navigate my research journey towards my dissertation. He provided me with multiple opportunities to improve my professional and communication skills by presenting at international conferences, work directly with industry research teams, teach, and review academic publications. I would also like to thank Prof. Amos Gilat, Prof. Hannah Cho, and Prof. Antonio Ramirez for serving on my committee. Their insightful questions and guidance helped me shape my dissertation work.

I am very grateful for Dr. Ryan Hahnlen for his mentorship and technical expertise to help direct the thrust this project. I also thank the team at Battelle for a great research collaboration experience - especially Dr. Steven Risser and Melissa Roshon. I would also like to acknowledge Prof. Xun Liu and Umair Shah for supplying the infrared camera used for thermal measurements and supporting the thermal modeling effort.

In addition, I would like to thank my colleagues in the Smart Materials and Structures Lab. Dr. Leon Headings was a constant source of technical knowledge, advice, and critical feedback that has improved the quality of my work. He also greatly helped me improve my attention-to-detail in manuscripts, presentations, and reports. In particular, I would like to thank Dr. Tyler (Tianyang) Han, Dr. Hatcher

(Hongqi) Guo, Dr. Adam Hehr, Dr. Venkata Siva Chillara, Bryant Gingerich, Dr. Arun Ramanathan, Dr. Sai Vemula, Ninxinger Zhao, Sean Chilelli, Vivek Srinivas, and Ismail Nas for their help and support in being a great team to bounce ideas off of. I would also like to thank Ms. Tommie Blackledge and graduate advisor Nick Breckenridge. Special thanks to the MAE and MSE departments staff who provided substantial technical support for the experimental studies in this endeavor.

I would also like to thank my Amma's patient and kind words and Appa's trust that have kept me going. I also leaned a lot on my most supportive friends - Kadambari, Venkatesh, Dr. Shanmugam, Kamalnath, Jo and Kat, and more who buoyed me up constantly. Thanks Hazel for our little infinity. I would finally like to thank all my teachers - especially Ms. Sridevi and Nataraj Ponnusamy from high school for building the foundations of my academic passion by going the extra mile.

Vita

July 19, 1994	Born - Trichy, India
June 2015	B.Tech. (Hons) Mechanical Engineering, Indian Institute of Technology Madras, Chennai, Tamilnadu, India.
June 2015 - Jul 2020	Graduate Research Associate, Smart Materials and Structures Lab, The Ohio State University, USA.
Aug 2020 - Dec 2020	Graduate Teaching Associate, Mechanical and Aerospace Engineering, The Ohio State University, USA.
Jan 2021 - Dec 2021	Graduate Research Associate, Smart Materials and Structures Lab, The Ohio State University, USA.

Publications

G. VENKATRAMAN, A. Hehr, L.M. Headings, and M.J. Dapino. “Effect of system compliance on weld power in ultrasonic additive manufacturing” Rapid Prototyping Journal, Vol. 27, No. 9, pp. 1650-1663, 2021.

G. VENKATRAMAN, L.M. Headings, and M.J. Dapino. “In-situ Investigation of Deformation Dynamics for Quality Monitoring in Ultrasonic Additive Manufacturing”, 18th International Conference on the Strength of Materials, Columbus, Ohio, 2018.

G. VENKATRAMAN, L.M. Headings, and M.J. Dapino. “Multiphysics Modeling of Ultrasonic Additive Manufacturing”, OSU Materials Week, Columbus, Ohio, 2020.

G. VENKATRAMAN, L.M. Headings, and M.J. Dapino. “In-situ quality monitoring of high-power Ultrasonic Additive Manufacturing (UAM) using scanning Doppler vibrometry”, IEEE International Ultrasonics Symposium, virtual, 2021.

G. VENKATRAMAN, U. Shah, X. Liu, and M.J. Dapino. “In-situ IR imaging for modeling heat transfer in the ultrasonic additive manufacturing process”, Journal of Materials Processing Technology, in preparation.

Fields of Study

Major Field: Mechanical Engineering

Studies in:

Smart materials and structures
Dynamical systems
Ultrasonic additive manufacturing

Table of Contents

Page

Abstract ii

Dedication iv

Acknowledgments v

Vita vii

List of Tables xii

List of Figures xiii

1. **Introduction** 1

    1.1 Background 1
    1.2 Problem statement and research objectives 6
    1.3 Dissertation organization 7

2. **Effect of System Compliance on Weld Power in Ultrasonic Additive Manufacturing** 9

    2.1 Introduction 10
    2.2 Model for dynamic load stiffness and weld power in UAM 13
    2.3 Lumped parameter modeling of dynamic load stiffness 16
        2.3.1 Equivalent circuit analysis 16
        2.3.2 Weld power - stiffness relationships 19
    2.4 Estimation of LTI model parameters 21
        2.4.1 Estimation of vacuum chuck stiffness 21
        2.4.2 Estimation of system stiffness using FEM 24
    2.5 Experiments for validating weld power model 25
        2.5.1 Study A: Effect of baseplate stiffness on weld power 26

2.5.2 Study B: Effect of foil material stiffness on weld power . . . 33
2.5.3 Study C: Effect of foil material on model damping parameter 36
2.6 Conclusions 43

3. **In-situ Measurements for Quality Monitoring and Process Control** 45

3.1 Introduction 46
3.2 Measurement setup 47
3.2.1 In-situ electrical measurements 47
3.2.2 In-situ Doppler velocimetry 48
3.3 Weld quality assessment using Doppler velocimetry 51
3.4 Conclusions 56

4. **Investigation of Microstructural Energy Storage using EBSD and Hardness Testing** 59

4.1 Introduction 60
4.2 Electron backscatter diffraction (EBSD) and Nanoindentation analysis 62
4.2.1 EBSD technique 62
4.2.2 Quantitative analysis 62
4.2.3 Weld interface identification 65
4.2.4 Nanoindentation for interface identification 67
4.3 Estimation of energy storage in the microstructure 69
4.3.1 Study A: Effect of subsequent weld layers 69
4.3.2 Study B: Effect of process settings 74
4.4 Conclusions 81

5. **Influence of Surface Roughness in UAM** 83

5.1 Introduction 84
5.2 Surface roughness measurements using optical profilometry 86
5.3 Roughness transfer experiments 88
5.4 In-plane shear strength measurements 90
5.5 Conclusions 95

6. **Energy-based Process Model for UAM with Temperature-dependent Plasticity** 96

6.1 Introduction 97
6.2 Analytical model development 99
6.2.1 Modeling assumptions 99
6.2.2 Model for plastic deformation energy 101
6.2.3 Model for frictional dissipation energy 108

6.3 Thermal model 109
    6.3.1 Transient thermal finite element model 110
    6.3.2 Parametric study using FE model - effect of weld speed . . 112
    6.3.3 IR Experiments and data analysis 115
    6.3.4 Model validation 117
6.4 Process-property relationships for the UAM of Aluminum 121
6.5 Energy flow map for the UAM of aluminum 123
6.6 Conclusions 125

7. **Conclusions and Future Work** 127

7.1 Summary of findings 127
7.2 Contributions 131
7.3 Future work 132

Appendices 135

A. **Energy required to disperse the oxide layer** 135

B. **Temperature-dependent flow stress of Al 6061-H18 foil** 137

C. **Calibration of infrared emissivity of the welder surface** 139

Bibliography 141

List of Tables

Table **Page**

2.1 UAM weld parameters for welding Al 6061-H18 foil onto aluminum and steel baseplates. 28

2.2 UAM weld parameters for welding 10 layers of Cu C11000-O60 on an aluminum baseplate. 33

2.3 Summary of foil tensile properties. 36

2.4 Influence of foil and baseplate material on effective system stiffness (K_{system}) for 2 layers of foil welded onto a 9.53 mm (0.375 in) thick Al 6061-T6 baseplate. Stiffness units are (MN/m). 37

2.5 UAM weld parameters for welding the second layer of all foil types with an Al 6061-T6 baseplate. 37

3.1 Signals measured using the NI cDAQ 9178. 49

4.1 Summary of the welding trials. 73

6.1 Summary of thermal properties used for the transient thermal finite element (FE) analysis using COMSOL. 110

B.1 Summary of temperature-dependent yield strength of as-received Al 6061-H18 foil. 138

List of Figures

Figure **Page**

1.1 Fabrisonic 9 kW SonicLayer 4000 ultrasonic additive manufacturing system: (a) the ultrasonic welder is used to additively join foils together on a vacuum chuck fixture; (b) the subtractive CNC stage is used to introduce complex internal features and to trim components. The two Dukane ultrasonic transducers are each rated to 4.5 kW. The solid blue downward arrow represents the normal force applied during welding (weld force) and the hollow red side-to-side arrow represents the vibratory scrubbing action. 2

1.2 The relationship between deformation reduction and the strength of the resulting bond shown for cold roll bonding, a room-temperature solid-state joining process by rolling two foils together using rollers, reproduced from [1]. 4

2.1 UAM stack and system dynamics: (a) schematic illustration of the components that contribute to the mechanical compliance of the system; (b) equivalent circuit representation of the system. The weld zone deformation is modeled using a viscous damping element. 16

2.2 The first mode of vibration in shear of a 20-layer Al stack and 9.53 mm (0.375 in) thick Al baseplate in shear is identified using the eigenfrequency solver within COMSOL to be 70.4 kHz, which is well above the 20 kHz excitation frequency. The color scale represents the normalized total displacement. 19

2.3 Setup for modal hammer testing of the vacuum chuck anvil structure using a 9.53 mm (0.375 in) thick Al 6061-T6 baseplate. This test is used to measure the dynamic stiffness of the structure with impacts on the vacuum chuck. 22

2.4 Dynamic transfer mechanical stiffness of the vacuum chuck with respect to a baseplate constrained to the vacuum chuck shown for aluminum and steel baseplates. Frequency response functions were measured by striking a modal hammer on the vacuum chuck and measuring the response using accelerometers on the vacuum chuck and the baseplate. 23

2.5 FE model of stack and baseplate: (a) Contact surface used to apply load from the weld tool. Normal (-z) and transverse (y) static loads are applied as traction loads on the contact surface. (b) Mesh density of FE model. A graded mesh was utilized near the contact surface to improve accuracy of the simulated stack deformation. 25

2.6 FE simulation of the UAM stack displacement for: (a) 2-layer and (b) 20-layer Al 6061-H18 stacks on a 9.53 mm (0.375 in) thick Al 6061-T6 baseplate with simulated K_{system}=433 MN/m and 364 MN/m, respectively; (c) 2-layer and (d) 20-layer Al 6061-H18 stacks on a 3.18 mm (0.125 in) thick annealed AISI 4130 steel baseplate with simulated K_{system}=772 MN/m and 455 MN/m, respectively. 28

2.7 Comparison of in-situ measurements for welding the second layer of Al 6061-H18 foil with a 3.18 mm (0.125 in) thick annealed AISI 4130 steel baseplate versus a 9.53 mm (0.375 in) thick Al 6061-T6 baseplate. The peak force (welder shear force) is estimated from the weld power and welder's vibration velocity measurements using the LTI model of the weld assembly. The steel baseplate weld required greater power to achieve the prescribed welder vibration amplitude. 30

2.8 Trends in weld power and stiffness with build height for the welding of Al 6061-H18 foil: (a) measured average electric power; (b) simulated effective stiffness K_{system} from (2.15) based on FE modeled stiffness of the stack and baseplate. 31

2.9 Experimentally measured average electric power plotted against the system stiffness estimated from the model for a 0.9 mm contact width. Data points for each baseplate are calculated from welds on consecutive layers, with progressively decreasing stiffness with build height. The non-linear model uses (2.11) and the linearized model uses (2.12) to estimate the average electric power, with parameter D_{loss} determined to be 6100 N.s/m from weld power data while welding the second Al 6061-H18 layer on the aluminum baseplate. The vertical lines show the range of system stiffness values expected for foil−foil welding using our welding setup. 32

2.10 Ten-layer stack of Cu C11000-O60 foil welded onto a 9.53 mm (0.375 in) thick Al 6061-T6 baseplate. 34

2.11 Weld power and system stiffness values for welding 10 layers of 0.152 mm (0.006 in) thick C11000-O60 foils onto a 9.53 mm (0.375 in) thick Al 6061-T6 baseplate: (a) simulated effective stiffness K_{system} from (2.15) based on FE modeled stiffness of the stack and baseplate; (b) measured average electric power compared against predictions from the weld power model in (2.11). 35

2.12 Measurements during welding of different metal foil types onto one another, i.e., foil−foil results, as well as the reference no welding condition. The first foil was welded onto a 9.53 mm (0.375 in) thick Al 6061-T6 baseplate. The power, peak velocity, frequency, and peak shear force profiles are similar in magnitude for all of the foil types. The welder frequency estimates for Al 6061-H18 and Cu C11000-O60 data overlap. Measurements are shown in the steady-state regions of the welds (at least 12.7 mm (0.5 in) away from start and end of each weld). 38

2.13 Welded foils along with ultimate tensile strength (UTS) for reference. Two layers of each material were welded onto a 9.53 mm (0.375 in) thick Al 6061-T6 baseplate. Welds using a 32 μm peak-peak weld amplitude setpoint are shown here. 40

2.14 Measurements for attempting welding of different metal foil types onto one another, i.e., foil−foil results for welding the second foil to the first foil, as well as the no welding (actuated in air) condition for reference over a range of peak-peak weld amplitude setpoints. Model predictions are computed using the system stiffnesses of Al and Cu builds from Table 2.4 in (2.11). (a) Average electric power calculated by averaging the power measurements in the steady-state region of the weld (at least 12.7 mm (0.5 in) away from both the start and end of the weld). (b) Peak velocity of the vibration of the welder during welding and in air (no welding). The regression line between the peak velocity data in the no-welding cases and welding all the foils is shown. The least squares estimate of the slope value is 0.77, with an R-squared value of 98%. . 41

3.1 Measurement setup: (a) Weld power, weld speed, weld force, voltage, and current to the transducers are acquired using National Instruments cDAQ-9178 for in-situ process measurements; (b) LabVIEW program used for storing the collected data on a Windows PC. 47

3.2 Focused image of welder and foil before welding taken with a macro lens and lighting system. The welder is applying the set weld normal force on the baseplate. The baseplate is machine flat and hence has a mirroring effect in the image. The zoomed image shows the laser spot completely positioned within the foil. 50

3.3 Representative data for a Al 6061-H18 foil-foil weld using the following weld parameters: 32 µm weld amplitude, 5000 N weld force, 84.67 mm/s (200 in/min) weld speed. The velocity plots on the right show that the foil vibration velocity is also a sinusoidal signal with some noise artifacts due to issues maintaining focus on the foil. 51

3.4 A Polytec PSV-400 scanning vibrometer is used to measure the velocity profile of the foils being welded using UAM. A grid of points are defined in the Polytec software, and the laser spot sequentially measures the vibration velocity at the given location. 52

3.5 Different slip regimes identified during the welding of Al 6061-H18 welded onto an Al 6061-T6 baseplate: (a) illustration of the welded zone (bottom surface of the foil being welded sticks to the workpiece), slip zone (the foil-foil interface has a constant slip velocity), and the transition zone in-between for a successful weld; (b) the three zones marked on a plot of the velocity profile for a successful weld (32 μm weld amplitude, 5000 N weld force, 84.67 mm/s (200 in/min) weld speed); (c) the velocity profile of an unsuccessful weld with insufficient weld amplitude (12 μm weld amplitude, 5000 N weld force, 84.67 mm/s (200 in/min) weld speed) where the entire contact region is the slip zone. 53

3.6 The velocity of the foil being welded at different positions: (a) welded zone; (b) transition zone; and (c) slip zone, as defined in Figure 3.5. The velocity of the foil in the slip zone approaches that of the welder, whereas that in the welded zone is non-sinusoidal and has higher harmonics, indicating non-linear stick/slip behavior. 54

3.7 Normalized velocity profile for different weld amplitudes for the UAM of: (a) Al 6061-H18, (b) Cu C11000-O60. (c) Metric θ defined in (3.1) to quantify the degree of asymmetry in the foil velocity profile. 56

3.8 Algorithm for parameter search using the weld quality detection technique identified in Figure 3.5. 58

4.1 Using a cutoff angle θ_m of 15 degrees, low (LAGB) and high (HAGB) angle boundaries can be distinguished. HAGBs are shown in red and LAGBs in black. The minimum threshold size for a grain is 2 pixels. The UAM interface is seen near the top as a collection of dense HAGBs. 63

4.2 The un-smoothed inverse pole figure (IPF) shows the point-by-point orientation of the sample. The 2-layer Al 6061-H18 sample was fabricated on an Al 6061-T6 baseplate using the following settings: 29 μm weld amplitude, 5000 N weld force, and 84.67 mm/s (200 in/min) weld speed. Black regions are areas that did not provide a high-confidence data fit. The different colors denote the different orientations of each pixel. 64

4.3 Interface location identified with a red cross using the location of the minimum of the fraction of unindexed points. 66

4.4 Measurement of local hardness of UAM-welded Al 6061-H18: (a) MTS Nano Indenter XP with a Berkovich indenter used to perform nanoindentation; (b) map of local hardness measured with a spacing of 5 µm; (c) Inverse Pole Figure (IPF) from EBSD analysis of a UAM weld with the weld interface region shown using dashed white lines. 67

4.5 Samples fabricated with 2, 3, 5, and 10 layers of Al 6061-H18 foil UAM-ed on a 12.7 mm (0.5 inch) thick Al 6061-T6 baseplate to study the effect of subsequent weld layers on the weld interface microstructure. 69

4.6 Optical images of (a) 2-, (b) 3-, (c) 5-, and (d) 10-layer Al 6061-H18 welds constructed on a 12.7 mm (0.5 inch) thick Al 6061-T6 baseplate using weld parameters: 32 µm welder amplitude, 5000 N weld force, and 84.67 mm/s (200 in/min) weld speed. 70

4.7 Inverse pole figures of (a) 2-, (b) 3-, (c) 5-, and (d) 10-layer Al 6061-H18 welds constructed on a 12.7 mm (0.5 inch) thick Al 6061-T6 baseplate using weld parameters: 32 µm welder amplitude, 5000 N weld force and 84.67 mm/s (200 in/min) weld speed. The centerpoint of the interface was identified from Figure 4.3, and the approximate weld interface region is shown using dotted white lines. 71

4.8 Analysis of the size distribution of grains in the 2-, 3-, 5-, and 10-layer samples: (a) Histogram of the area of the grains vs. the grain size near the weld interface; (b) Mean grain size near the foil 1 - foil 2 weld interface plotted vs. the total number of layers welded. 72

4.9 Analysis of the misorientation angle distribution of grains in the 2-, 3-, 5-, and 10-layer samples: (a) Histogram of the number of the grains vs. the misorientation angle near the weld interface; (b) Zoomed-in section with higher misorientation angles showing a peak for all the samples with similar distributions. 73

4.10 Study to determine the effect of UAM process settings on the weld interface microstructure at a fixed weld force of 5000 N: (a) Weld amplitude varied by fixing the weld speed at 84.67 mm/s (200 in/min); (b) Weld speed varied by fixing the weld amplitude at 29 µm. 76

4.11 Weld power, X-position of the workpiece, and weld force as recorded by NI 9239 sampled at 50 kHz using weld parameters: 35 µm welder amplitude, 5000 N weld force and 84.67 mm/s (200 in/min) weld speed. 77

4.12 Flowchart showing the method to calculate energy stored in the microstructure from raw EBSD data. 78

4.13 Comparison of post-UAM microstructure to control: (a) Stored energy map for sample prepared using 23 μm weld amplitude; (b) Histogram of stored energy showing a peak near the weld interface; (c) Stored energy map for the as-received rolled foil (control) showing elongated grains with low misorientations; (d) Histogram of stored energy for the control. 79

4.14 Trends in the stored energy in the microstructure with the weld parameters used for fabrication in UAM: (a) stored energy map for the control vs. samples prepared using 23, 29, and 32-μm weld amplitude; (b) total stored energy in the microstructure per unit length compared against the input electrical energy per unit length of weld as a function of weld amplitude; (c) stored energy map for the control vs. samples prepared using 125, 200, and 275 in/min weld speed; (d) total stored energy in the microstructure per unit length compared against the input electrical energy per unit length of weld as a function of weld speed. 80

5.1 Optical profilometry setup: (a) Specimen with 2-layers of Al 6061-H18 foil welded onto a Al 6061-T6 baseplate; (b) Bruker Contour GT-K optical profilometer used for non-contact roughness measurement. . . 86

5.2 Bruker Contour GT-K optical profilometer used for non-contact roughness measurement: (a) 3-D surface profile of an as-welded UAM foil prepared using the following weld parameters: 28 μm weld amplitude, 5000 N weld force, and 84.67 mm/s (200 in/min) weld speed. with 2-layers of Al 6061-H18 foil welded onto a Al 6061-T6 baseplate with $R_a = 9.66$ μm; (b) The 2-D projection of (a); (c) 3-D surface profile of an as-received foil of Al 6061-H18 with $R_a = 0.11$ μm; (d) the 2-D projection of (c). 87

5.3 Flowchart to produce different surface textures on the first welded foil before welding foil 2. Optimal process conditions used for Al 6061-H18 are 32 μm weld amplitude, 5000 N weld force, and 84.67 mm/s (200 in/min) weld speed. 88

5.4 The surface of a machined Al 6061-T6 baseplate was modified using sandblasting using steel and alumina pellets to obtain surface textures with R_a values of 7 and 4 μm, respectively. 89

5.5 The R_a value of the surface texture produced using different pretexturing amplitudes at a fixed traversal speed of 84.67 mm/s (200 in/min). 90

5.6 The shear testing rig used with compression platens in an MTS load frame used to test the foil−foil weld strength in shear. 91

5.7 In-situ process power measurements for the welding of a second Al 6061-H18 foil onto Al 6061-H18 foil with different surface preparations: (a) The surface of the first foil is machined per Figure 5.3 and pretextured using different amplitudes; (b) weld power drawn by the transducers is monitored for the welding over the different sections, and was found to be invariant with pretexturing amplitude. 92

5.8 Samples prepared with different pre-weld surface textures using pretexturing: (a) Image of 23-layers of Al 6061-H18 welds welded onto the Al 6061-T6 baseplate by varying the welder vibration amplitude set point using a fixed 5000 N normal force and 84.67 mm/s (200 in/min) weld speed; (b) Mechanical testing coupons prepared at different surface preparation conditions for foil-foil welding between the first and second layer. 93

5.9 Shear testing results: (a) Individual stress versus displacement curves of full-size samples prepared using different surface textures between foil 1 and foil 2 before welding; (b) failure stress in shear as a function of the pretexturing amplitude which shows no significant effect of pretexturing on the resulting weld strength. Error bars are added to indicate 95% confidence intervals from multiple replicate shear samples. Some replicates were damaged during the fabrication of the shear sample. 94

6.1 Schematic of the thermal-structural model to estimate the energy of plastic deformation E_{pl} and the energy dissipated due to friction E_f. . 99

6.2 Illustration of the forces and vibration velocities during UAM: (a) the contact width $2a$ of the weld foil of thickness t with the yielded foil material under the welder; (b) the top of the foil of width w sticks to the welder and the bottom of the foil has a slip velocity profile $\dot{\delta}_{slip}(x)$ with the workpiece (previously welded foil or baseplate). The vibration velocity of the workpiece is assumed to be small in comparison to the welder's vibration velocity. 101

6.3 The expression in (6.16) is plotted as a function of the variable η. The minimum value for the expression is 1 when $\eta = 0$. The dotted red line denotes the value of the expression at a weld force $F_n = 5000$ N and shear force $F_s = 2000$ N. 104

6.4 The normal and shear stresses along the contact width are plotted vs. the X-position normalized with the contact width a: (a) normalized normal stress $= \frac{\sigma(x)}{\sigma_y}$ from (6.5) and (b) normalized shear stress $= \frac{\tau(x)}{\sigma_y/3}$ from (6.10) for three different values of $\eta = 0$, 0.75, and 1.5. The value of $\eta = 0$ corresponds to the shear force $F_s = F_{s,min}$ from (6.17). . . . 105

6.5 A transient thermal simulation of the rotating welder and the translating workpiece simulated using COMSOL. The welder rotates such that there is no rolling slip with the workpiece. The weld foils and the baseplate are modeled as one piece since they are all made of aluminum alloys. A pairwise thermal contact is defined between the welder and the workpiece, with heat generation at the interface. 111

6.6 Temperature field in K under a rotating welder and a feedstock translating at a speed of 84.67 mm/s (200 in/min) simulated using COMSOL. Thermal power of 2000 W is input to the welder-workpiece interface which is partitioned based on Charron's rule (6.36). A temperature increase of 107 K from ambient was estimated. 112

6.7 Temperature field in K under a rotating welder with a translating feedstock simulated using COMSOL at different weld speeds, and the corresponding temperature profile on the welder for a 2000 W reference heat input at the welder-workpiece interface: (a) The temperature at the foil-welder interface as a function of time from the FE model. The temperature reaches a steady value which corresponds to the weld temperature measured by the IR camera in subsection 6.3.3; Temperature vs. angle plots of the welder for weld speed $\dot{x}$ of (b) 52.92 mm/s (125 in-/min), (c) 84.67 mm/s (200 in/min), and (d) 116.4 mm/s (275 in/min). 114

6.8 Setup to measure the weld temperature during UAM in-situ: (a) illustration of the IR camera positioned to view the front of the welder during welding; (b) image of the FLIR A6751sc camera positioned using a Manfrotto boom arm. 115

6.9 IR temperature measurements during the UAM of Al foils onto a 0.5 in thick Al 6061-T6 baseplate: (a) Peak temperature vs. time for Al 5052-H38, with a steady weld temperature of 74° C; (b) Infrared image during welding the welding of Al 5052-H38, where the black dotted line follows the point with maximum temperature from left to right; (c) Peak temperature vs. time for Al 6061-O, with a steady weld temperature of 118° C; (d) Infrared image during welding the welding of Al 6061-O, where the black dotted line follows the point with maximum temperature from left to right. 117

6.10 Weld temperatures for the welding of Al 6061-O, Al 6061-H18, Al 5052-O, and Al 5052-H38 measured using infrared imaging using a weld force of 5000 N and a weld speed of 84.67 mm/s (200 in/min) and varying weld amplitude. The measurements are compared against estimates from the analytical model. The total heat generated was estimated using (6.32) and input to the thermal finite element model to predict the temperature increase. Two possible values of the parameter β are chosen to account for the differences between the alloys. 120

6.11 The foil−foil weld interface shear strength is measured for UAM-ed Al 6061-H18 and Al 5052-O samples welded using a weld force of 5000 N and a weld speed of 84.67 mm/s (200 in/min), and is normalized by the bulk shear strength of the foil material. The weld amplitude was varied between 23 and 32 μm to fabricate the welds. The expression in (6.37) was used to estimate the normalized weld interface shear strength. The higher increase in shear strength for Al 5052-O material is attributed to work hardening, and an empirical hardening coefficient of 2.5 was used to account for this. 121

6.12 Flow of electrical energy per unit time (E_{ip}) from the welder (electrical) to the different energies involved in the UAM process. A energies were estimated using the following weld parameters for the UAM of Al 6061-H18: weld amplitude of 32 μm, weld speed of 84.67 mm/s (200 in/min), and a weld force of 5000 N. The useful energy E_{useful} for bond formation is defined in (6.38). 123

A.1 TEM measurements of air-grown oxide layer of as-received Al 6061-H18 foil at room temperature. The thickness of the oxide layer is found to be less than 20 nm. RD denotes the rolling direction of the welder. To the left is as-received foil, and to the right is the deposited platinum and gold. The bright segment in the middle contains the oxide layer of Al. 135

B.1 Stress vs. strain curves from uniaxial tensile testing of as-received Al 6061-H18 foil conducted at different controlled temperatures (86, 300, 350, and 400 F). 137

C.1 Calibration of the infrared emissivity of the steel welder using a OMEGA Type K AWG 40 thermocouple (0.080 mm tip diameter): (a) Infrared image of the setup showing the thermocouple bonded to the side of the welder and the infrared camera estimating the welder temperature from the exposed surface of the steel welder (enclosed in the red rectangle); (b) Comparison of the measured temperatures estimated using the thermocouple and infrared images. 139

Chapter 1

Introduction

Manufacturing is vitally important to the US economy, representing more than $2 trillion and 12.5% of the GDP, offering the highest economic multiplier of any segment of the economy. Each dollar of manufacturing spending generates $1.33 in economic activity. This research has the potential to enable the widespread adoption of Ultrasonic additive manufacturing (UAM) in manufacturing. Equally important, UAM is a US-based additive technology, as opposed to common additive manufacturing methods that are supplied only overseas.

1.1 Background

Ultrasonic additive manufacturing (UAM), or ultrasonic consolidation, is a solid-state process capable of producing gapless metal 3D printed parts [2]. The process works by welding together similar or dissimilar metal foils in an additive fashion using ultrasonic welding. An ultrasonic welder is integrated into a CNC framework to permit intermittent machining between welding operations. The subtractive feature of the process enables the fabrication of complex internal features, embedment of objects, and net shaping of parts [3]. A state-of-the-art UAM system is shown in Figure 1.1 which illustrates the additive and subtractive stages of the process.

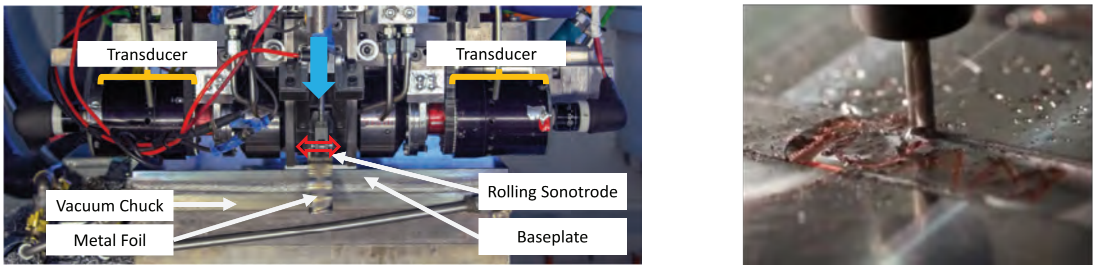

(a)

(b)

Figure 1.1: Fabrisonic 9 kW SonicLayer 4000 ultrasonic additive manufacturing system: (a) the ultrasonic welder is used to additively join foils together on a vacuum chuck fixture; (b) the subtractive CNC stage is used to introduce complex internal features and to trim components. The two Dukane ultrasonic transducers are each rated to 4.5 kW. The solid blue downward arrow represents the normal force applied during welding (weld force) and the hollow red side-to-side arrow represents the vibratory scrubbing action.

The welding or additive stage of the process works by bringing a tool piece called the welder, sonotrode, or horn into contact with a metallic foil under a controlled pressure. Then, the sonotrode is actuated at a nominal resonance frequency of 20 kHz with piezoelectric transducers which scrub the metallic foil against pre-deposited metal foils or a baseplate metal beneath. The circular design of the sonotrode allows it to rotate in place while the foil stock is fed at a prescribed linear speed underneath it.

A key feature of the UAM process is the low formation temperature, which enables joining of dissimilar metals without the formation of brittle intermetallic phases. The low temperature aspect of the process enables the joining of many different metal combinations [4]. Using thermocouples embedded at the weld interface, the work in [5] showed that the peak temperature reaches near 150°C for welding aluminum and copper alloys with a 9 kW welder. Previous work in [6] measured a temperature increase between 400 and 700 K for the welding of 4130 carbon steel. Intermetallics often form in fusion processes with dissimilar metals because elevated temperatures permit mixing and diffusion. In contrast, melting and subsequent solidification are absent in UAM, and diffusion can be minimal.

The introduction of very high power ultrasonic additive manufacturing (VHP-UAM), which increased the power envelope of the process from 1 kW in first-generation systems to 9 kW by using two piezoelectric transducers in a push-pull configuration, dramatically increased process capabilities to enable gapless, fully dense joints [7]. The higher available weld power expands the range of alloys that can be welded with UAM: from softer 3000 series aluminum [8] to higher strength materials such as 6000 series aluminum [9], steel [10, 11], and titanium [12]. Parameters controlled during welding include normal force (weld force), amplitude setpoint of oscillation (weld amplitude), and speed of rolling (weld speed) [8]. Additionally, certain UAM systems have an integrated thermal plate that can heat the baseplate to a prescribed preheat temperature, enhancing bonding by reducing the yield stress for certain material systems. The levels of these parameters vary depending on the material being welded and have a significant influence on bond quality [8, 9]. Limited work has also been conducted on the effect of surface roughness [13] and cold work [14, 15] on UAM bond quality.

Several studies [5], [16], [17] have found that plastic deformation is important for the bonding between layers during UAM, and plastic flow is important for redistribution of the oxide layer, forming of mechanical interlocks, filling micro-valleys on the mating surface, and filling gaps when embedding elements. It was found in [18] that the energy of plastic deformation is much higher in magnitude than the energy dissipated by friction, which some studies [19], [20] have considered to be the dominant energy in the UAM process. The UAM process has similarities to cold roll bonding (CRB), a simple solid-state joining process where two foils are rolled under high pressures to create a weld.

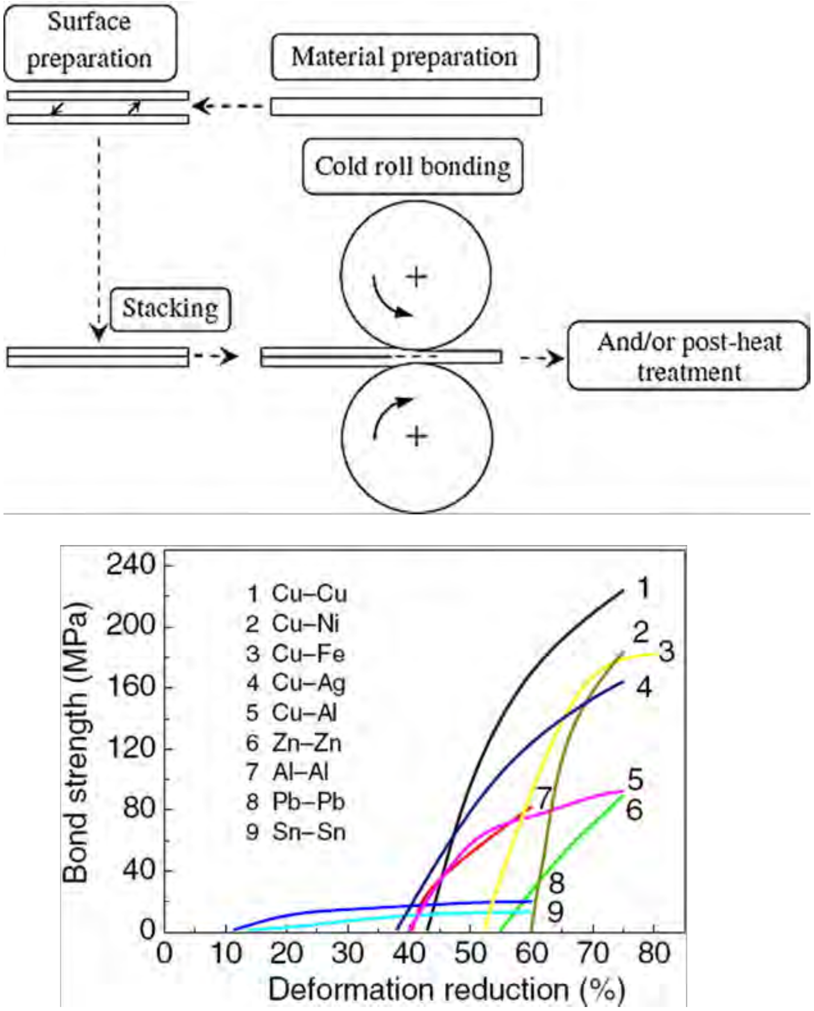

Figure 1.2: The relationship between deformation reduction and the strength of the resulting bond shown for cold roll bonding, a room-temperature solid-state joining process by rolling two foils together using rollers, reproduced from [1].

There are several competing theories for bond formation in cold roll bonding [21]. The film theory proposes that nascent metallic contact instantaneously forms a bond, and the fragmentation of the oxide layer is the only barrier to bonding, used in [22] for ultrasonic consolidation. However, the high amplitude cyclic deformation applied by the welder is expected to cause the brittle oxide layer to crack, and thus not a barrier to bonding as in roll bonding. The asperities in the foil are also found not to play a significant role in weld strength, and thus this model is considered to be insufficient. The energy barrier theory proposes that even after nascent metallic contact, an activation energy needs to be applied for bond formation. In this dissertation, this activation energy will be presumed to be proportional to the energy of plastic deformation as it was found in [21] that plastic deformation is a key requirement for solid-state welding. In this work, using a sleeve to restrict lateral displacement, and hence plastic deformation, prevented the solid-state butt welding of two blocks at deformations where bonding was otherwise expected.

The relationship between bond strength and deformation shown in Figure 1.2 is similar to that between bond strength and shear deformation in UAM. Work in [23] showed that ultrasonic consolidation shows a similar threshold energy requirement for bond formation. Several studies have tried to develop an analytical expression for the relationship between deformation reduction R and the bond strength ratio (to the bulk strength) η in cold roll bonding. A simple model accounting for the threshold deformation R_{th} seen in Figure 1.2 is found in [24]:

$$\eta = H\left(1 - \frac{(1-R)^2}{(1-R_{th})^2}\right), \tag{1.1}$$

where H is an empirical hardening coefficient. Other studies [25], [26], [27], [28] have developed more complex expressions requiring knowledge of the properties of the oxide layer and the flow stress of the material. The superposition of stresses introduced by the out-of-plane ultrasonic vibrations in UAM is expected to reduce the deformation required for bonding. In this dissertation, UAM will be modeled as ultrasonically-assisted cold-roll bonding.

1.2 Problem statement and research objectives

Transportation accounts for a significant proportion of the global energy consumption and is approximately 28% of the U.S. energy consumption. The main source of this energy is derived from petroleum sources [29], and hence, solutions to reduce fuel consumption in automobiles are critical to reduce greenhouse emissions and meet U.S. fuel economy requirements for new light-duty vehicles to achieve 54.5 miles per gallon by 2025 [30]. Vehicle lightweighting is a promising solution to tackle this challenge, as 10% reduction in vehicle weight can improve fuel efficiency by 6-8% [29]. Vehicle lightweighting in the automotive industries requires the ability to join dissimilar metals and integrate metallic and non-metallic components for reinforcement without compromising on safety.

Ultrasonic additive manufacturing (UAM) is an enabling technology for vehicle lightweighting, as it has the capability to join similar and dissimilar metals in solid state and to embed both active materials and electronics in metals due to its low formation temperature. The process combines ultrasonic metal welding, using a layer-by-layer process, with subtractive processes to create large, gapless, near net-shape metallic parts. Hence, it can be used to fabricate 3D structures that incorporate dissimilar metals (e.g., aluminum, copper, and titanium), internal conformal channels for cooling and other transport purposes, and temperature sensitive components such as sensors, reinforcement fibers [31], electronic circuits, fiber optics [32], and smart materials [33].

However, studying the feasibility of joining new material combinations and optimizing weld parameters for new geometries requires time-consuming and expensive trials. Understanding the effect of build mechanical properties and energy input on the resulting UAM joint strength is crucial for reliable large-scale development of additively manufactured builds. There is a lack of predictive ability in models available in the literature to establish process-property relationships for UAM builds. There is also limited understanding about the bonding mechanisms and the effect of surface roughness, cold work and mechanical properties of the metal on the strength of the resulting joint.

It is therefore necessary to develop new analytical tools that, with knowledge of material properties (e.g., mechanical, microstructural, surface properties), will allow determination of the UAM process parameters for optimal strength within a given system parameter envelope and geometry. Fundamental research to develop validated models will be useful to predict process property relationships in new material combinations (e.g., high strength steels and titanium), and reduce the resources required to optimize process parameters.

1.3 Dissertation organization

The outline of this dissertation is as follows. A model for the effect of system compliance on weld power is developed in Chapter 2 using modal analysis and analytical and finite element (FE) modeling. In-situ process measurements using Doppler velocimetry are developed in Chapter 3 for in-line process quality control. In Chapter 4, the energy stored in the microstructure of welded samples is characterized and the trends in stored energy with weld parameters is investigated. In Chapter 5, the effect of changing the surface roughness of the mating surfaces using treatment methods such as pretexturing and sandblasting on the resulting part quality is investigated. In Chapter 6, a transient thermal FE and an analytical structural model is built to model the transfer of heat generation and plastic deformation in UAM. This model is used to audit the flow of energy in UAM. This audit is used to develop process-property relationships to relate the energy of plastic deformation and weld strength. Key findings are summarized in Chapter 7. Lastly, the appendix contains studies that support the dissertation effort.

Chapter 2

Effect of System Compliance on Weld Power in Ultrasonic Additive Manufacturing

Overview

This chapter develops a model for the relationship between UAM weld power and system compliance considering the workpiece (geometry and materials) and the fixture on which the build is fabricated. Linear elastic finite element modeling and experimental modal analysis are used to characterize the system's mechanical compliance, and linear system dynamics theory is used to understand the relationship between weld power and compliance. In-situ measurements of the weld power are presented for various build stiffnesses to compare model predictions with experiments. Weld power in UAM is found to be largely determined by the mechanical compliance of the build and insensitive to foil material strength.

2.1 Introduction

Ultrasonic additive manufacturing (UAM) or ultrasonic consolidation, is a solid-state process capable of producing gapless metal 3D printed parts [2]. The process works by welding together similar or dissimilar metal foils in an additive fashion using ultrasonic welding. The ultrasonic welder is integrated into a CNC framework to permit intermittent machining between welding operations. The subtractive feature of the process enables the fabrication of complex internal features, embedment of objects, and net shaping of parts. Many UAM studies have been conducted to determine the optimal process parameters such as welder's vibration amplitude, travel speed of the welder (weld speed), weld force, and baseplate temperature to produce strong welds between similar and dissimilar materials [34]. However, the same process parameters produce different amounts of weld power depending on the workpiece geometry and the materials being welded, and these studies do not report weld power measurements. Weld power has been shown to have a strong influence on the mechanical strength and the microstructure of the weld interface [15]; therefore, it is necessary to develop a model for weld power as a function of process parameters and the geometry and material properties of the workpiece.

The work in [15] showed that using a constant weld amplitude to weld all the layers of a 20-layer build using Al 6061-H18 results in a decrease in weld power with build height. The microstructure and strength of this so-called uncompensated build were compared with a build where the weld amplitude was increased with build height to maintain a constant weld power. The uncompensated build with lower weld power and hence lower input strain energy was found to have poor mixing and lower grain refinement than the power-compensated build. An 18% lower energy absorption and 6% lower peak force were observed in push-pin testing of the uncompensated build. This showed a direct connection between the weld power in UAM to the weld interface microstructure and the mechanical strength of the resulting part. The structural compliance of the build has been shown to influence the weld power and the lateral compliance of the welded stack can be approximated using the expression for a cantilever beam fixed on one end. However, this work did not examine the effect of build geometry and the foil material being welded, or establish a quantitative relationship between the system's compliance and weld power. The work in [19] included a study on the effect of build height on weld power using multiple regression analysis and developed an empirical fit between build height and weld power, but did not develop a physical model to predict weld power for an arbitrary workpiece geometry.

The work in [35] included the development of a lumped parameter LTI model of the weld assembly which relates the shear force and current to the voltage and vibration velocity. The authors proposed that this model, coupled with a complex stiffness load impedance term to model the dynamics of the workpiece, would be able to describe the transfer of power from the weld assembly to the workpiece during UAM. Viscous damping elements can be used to model a range of loss mechanisms such as hysteretic damping or Coulomb friction [36]. Networks of viscous damping and spring elements have been used in modeling the dynamics of tool-workpiece interactions in other manufacturing processes, including ultrasonic drilling [37], ultrasonic machining [38], and peripheral milling [39].

The broad objective of this chapter is to establish a relationship between the mechanical compliance of the build (which includes the foil material being welded, the workpiece being welded onto, and the fixture) and weld power. Because a change in power is observed to have a significant effect on weld quality [15], the goal of this investigation is to develop a predictive tool to determine the weld parameter settings needed to obtain a target weld power for UAM joining of metals with different build configurations. The travel speed of the welder (weld speed) is fixed in this analysis, since previous works have found that changing the weld speed does not significantly change the weld power [19, 35]. Preheating has been used in UAM to improve bond quality [10, 34], but it is not used in this study since it is not required for producing successful bonding for the materials tested.

In Section 2.2, a dynamic stiffness model is used to characterize the mechanical loading on the welder during UAM. This model is coupled with the LTI model of the weld assembly presented in [35] to develop an expression for weld power as a function of load stiffness. In Section 2.3, equivalent circuit analysis is used to develop a lumped parameter model for the dynamic load stiffness with a damping element in parallel with lumped compliance elements that account for the individual contributions from the foil being welded, welded stack, baseplate, and fixture. Using relationships developed in Section 2.2, weld power-stiffness relationships are developed. In Section 2.4, the stiffness of the foil with the workpiece (baseplate and welded stack) is characterized using finite element modeling (FEM). Modal analysis is used to characterize the stiffness of the vacuum chuck fixture.

In Section 2.5, three different studies are presented to test the weld power predictions for a range of workpiece and fixture configurations. The first study (2.5.1) investigates the effect of baseplate stiffness on weld power by welding Al foil on Al and steel baseplates chosen with different stiffness values. The weld power predictions from the model show good agreement with these measurements. The second study (2.5.2) investigates the effect of foil material stiffness on weld power using a stiffer foil material, copper. Ten layers of Cu C11000-O60 were built onto an Al 6061-T6 baseplate, and the weld power measurements were compared with model predictions. The third study (2.5.3) investigates the dependency of the parameters of the weld power model on the foil type. Al 6061-H18, Al 6061-O, Al 3003-H18 foils were chosen to be welded onto an Al 6061-T6 baseplate because they have the same elastic properties but very different characteristics in the plastic deformation regime. Cu C11000-O60 foils were also welded for comparison. It is observed that the model's damping parameter is not foil-dependent. The foils were also welded using a range of weld amplitudes to validate the weld power model.

2.2 Model for dynamic load stiffness and weld power in UAM

The linear time invariant (LTI) model of the weld assembly from [35], which relates the shear force and electric current to resultant welder velocity and voltage, is reproduced below with $\dot{x}_{welder}$ replacing $\dot{\delta}$:

$$\begin{pmatrix} V(j\omega) \\ \dot{x}_{welder}(j\omega) \end{pmatrix} = \begin{bmatrix} H_e^*(j\omega) & H_{me}^*(j\omega) \\ H_{em}^*(j\omega) & H_m^*(j\omega) \end{bmatrix} \begin{pmatrix} i(j\omega) \\ F_s(j\omega) \end{pmatrix}. \tag{2.1}$$

This model describes the interrelation between the electrical and mechanical signals in the frequency domain to explain the transfer between electrical and mechanical power within the welder. The terms $H_e^*(j\omega)$, $H_m^*(j\omega)$, and $H_{me}^*(j\omega)$ are the electrical, mechanical, and electromechanical transfer functions, respectively. The electrical signals $V(j\omega)$ and $i(j\omega)$ are the voltage and current applied to the transducers, respectively, and the mechanical signals $F_s(j\omega)$ and $\dot{x}_{welder}(j\omega)$ are the shear force acting on the sonotrode and vibration velocity of the welder, respectively.

A dynamic mechanical stiffness term is used to model the load on the welder during UAM, which is then coupled with the LTI model of the weld assembly from [35]. The parameterization of the dynamic stiffness term is discussed in Section 2.3, where we develop a relationship for weld power as a function of a generalized dynamic mechanical stiffness $\widetilde{K}_{LD}(j\omega)$ that accounts for contributions from the contact interactions between the welder and the materials being welded. A parametric model for the load stiffness is then developed by considering the individual contributions from the foil being welded, welded stack, baseplate, and fixture.

The dynamic mechanical stiffness $\widetilde{K}_{LD}(j\omega)$ is defined as the ratio of the shear force to the welder's vibration displacement. The stiffness can be separated into its real ($\widetilde{K}_R(j\omega)$) and imaginary ($\widetilde{K}_I(j\omega)$) parts as

$$\widetilde{K}_{LD}(j\omega) = \frac{F_s(j\omega)}{\dot{x}_{welder}(j\omega)/j\omega} = \widetilde{K}_R(j\omega) + j\widetilde{K}_I(j\omega). \tag{2.2}$$

The $(j\omega)$ term is dropped henceforth for brevity. When the welder is under load, the relationships between the inputs and outputs in the electromechanical model at the excitation frequency can be simplified to the following expressions using $\widetilde{K}_{LD}$ as described in (2.2):

$$\begin{aligned} V &= H_e^* i - H_{me}^* (\widetilde{K}_R + j\widetilde{K}_I)\frac{\dot{x}_{welder}}{j\omega}, && (2.3) \\ \dot{x}_{welder} &= H_{em}^* i - H_m^* (\widetilde{K}_R + j\widetilde{K}_I)\frac{\dot{x}_{welder}}{j\omega}. && (2.4) \end{aligned}$$

Eliminating $\dot{x}_{welder}$ from the two expressions, the relationship between voltage and current simplifies to

$$\frac{V}{i}(j\omega) \quad = \quad \frac{\Psi_t^2}{j\omega M_t + (D_t + \frac{\widetilde{K}_I}{\omega}) + \frac{K_t + \widetilde{K}_R}{j\omega}}, \tag{2.5}$$

where the parameters Ψ_t, M_t, and D_t of the LTI model for the weld assembly are defined in [35].

The welder is operated using a motional feedback controller, which uses a phase-locked loop (PLL) algorithm to minimize the phase difference between the voltage and current. This ensures that the voltage and current signals are in phase. It also employs amplitude control to keep the amplitude of the voltage constant during welding. Assuming harmonic signals V and i, the average electrical power consumed during welding can thus be expressed as

$$P_{e,avg}^{weld} \quad = \quad \frac{1}{2}|V|.|i| = \frac{1}{2}\left(D_t + \frac{\widetilde{K}_I}{\omega_{weld}}\right)|\dot{x}_{welder}|^2, \tag{2.6}$$

where $|V|$ and $|i|$ denote the zero-to-peak amplitudes of the respective signals and $\omega_{weld} = 2\pi f_{weld}$, where f_{weld} is the fundamental frequency of vibration of the welder during welding. Since the voltage and current signals are in phase, the welder frequency f_{weld} can be obtained by setting the imaginary part in the right hand side of (2.5) to zero, giving

$$f_{weld} = \frac{1}{2\pi}\sqrt{\frac{K_t + \widetilde{K}_R}{M_t}}. \tag{2.7}$$

2.3 Lumped parameter modeling of dynamic load stiffness

2.3.1 Equivalent circuit analysis

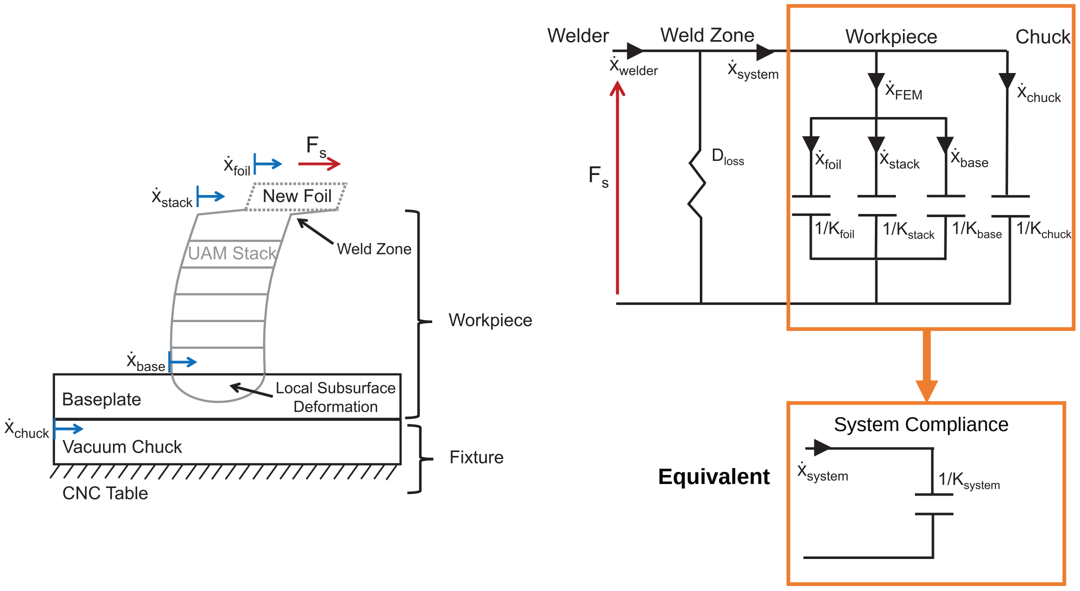
F_s
$\dot{x}_{foil}$
$\dot{x}_{stack}$
New Foil
UAM Stack
Weld Zone
Workpiece
$\dot{x}_{base}$
Baseplate
Local Subsurface Deformation
$\dot{x}_{chuck}$
Vacuum Chuck
Fixture
CNC Table
Welder
Weld Zone
Workpiece
Chuck
$\dot{x}_{welder}$
$\dot{x}_{system}$
$\dot{x}_{FEM}$
$\dot{x}_{chuck}$
F_s
D_{loss}
$\dot{x}_{foil}$
$\dot{x}_{stack}$
$\dot{x}_{base}$
$1/K_{foil}$
$1/K_{stack}$
$1/K_{base}$
$1/K_{chuck}$
Equivalent
System Compliance
$\dot{x}_{system}$
$1/K_{system}$

(a) (b)

Figure 2.1: UAM stack and system dynamics: (a) schematic illustration of the components that contribute to the mechanical compliance of the system; (b) equivalent circuit representation of the system. The weld zone deformation is modeled using a viscous damping element.

Figure 2.1(a) illustrates the components that contribute to the total system stiffness and how system stiffness impacts the UAM process. Due to the combined compliance of the UAM stack, the baseplate near the stack, and the vacuum chuck, only a portion of the displacement imparted by the sonotrode is used to displace the new foil being welded relative to the stack. Figure 2.1(b) shows an electrical equivalent circuit representation of this system. This model is an extension of the equivalent circuit analysis of the weld assembly in [35]. A viscous damping element, D_{loss}, is used to represent the mechanical losses in the weld zone. Lumped compliance elements are used to model the dynamic response of the foil, stack, baseplate, and vacuum chuck fixture. These elements behave as capacitors connected in parallel, which gives the following expression for the effective system compliance:

$$\frac{1}{K_{system}} = \frac{1}{K_{foil}} + \frac{1}{K_{stack}} + \frac{1}{K_{base}} + \frac{1}{K_{chuck}}. \tag{2.8}$$

All the stiffness terms in the rest of this paper are in the lateral (along the welder's vibration) direction. The CNC table is modeled as a rigid base, hence its stiffness is assumed to be infinite. The lumped stiffness of the vacuum chuck is estimated using modal analysis, detailed in Section 2.4.1. The stiffness of the foil, stack, and baseplate are estimated using finite element analysis in Section 2.4.2.

In order for the equivalent circuit representation to be accurate, the following assumptions are made. First, it is assumed that there is no slip between the welder and new foil, and between the new foil and workpiece. The no-slip assumption is supported by findings in [5], where good agreement was found between temperature at the foil−foil interface measured using a thermocouple, and the temperature predicted using a thermal model that considered only plastic deformation as the heat source and neglected frictional slip. As detailed in [5], while there is some work in the literature that does not neglect the contribution of frictional slip to the overall heating in ultrasonic welding, it is proposed that once initial sliding disperses the oxide layers and initiates the contact of nascent metal from both foils, there is no further slip at the weld interface.

Second, it is assumed that the dynamics of the workpiece are primarily influenced by its quasi-static stiffness. Lumped stiffness elements are thus used to approximate the dynamic response of the welded stack and baseplate. This assumption is valid if the frequency corresponding to the lateral (shear) mode of vibration of the structure is significantly higher than the excitation frequency of 20 kHz. It is possible for the resonance frequency of the build to approach the excitation frequency of the welder [40], which would affect the dynamic response of the build to sonotrode vibrations. An eigenfrequency analysis of a representative UAM build, a 20-layer Al stack welded onto a 9.53 mm (0.375 in) thick Al baseplate, was performed using COMSOL to estimate the frequency of the first shear mode. The first shear mode of vibration is shown in Figure 2.2, computed using the eigenfrequency solver within COMSOL. The eigenfrequency or resonant frequency of the stack and baseplate in shear is near 70 kHz, which is well above the excitation frequency of 20 kHz. As a result, the dynamics of the stack are primarily influenced by the quasi-static stiffness at 20 kHz. Hence, the system is assumed to be quasi-static for modeling purposes, and mass terms are not considered for the stack, foil, or baseplate.

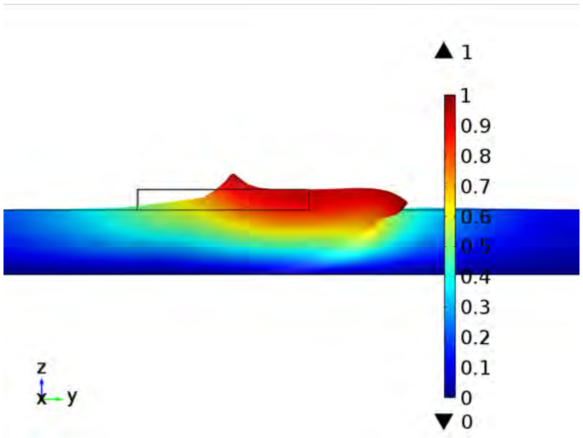

Figure 2.2: The first mode of vibration in shear of a 20-layer Al stack and 9.53 mm (0.375 in) thick Al baseplate in shear is identified using the eigenfrequency solver within COMSOL to be 70.4 kHz, which is well above the 20 kHz excitation frequency. The color scale represents the normalized total displacement.

Third, it is assumed that the lumped viscous damping element in the weld zone in Figure 2.1(b) accounts for all of the energy losses near the foil-welder contact, including frictional heating and plastic deformation near the weld interface. Losses due to friction in the baseplate and chuck are assumed to be negligible. The damping coefficient D_{loss} is assumed to be constant and not dependent on the weld parameters or foil type. This assumption is tested in Section 2.5.3.

2.3.2 Weld power - stiffness relationships

The average mechanical power consumption is affected by the phase angle between the harmonic shear force F_s and the welder's vibration velocity $\dot{x}_{welder}$, which changes when the system stiffness K_{system} is varied. The dynamic mechanical stiffness $\widetilde{K}_{LD}$ at the operating frequency is determined considering the system's compliance in parallel to the damping element, which has an impedance of $j\omega D_{loss}$, to be

$$\begin{aligned}\widetilde{K}_{LD}(j\omega_{weld}) &= \frac{j\omega_{weld}}{(j\omega_{weld})/K_{system} + 1/D_{loss}} &(2.9)\\ &= K_{system}\frac{(\omega_{weld}D_{loss})^2}{K_{system}^2 + (\omega_{weld}D_{loss})^2}\\ &+ j\omega_{weld}D_{loss}\frac{K_{system}^2}{K_{system}^2 + (\omega_{weld}D_{loss})^2}, &(2.10)\end{aligned}$$

where $\omega_{weld} = 2\pi f_{weld}$ and f_{weld} is the fundamental frequency of the welder's vibration during welding.

Using the expression for weld power (2.6), and substituting $|\dot{x}_{welder}| = \omega|x_{welder}|$ in (2.10), the expression for weld power becomes

$$P_{e,avg}^{weld} = \frac{1}{2}\left(D_t + D_{loss}\frac{K_{system}^2}{K_{system}^2 + (\omega_{weld}D_{loss})^2}\right)\omega_{weld}^2|x_{welder}|^2. \tag{2.11}$$

This expression is a non-linear relationship between the weld power and the system stiffness with tunable parameter D_{loss} to be determined from experimental data. This relationship indicates that there is a maximum attainable weld power for a given configuration of foils, computed by setting $K_{system} \to \infty$, which is $P_{e,avg}^{weld,max} = (D_t + D_{loss})\omega_{weld}^2|x_{welder}|^2/2$. The lowest value is attained when the welder is ringing in air, with $K_{system} = 0$, where $P_{e,avg}^{weld,min} = D_t\omega_{weld}^2|x_{welder}|^2/2$.

It is desirable to be able to predict the weld power $P_{e,avg}^{weld}$ for a new base structure with stiffness K_{system} after welding using the same weld assembly on a reference structure with stiffness K_{system}^{ref} drawing weld power $P_{e,avg}^{weld,ref}$. A simple linear relationship can be developed to provide a good approximation of the model in (2.11) away from the extreme stiffness regimes. The model is linearized at the inflection point $K_{system} = D_{loss}\omega_{weld}/\sqrt{3}$ (point where the second derivative of power with respect to stiffness is zero). The linear model can be expressed as follows for a small stiffness change $\delta K = K_{system} - K_{system}^{ref}$:

$$\delta P = P_{e,avg}^{weld} - P_{e,avg}^{weld,ref} \quad \approx \quad \frac{3\sqrt{3}\omega_{weld}}{16}|x_{welder}|^2\delta K. \tag{2.12}$$

The slope of the linear fit in (2.12) does not depend on the damping coefficient D_{loss}. Therefore, if the weld power in a reference assembly is known, this linear relationship can be used to approximate the weld power for a different assembly without requiring an estimate for the damping coefficient.

2.4 Estimation of LTI model parameters

2.4.1 Estimation of vacuum chuck stiffness

In order to model and quantify the relative contributions of the welded stack, baseplate, and vacuum chuck fixture stiffnesses to the overall system's compliance defined in Figure 2.1(b), it is necessary to characterize the stiffness of the vacuum chuck anvil structure, which is the fixture used for all UAM welding experiments in this paper. Modal testing was carried out on the structure to estimate the dynamic stiffness of the structure near 20 kHz. The measurement is dynamic because mass, damping, and stiffness influences are measured simultaneously in a single term. Figure 2.3 shows the setup for estimating the mechanical dynamic stiffness, where a high frequency impact hammer (PCB 086C80) is utilized to impart the excitation force, and two high frequency accelerometers (PCB 352A60) measure the vibration response. Accelerometers were chosen rather than a non-contact laser vibrometer because concurrent measurements of the baseplate and vacuum chuck were desired and only a single-point laser vibrometer was available for use. The size and mass of the accelerometers are small compared to the size and mass of the base structure being measured, and do not cause additional mass loading effects in the experiment.

To emulate representative operating conditions in Section 2.5, a 9.53 mm (0.375 in) thick aluminum baseplate and a 3.18 mm (0.125 in) thick steel baseplate were each constrained to the chuck with vacuum pressure.

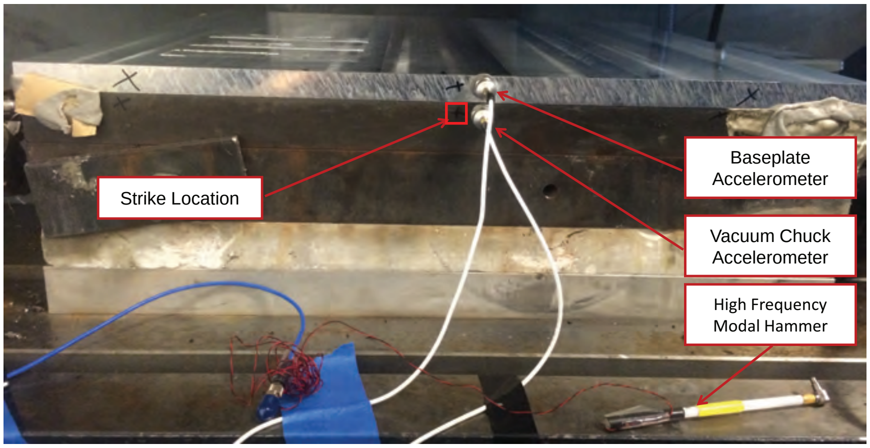

Figure 2.3: Setup for modal hammer testing of the vacuum chuck anvil structure using a 9.53 mm (0.375 in) thick Al 6061-T6 baseplate. This test is used to measure the dynamic stiffness of the structure with impacts on the vacuum chuck.

A QUATTRO signal analyzer was used to calculate frequency response functions (FRFs) $H(j\omega)$ between the force input and the corresponding measured acceleration output using ten exponentially-windowed averages. The dynamic stiffness $\widetilde{K}_{chuck}(j\omega)$ can be determined from the FRF $H_{chuck}(j\omega)$ between the force input F and the acceleration measured by the vacuum chuck accelerometer a_{chuck} to be

$$\widetilde{K}_{chuck}(j\omega) = H_{chuck}(j\omega)\omega^2, \tag{2.13}$$

$$H_{chuck}(j\omega) = \frac{F}{a_{chuck}}(\omega). \tag{2.14}$$

The transfer dynamic mechanical stiffness $\widetilde{K}_{chuck}(j\omega)$ of the vacuum chuck with respect to each baseplate, estimated with the strike location on the chuck and the response accelerometer location on the baseplate, is shown in Figure 2.4. The impedances measured with Al and steel baseplates mounted on the vacuum chuck are very close to each other. Ordinary coherence was close to 1 for the frequencies of interest near 20 kHz. Dynamic stiffness values below 5 kHz are not plotted because the corresponding coherence was poor. Since there are no resonant modes observed for the vacuum chuck anvil structure in the frequency range of interest near the welder frequency, it can be modeled as a lumped mechanical stiffness near 20 kHz. The stiffness K_{chuck} of the lumped spring in Figure 2.1(b) is estimated to be 2 GN/m by taking the magnitude of the transfer dynamic mechanical stiffness of the chuck (2.13) near 20 kHz.

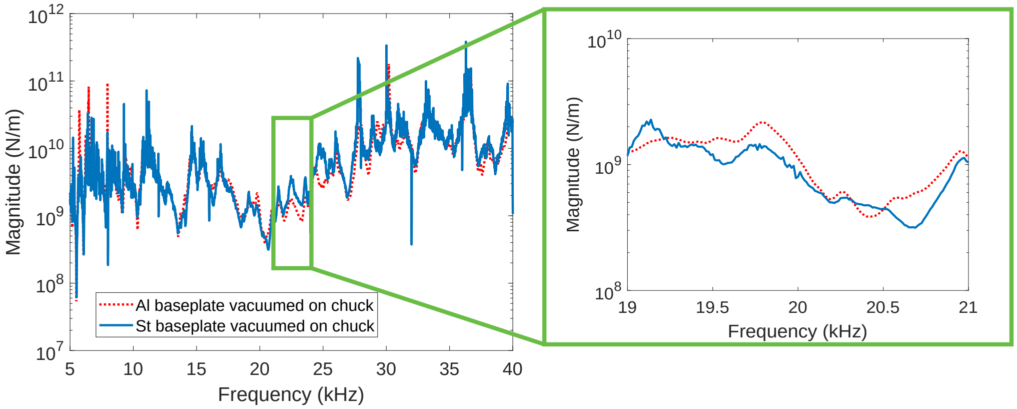

Figure 2.4: Dynamic transfer mechanical stiffness of the vacuum chuck with respect to a baseplate constrained to the vacuum chuck shown for aluminum and steel baseplates. Frequency response functions were measured by striking a modal hammer on the vacuum chuck and measuring the response using accelerometers on the vacuum chuck and the baseplate.

2.4.2 Estimation of system stiffness using FEM

To estimate the combined stiffness of the foil, stack, and baseplate, finite element modeling (FEM) in COMSOL Multiphysics is employed. The simulations are quasi-static and for simplicity, all materials are assumed to remain in the elastic domain. In this paper, different alloys of aluminum, copper, and steel are used for baseplate and foil materials. Built-in material properties in COMSOL for copper, Al 6063-T83, and AISI 4340 steel are used for simulation purposes. Although the alloying elements of these virtual materials differ from those in the materials tested, the linear elastic properties are the same. The system stiffness is then evaluated from (2.8) as

$$\frac{1}{K_{system}} = \frac{1}{K_{FEM}} + \frac{1}{K_{chuck}}, \tag{2.15}$$

where K_{FEM} is the quasi-static stiffness estimate for the stack and baseplate from FEM. Note that K_{chuck} was estimated in Section 2.4.1.

The contact surface width is estimated to be 0.90 mm (0.035 in) using elastic Hertzian contact theory[1]. This contact width is used for all simulations in this study. Figure 2.5(a) shows the components of the finite element model. The normal load and transverse load from the welder are input as applied loads on the contact surface in the -z and y directions, respectively. The quasi-static stiffness is estimated by dividing the transverse applied load (2000 N) by the average transverse deformation of the contact surface. Figure 2.5(b) shows the transverse (y-direction) deformation from the applied loads, which is used for estimating stiffness. A representative image of the graded mesh density of the FE model is shown in Figure 2.5(b). The inset illustrates the increased mesh density around the contact surface.

---

[1] The contact width is estimated using closed-form equations for a cylinder on a flat surface [41].

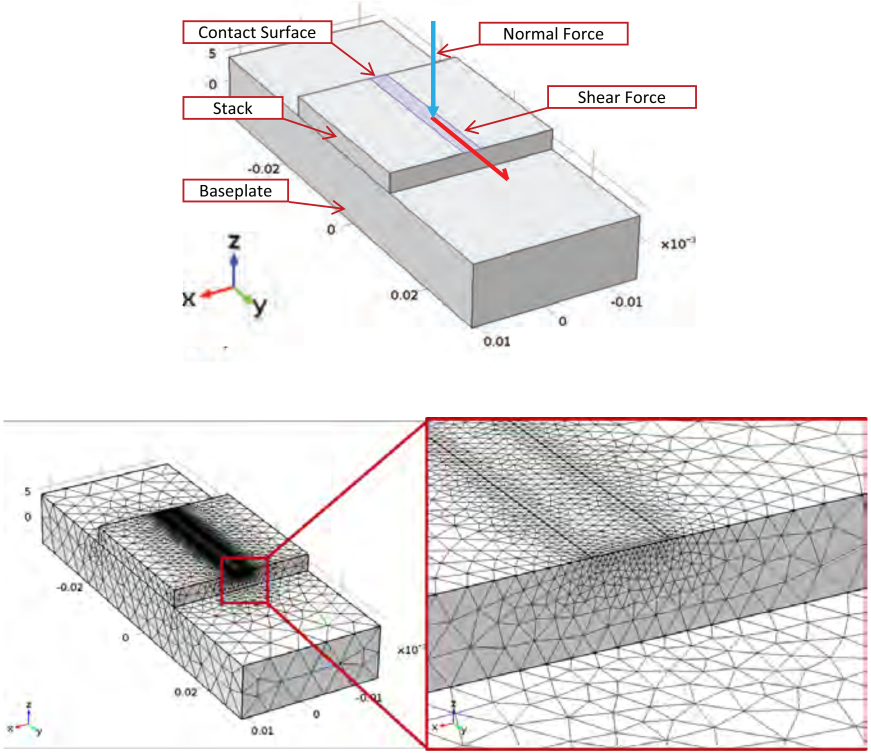

(a)

(b)

Figure 2.5: FE model of stack and baseplate: (a) Contact surface used to apply load from the weld tool. Normal (-z) and transverse (y) static loads are applied as traction loads on the contact surface. (b) Mesh density of FE model. A graded mesh was utilized near the contact surface to improve accuracy of the simulated stack deformation.

2.5 Experiments for validating weld power model

The model for weld power as a function of the system's compliance is established in (2.11). The system's compliance depends on the geometry and materials of the foil, previously welded layers, baseplate, and the vacuum chuck fixture. The model also includes a damping parameter D_{loss} which is calibrated in this section. Three studies are developed where the system's compliance is varied by changing the geometry and materials involved, and the resulting measurements of weld power are compared with model predictions to validate the weld power model. The compliance is estimated using the FE model and modal analysis as described in Section 2.4.

In Study A, the effect of baseplate stiffness on weld power is investigated. The baseplate materials and dimensions are chosen to achieve a wide range of system stiffness values based on the FE model. In addition, the effect of build height on weld power is investigated for the welding of Al foil. Based on the findings in [15], it is expected that the weld power will decay with increasing build height. In Study B, the influence of foil stiffness on the change in weld power with build height is studied for the welding of Cu C11000-O60 foil. In contrast to the stack of aluminum foils, the FE model predicts that the system stiffness for a stack of copper foils welded onto an aluminum baseplate is not very sensitive to build height due to the higher elastic modulus of copper. In Study C, the effect of foil material on the damping parameter D_{loss} is investigated. In-situ weld power measurements during the welding of four foil materials with substantially different elastic moduli and yield strengths are compared with model predictions.

2.5.1 Study A: Effect of baseplate stiffness on weld power

The influence of baseplate stiffness on weld power in UAM is investigated by welding 20 layers of 2.54 cm (1.00 in) wide and 152 μm (0.006 in) thick Al 6061-H18 foil on steel and aluminum baseplates. To obtain a large contrast in system stiffness, a 9.53 mm (0.375 in) thick Al 6061-T6 baseplate and a 3.18 mm (0.125 in) thick annealed AISI 4130 steel baseplate were chosen. FE simulation results corresponding to 2-layer and 20-layer Al 6061-H18 stacks welded onto these baseplates are shown in Figure 2.6. After the first foil is welded onto the baseplate, the system stiffness decreases from 433 to 364 MN/m (-16%) and 772 to 455 MN/m (-41%) for the Al and steel baseplates, respectively, during the welding of a twenty-layer Al stack. The baseplate dimensions were chosen such that their masses are equal, which is important because some baseplate slip is present in UAM when a vacuum chuck fixture is utilized [42]. This intermittent slip may introduce mass loading effects on the welder so it is desirable for these potential mass loading effects to be equal. Al 6061-H18 weld foil was used because multiple layers can be welded without foil sticking to the sonotrode, known as nuggeting.

The weld parameters shown in Table 2.1 were selected based on previous work welding Al 6061-H18 onto steel in [14], and hence they are different from the optimal values determined in a design of experiments study in [9] for welding of Al 6061-H18 foil onto an Al 6061-T6 baseplate. Prior to welding, both baseplates were textured (welder rolled on baseplate with ultrasonics on) using the weld parameters listed in Table 2.1.

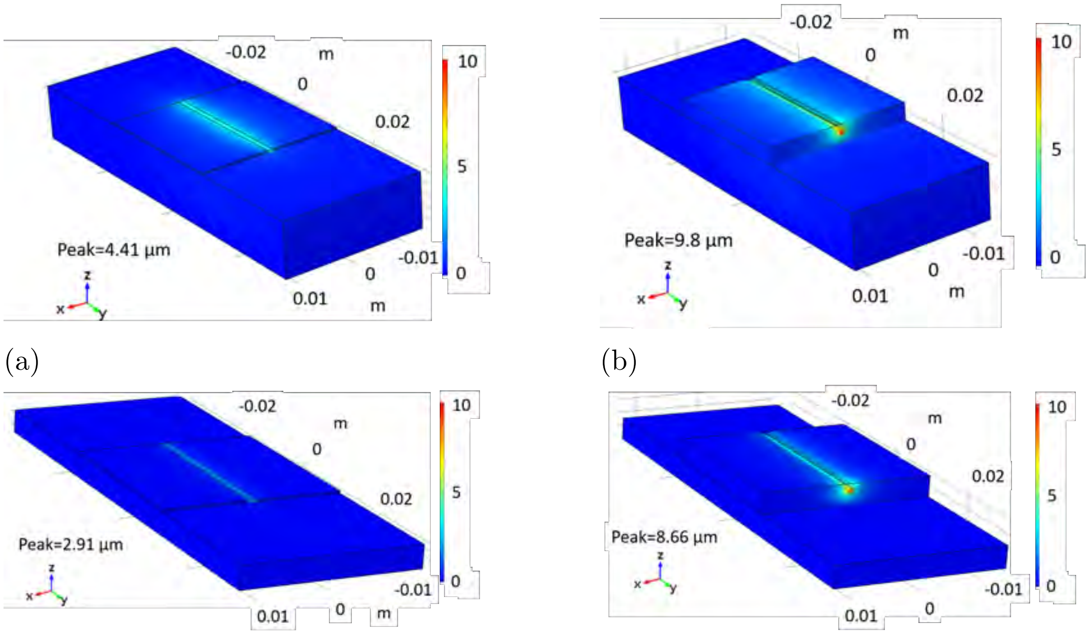
Peak=4.41 µm
Peak=9.8 µm
Peak=2.91 µm
Peak=8.66 µm
-0.02
0
0.02
-0.01
0
0.01
m
10
5
0
x
y
z

(a)

(b)

(c)

(d)

Figure 2.6: FE simulation of the UAM stack displacement for: (a) 2-layer and (b) 20-layer Al 6061-H18 stacks on a 9.53 mm (0.375 in) thick Al 6061-T6 baseplate with simulated K_{system}=433 MN/m and 364 MN/m, respectively; (c) 2-layer and (d) 20-layer Al 6061-H18 stacks on a 3.18 mm (0.125 in) thick annealed AISI 4130 steel baseplate with simulated K_{system}=772 MN/m and 455 MN/m, respectively.

Table 2.1: UAM weld parameters for welding Al 6061-H18 foil onto aluminum and steel baseplates.

Vibration Amplitude Setpoint (peak-peak)	(µm)	22.0
Weld Force	(N)	6000
Welder Travel Speed	(m/min)	2.54
Baseplate Temperature	(^{o}C)	93.3

Coefficients for the LTI model of the weld assembly were estimated using the procedure detailed in [35], which enables the estimation of the welder shear force from the vibration velocity and weld power measurements. The welder's vibration velocity was measured with a PSV-400 non-contact laser vibrometer at a sampling rate of 500 kHz and analyzed in the frequency domain with a block size of 8192 points. The fundamental frequency of the velocity signal (welder frequency) was estimated as the frequency corresponding to the peak amplitude of the short-time Fourier transform (STFT) of the signal with a frequency resolution of 9.5 Hz.

Figure 2.7 presents data for welding the second layer of aluminum foil using an aluminum baseplate versus a steel baseplate. It is shown that the welder frequency and welder's peak vibration velocity are nearly identical for both baseplates. On the other hand, the weld power and the estimated shear force are about 80% higher for the steel baseplate when compared to the Al baseplate. Weld power measurements and the corresponding simulated system stiffness values from the FE model are presented in Figures 2.8(a) and 2.8(b), respectively.

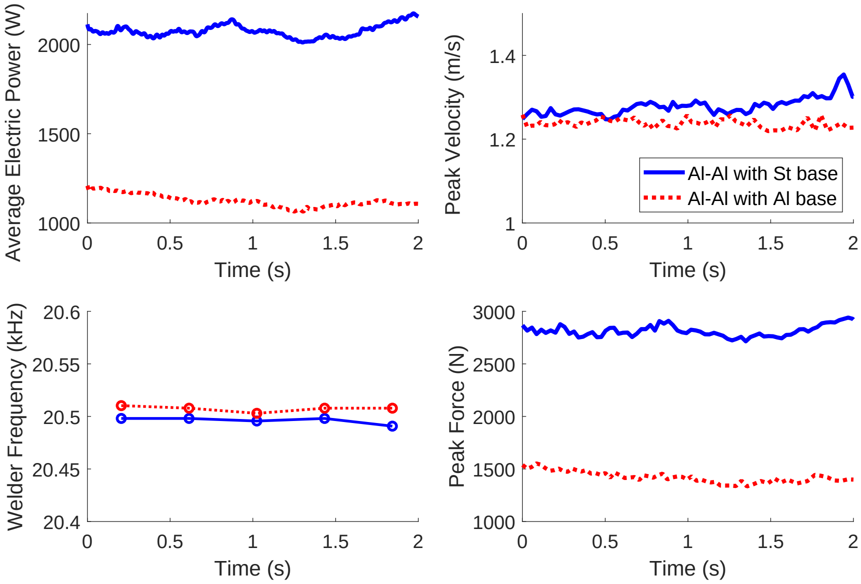

Figure 2.7: Comparison of in-situ measurements for welding the second layer of Al 6061-H18 foil with a 3.18 mm (0.125 in) thick annealed AISI 4130 steel baseplate versus a 9.53 mm (0.375 in) thick Al 6061-T6 baseplate. The peak force (welder shear force) is estimated from the weld power and welder's vibration velocity measurements using the LTI model of the weld assembly. The steel baseplate weld required greater power to achieve the prescribed welder vibration amplitude.

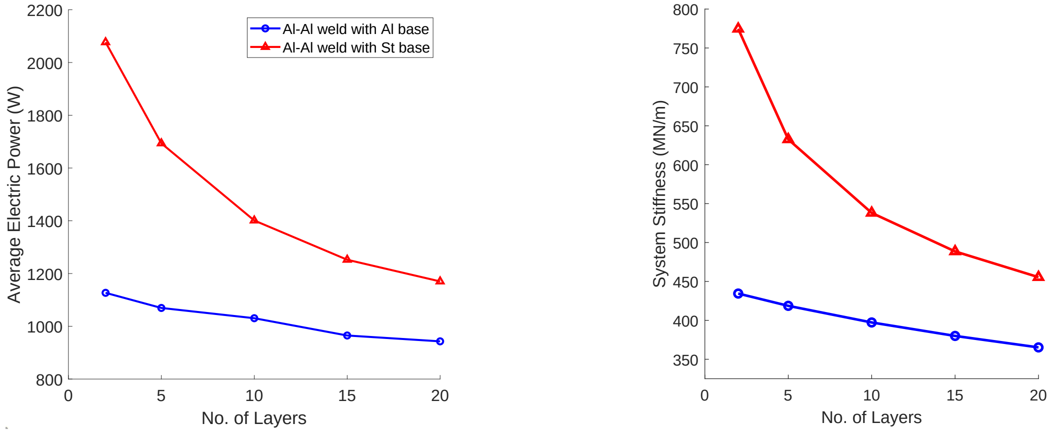

(a) (b)

Figure 2.8: Trends in weld power and stiffness with build height for the welding of Al 6061-H18 foil: (a) measured average electric power; (b) simulated effective stiffness K_{system} from (2.15) based on FE modeled stiffness of the stack and baseplate.

Parameter D_{loss} of the weld power model is calibrated based on weld power measurements for the 20-layer Al stack on the Al 6061-T6 baseplate. The squared errors between the weld power measurements and the model estimates are minimized using the fmincon routine in MATLAB to estimate D_{loss} to be 6100 N.s/m. This value of D_{loss} is then substituted into the non-linear expression for weld power, (2.11), to predict the weld power in Figure 2.9 for the different build heights on the steel baseplate. The $|x_{welder}|$ term in (2.11) is calculated as $|x_{welder}| = |\dot{x}_{welder}|/\omega_{weld}$ for the FFT magnitude of the welder's measured vibration velocity at the fundamental vibration frequency f_{weld}. For example, $|x_{welder}|$ corresponding to welding of the second Al 6061-H18 layer on the aluminum baseplate is calculated to be 17.7 μm. The decrease in displacement amplitude during welding is consistent with observations in [35]. A similar reduction in displacement amplitude is observed in many power ultrasonic processes under high loads, as detailed in [43].

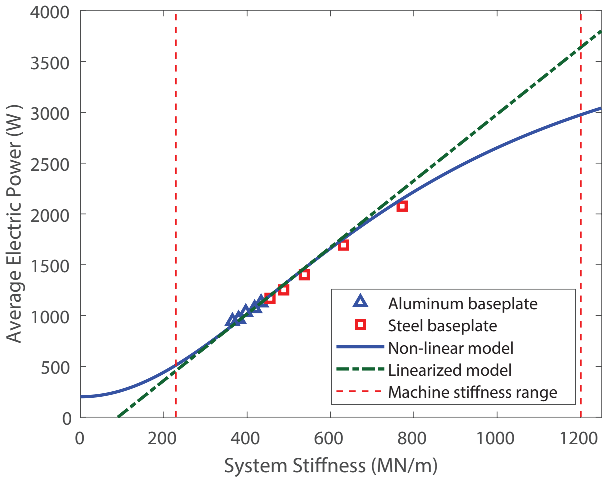

Figure 2.9: Experimentally measured average electric power plotted against the system stiffness estimated from the model for a 0.9 mm contact width. Data points for each baseplate are calculated from welds on consecutive layers, with progressively decreasing stiffness with build height. The non-linear model uses (2.11) and the linearized model uses (2.12) to estimate the average electric power, with parameter D_{loss} determined to be 6100 N.s/m from weld power data while welding the second Al 6061-H18 layer on the aluminum baseplate. The vertical lines show the range of system stiffness values expected for foil−foil welding using our welding setup.

The vertical lines in Figure 2.9 indicate the range of system stiffness values attainable for foil−foil welding in UAM using our welding assembly with standard materials and geometries. Assuming steel and aluminum as the most and least stiff materials used, and our typical range of baseplate thicknesses, the minimum and maximum typical system stiffness values are evaluated to be 229 MN/m and 1201 MN/m, respectively, using our vacuum chuck, shown in Figure 2.9.

The non-linear model and experimental results in Figure 2.9 show good agreement. The non-linear (2.11) and the linearized (2.12) models have estimated R-squared values of 98% and 96%, respectively, relative to the experimental data. The error can be attributed to a few model assumptions. One assumption is that there is no slip between the welder and the foil being welded. From (2.12), this leads to the model overpredicting the weld power, which is supported by Figure 2.9. The second assumption is that the contact width in UAM can be accurately estimated by Hertzian contact. Due to plasticity inherent in UAM, the true contact width could be higher, which would change the predicted system stiffness. The agreement between the model and experiments indicates that weld power can be estimated if the welder's vibration amplitude and system stiffness are known after calibrating the model with a calibration data set. Moreover, because input weld power is related to consolidation quality, this expression can be used to select an amplitude setting for adequate bonding for a given baseplate and chuck setup.

2.5.2 Study B: Effect of foil material stiffness on weld power

Table 2.2: UAM weld parameters for welding 10 layers of Cu C11000-O60 on an aluminum baseplate.

Vibration Amplitude Setpoint (peak-peak)	(µm)	32
Weld Force	(N)	6000
Welder Travel Speed	(m/min)	5.08
Baseplate Temperature	(^{o}C)	25

The influence of foil material stiffness on weld power is investigated in this study. Two copper foils are welded onto a 9.53 mm (0.375 in) thick Al 6061-T6 baseplate.

The stack was built using copper as the foil material because the estimated system stiffness does not significantly decrease with build height (less than 2% reduction for ten layers), in contrast to about a 9% reduction for ten layers of aluminum as the foil material. The stiffness values for a 2-layer Cu build are 11% higher than a corresponding 2-layer Al build on a Al 6061-T6 baseplate with the same thickness. A different sonotrode and transducer assembly was used for the work in Section 2.2, with different LTI model parameters and hence, different power-amplitude relationships.

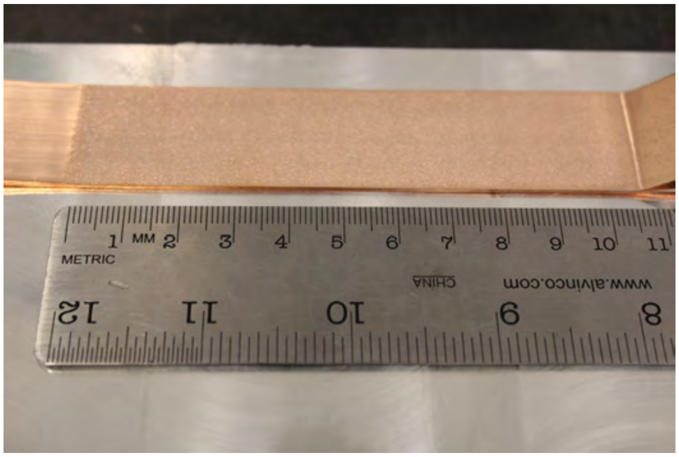

Figure 2.10: Ten-layer stack of Cu C11000-O60 foil welded onto a 9.53 mm (0.375 in) thick Al 6061-T6 baseplate.

Figure 2.10 shows a 10-layer Cu C11000-O60 stack welded onto a 9.53 mm (0.375 in) thick Al 6061-T6 baseplate. The corresponding system stiffness values as a function of build height, estimated from the FE model, are shown in Figure 2.11(a). The weld parameters shown in Table 2.2 were selected for good bonding, which means that the foil could not be peeled off by hand and there was no welding of copper to the sonotrode (nuggeting). The resulting weld power measurements are shown in Figure 2.11(b). The mean weld power values for the first ten layers are within 5% of each other. This study validates the hypothesis that system stiffness is the controlling variable for weld power at fixed process conditions. The D_{loss} value determined from Study A (6100 N.s/m) is used to estimate the weld power from (2.11). Although the D_{loss} value was determined for Al-Al welding, the model power estimates are within 10% of the weld power measurements. It is hence proposed that the damping parameter is independent of the foil material used, and this proposition is tested more rigorously in Study C for UAM with four different foil materials welded under the same process conditions.

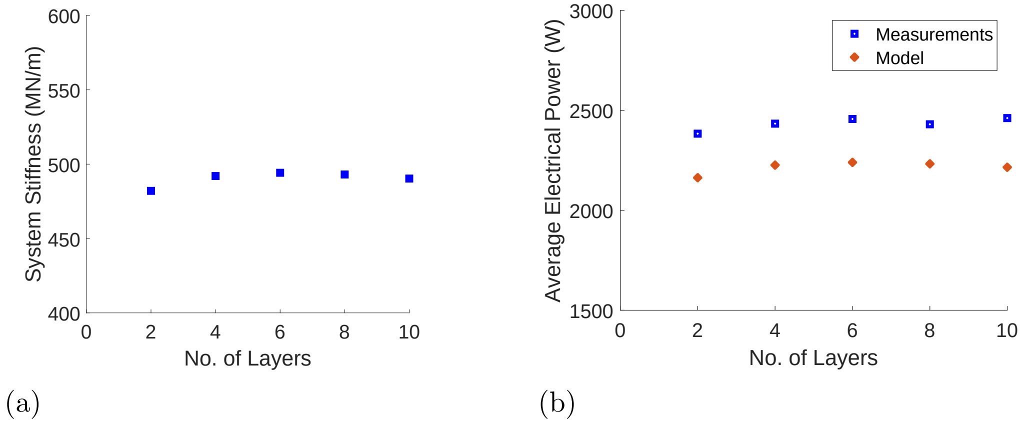

(a) (b)

Figure 2.11: Weld power and system stiffness values for welding 10 layers of 0.152 mm (0.006 in) thick C11000-O60 foils onto a 9.53 mm (0.375 in) thick Al 6061-T6 baseplate: (a) simulated effective stiffness K_{system} from (2.15) based on FE modeled stiffness of the stack and baseplate; (b) measured average electric power compared against predictions from the weld power model in (2.11).

2.5.3 Study C: Effect of foil material on model damping parameter

Table 2.3: Summary of foil tensile properties.

		Al 6061-H18	Al 6061-O	Al 3003-H18	Cu C11000-O60
Elastic Modulus	(GPa)	71	69	69	106
Yield Strength	(MPa)	237	55	185	107
Ultimate Strength	(MPa)	246	125	200	228
Elongation	(%)	3	25	4	25

The influence of foil material properties on weld power in the UAM process was studied by welding 2.54 cm (1.00 in) wide and 152 μm (0.006 in) thick Al 6061-H18, Al 6061-O, Al 3003-H18, and Cu C11000-O60 foils onto an Al 6061-T6 baseplate with the same peak-peak weld amplitude setpoint, weld force, and welder travel speed. These foils were chosen because they have substantial differences in their elastic moduli and yield strengths, which would affect the elastic and plastic response of the foil material during welding. Mechanical properties for Al 6061-O and Al 3003-H18 were obtained from the ASM materials handbook [44] for the respective alloy and temper combinations. Since the properties were not available in the literature, tensile properties for Al 6061-H18 and Cu C11000-O60 were measured by testing the foils in uniaxial tension using an MTS load frame with a digital image correlation (DIC) system for strain measurements. Table 2.3 summarizes the strength, stiffness, and elongation values for each foil material. The system stiffness for two layers of aluminum and copper foil welded on a 9.53 mm (0.375 in) thick aluminum baseplate

($K_{FEM,Al}$) are computed using (2.15) and summarized in Table 2.4. The copper weld foils have a higher system stiffness value due to their higher elastic modulus.

Table 2.4: Influence of foil and baseplate material on effective system stiffness (K_{system}) for 2 layers of foil welded onto a 9.53 mm (0.375 in) thick Al 6061-T6 baseplate. Stiffness units are (MN/m).

Foil Material	K_{chuck}	K_{FEM}	K_{system}
Aluminum	2000	555	434
Copper	2000	636	483

Table 2.5: UAM weld parameters for welding the second layer of all foil types with an Al 6061-T6 baseplate.

Vibration Amplitude Setpoint (peak-peak)	(μm)	12, 16, 20, ... 32
Weld Force	(N)	6000
Welder Travel Speed	(m/min)	5.08
Baseplate Temperature	(^{o}C)	25

Identical weld parameters were used to weld all of the foil types listed in Table 2.3 onto the same 9.53 mm (0.375 in) thick Al 6061-T6 baseplate, held in place on the CNC table using a vacuum chuck. Statistical techniques (ANOVA) have been used in [9] to demonstrate that weld force does not significantly influence weld quality in UAM of Al 6061; hence, it was fixed at a typical value of 6000 N. The travel speed of the welder was also fixed at a typical value of 84.67 mm/s (200 in/min). Two layers of each foil type were welded onto the baseplate one at a time. The first foil of all foil types was welded onto the baseplate using a 32 μm peak-peak weld amplitude setpoint, which was found to produce qualitatively acceptable welds for all of the foil types. A weld was considered to be acceptable if the welded foil could not be pulled off by hand. To understand the interrelation between the weld foil type and the UAM process, the welder's vibration amplitude and average weld power were measured in-situ during welding of the second foil.

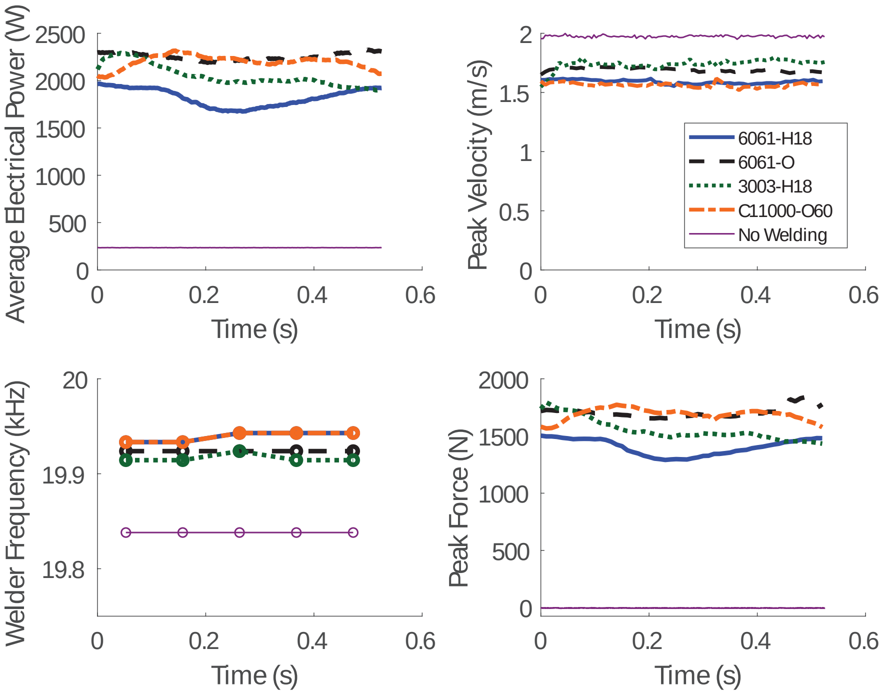

Figure 2.12: Measurements during welding of different metal foil types onto one another, i.e., foil−foil results, as well as the reference no welding condition. The first foil was welded onto a 9.53 mm (0.375 in) thick Al 6061-T6 baseplate. The power, peak velocity, frequency, and peak shear force profiles are similar in magnitude for all of the foil types. The welder frequency estimates for Al 6061-H18 and Cu C11000-O60 data overlap. Measurements are shown in the steady-state regions of the welds (at least 12.7 mm (0.5 in) away from start and end of each weld).

In Figure 2.12, the average electric power, peak vibration velocity, excitation frequency, and estimated shear force for the 32 μm peak-peak weld amplitude setpoint case are close to one another for all of the foil types. All of the data sets for welding cases are substantially different than those for actuating the welder under no load, which is consistent with earlier work in [35]. The similarities between the foils in Figure 2.12 are somewhat unexpected due to the large differences in foil strengths. For example, Al 6061-O has about a quarter of the tensile yield strength of Al 6061-H18, but draws about the same electrical power from the welder during welding of the second foil. Hence, we propose that weld power is mainly determined by the elastic compliance of the foil, workpiece, and fixture.

The second foil was welded onto the first foil using the range of peak-peak weld amplitude setpoints specified in Table 2.5. The span of values was chosen to provide a wide range of weld power and study both successful and unsuccessful foil−foil bonding. For example, no bonding was observed when attempting to weld the second foil of all foil types at the 12 μm peak-peak weld amplitude setpoint. The copper foil failed to bond successfully even at the 16 μm peak-peak weld amplitude setpoint. All of the foil types exhibit qualitative characteristics of good welds at the 32 μm peak-peak weld amplitude setpoint, shown in Figure 2.13.

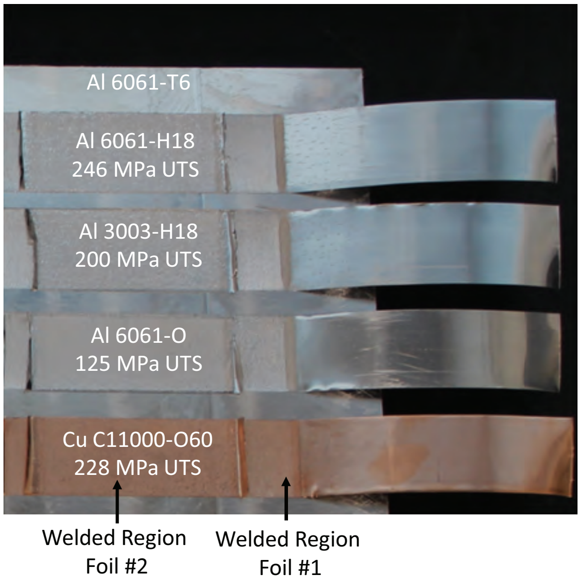
Al 6061-T6
Al 6061-H18
246 MPa UTS
Al 3003-H18
200 MPa UTS
Al 6061-O
125 MPa UTS
Cu C11000-O60
228 MPa UTS
Welded Region
Foil #2
Welded Region
Foil #1

Figure 2.13: Welded foils along with ultimate tensile strength (UTS) for reference. Two layers of each material were welded onto a 9.53 mm (0.375 in) thick Al 6061-T6 baseplate. Welds using a 32 μm peak-peak weld amplitude setpoint are shown here.

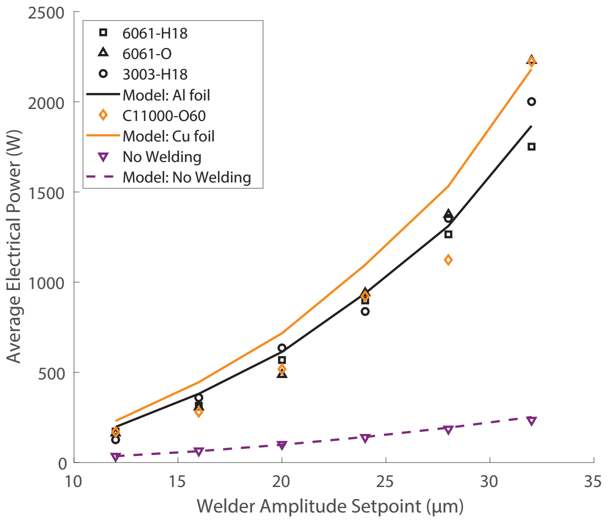

(a)

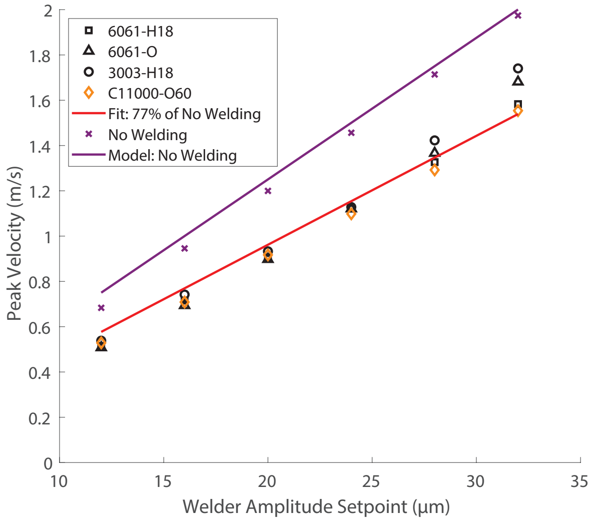

(b)

Figure 2.14: Measurements for attempting welding of different metal foil types onto one another, i.e., foil−foil results for welding the second foil to the first foil, as well as the no welding (actuated in air) condition for reference over a range of peak-peak weld amplitude setpoints. Model predictions are computed using the system stiffnesses of Al and Cu builds from Table 2.4 in (2.11). (a) Average electric power calculated by averaging the power measurements in the steady-state region of the weld (at least 12.7 mm (0.5 in) away from both the start and end of the weld). (b) Peak velocity of the vibration of the welder during welding and in air (no welding). The regression line between the peak velocity data in the no-welding cases and welding all the foils is shown. The least squares estimate of the slope value is 0.77, with an R-squared value of 98%.

It is known that weld power and peak-peak weld amplitude setpoint have a quadratic relationship under no load [35]. Modeling the welder's coupling with the materials being welded as a generalized dynamic mechanical stiffness, it is shown in (2.6) that the quadratic relationship holds even under load if the damping parameter is considered to be independent of weld amplitude, which is supported by the good fit between model predictions of weld power and the measured weld power in Figure 2.14(a) for all of the foil types. The D_{loss} parameter determined from Study A (6100 N.s/m) and the peak velocity measurement during welding are used to estimate the weld power from (2.11). The agreement between model and experiment also supports our proposition that the mechanical strength of the foil material does not significantly affect the weld power for foil−foil welding. It is also observed from Figure 2.14(a) that the weld power-amplitude relationship is not strongly affected by whether successful foil−foil bonding is achieved.

Based on the findings in Section 2.5.3, we develop a procedure to determine the amplitude setpoint required to achieve a target weld power for different build configurations. It is necessary to estimate the vibration amplitude of the welder under load as a function of the amplitude setpoint to use in (2.11). A linear regression model is developed between the peak velocity for the no welding cases and the peak velocity for welding all the foils, assuming zero Y-intercept. Using the method of least squares, the best-fit slope of the model is found to be 0.77, and the best-fit regression line is shown in Figure 2.14(b).

The weld power model (2.11) is combined with the following simplifying assumptions: welder's vibration amplitude under load is 77% of the amplitude under no load; the frequency shift due to welding is small compared to the ringing frequency, hence

$\omega_{weld} \approx \omega_{ring}$; the value estimated for parameter D_{loss} in this study (6100 N.s/m) applies to other UAM systems. Hence, the amplitude setpoint to achieve the target power is calculated from (2.11) to be

$$|x_{welder}| = \frac{1}{0.77\omega_{ring}} \sqrt{\frac{2P_{e,avg}^{weld}}{\left(D_t + D_{loss}\frac{K_{system}^2}{K_{system}^2 + (\omega_{ring} D_{loss})^2}\right)}}. \tag{2.16}$$

Relationship (2.16) serves as a tool to determine process settings to achieve a target power level with UAM for different workpiece and fixture combinations. Since power has been shown to strongly influence weld quality [15], this tool saves the UAM user from costly and time-consuming trial welds and testing to tune weld parameters. For example, if one determines that approximately 3000 W of average electric power is required to produce a strong bond between two metal foils, the target weld power and the estimated system stiffness for a given workpiece and fixture can be substituted into (2.16) to estimate the welder amplitude setpoint required to achieve the target weld power and weld quality.

2.6 Conclusions

A lumped parameter LTI model of the UAM welder coupled to the materials being welded during UAM has been developed to predict the weld power at a given weld amplitude as a function of the overall system's compliance, considering the contributions of the foil material being welded, the workpiece being welded onto, and the fixture. The non-linear relationship between weld power and system stiffness has been presented, along with a linearized relationship that has been shown to provide a good approximation. Prior to this study, predictive relations for UAM weld power have not been successfully developed.

Modal analysis and finite element modeling are used to estimate the different component compliances, and an equivalent circuit model is used to describe the overall system's compliance, which is then used to compute the weld power for a given weld amplitude setting. The model shows good agreement with measurements for a variety of build and fixture configurations tested: up to 20 layers of Al welded onto baseplates with different stiffnesses; up to 10 layers of Cu welded onto an Al baseplate; and a 2-layer build with different alloys and tempers of Al and Cu foil. Model predictions of higher weld power for stiffer (lower compliance) builds agree with experimental data. Weld power is also found to be largely insensitive to foil type (and hence foil strength) within the Al foils, although different welder effort is required to satisfactorily weld different foil types. A framework has been developed to determine the weld amplitude setpoint to obtain a target weld power for a given build configuration.

These observations support the conclusion that the elastic compliance of the system has the most dominant influence on weld power. This modeling framework, using a calibrated damping coefficient, can predict the weld amplitude required to reach a certain target weld power for different welder, workpiece, and fixture designs. This reduces the need for time-consuming pilot weld studies for new UAM build materials, configurations, and systems.

Chapter 3

In-situ Measurements for Quality Monitoring and Process Control

Overview

This chapter details the setup of process measurements analyzed in the frequency domain to enable an in-situ bond tracking system using a Doppler velocimeter to track the velocity profile of the welded foil. This setup is used to develop a relationship between the dynamic vibration velocity behavior and weld quality. The setup is also capable of in-line weld quality monitoring, and possibly defect identification. A metric is developed to distinguish successful and unsuccessful welding in an automated system.

3.1 Introduction

In-situ process measurements can be crucial to develop closed-loop process control techniques to improve the reliability and adoption of new manufacturing processes. In-situ process measurements have been setup to enable process control in ultrasound-assisted gas metal arc welding [45], resistance spot welding [46], ultrasonic metal welding [47], wire bonding [48], and many other manufacturing processes. Using in-situ fast fourier transform (FFT) computation is also commonly used for computing metrics used for monitoring manufacturing processes, such as etching in [49].

Foil vibration velocity has been used as a qualitative metric using phase difference between signals for successful UAM bonding [50] using thick foil (twice as thick as the standard 0.15 mm feedstock). Multiple single-point laser vibrometer were required to facilitate the method. Improved in-situ process measurements of the welding process can enable in-line quality monitoring for UAM. There has been some work on using in-situ non-destructive methods for detecting delamination in welds during the UAM process [51]. In this section, in-situ electrical measurements using a high-frequency data acquisition system will be used in conjunction with foil vibration velocity measurements to define a binary metric capable of distinguishing between successful and unsuccessful welding.

3.2 Measurement setup

3.2.1 In-situ electrical measurements

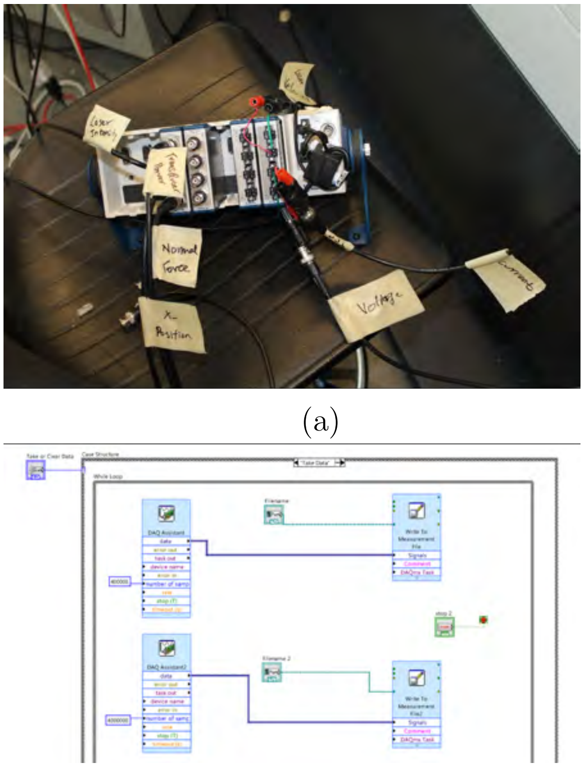
Laser Intensity
Normal Force
X-Position
Voltage
Current
Take or Clear Data
Case Structure
"Take Data"
While Loop
DAQ Assistant
data
error out
task out
device name
error in
number of samp
rate
stop (T)
timeout (s)
Filename
Write To Measurement File
Signals
Comment
DAQmx Task
stop 2
DAQ Assistant2
Filename 2
Write To Measurement File2

(a)

(b)

Figure 3.1: Measurement setup: (a) Weld power, weld speed, weld force, voltage, and current to the transducers are acquired using National Instruments cDAQ-9178 for in-situ process measurements; (b) LabVIEW program used for storing the collected data on a Windows PC.

The operating frequency of the welder is close to 20 kHz, and hence a high-frequency data acquisition system (DAQ) is required to record, store, and process these high frequency signals (laser velocity measurements, transducer voltage and transducer current measurements) for process monitoring. To this end, an NI 9222 high-speed

DAQ with a 500 kHz sampling frequency is used, as part of a c-DAQ 9178 module as seen in Figure 3.1(a). For slower varying signals such as feed table position and weld normal force, an NI 9234 module with a 50 kHz sampling frequency is used in conjunction with LabVIEW to record and process the signals, shown in Figure 3.1(b). All signals are synchronized to the same clock. The signals are listed in Table 3.1.

The transducer electrical power draw analog output measured from the controller of the Dukane transducer has an update rate of 2 kHz. This corresponds to approximately one data point every 10 harmonic cycles of the welder vibrations at 20 kHz. Voltage and current signals during welder operation were measured to provide an instantaneous estimate of the power draw. This provides a more accurate estimate of the electrical energy input into a section of weld. This is important in calibrating the energy flow models to relate the flow of energy from the electrical input to the weld microstructure. The motion of the feed table is commercially measured from the analog output from the CNC machine that has an update rate of about 7.5 Hz, reducing the resolution in the position measurement at a given time for a weld speed of 84.67 mm/s (200 in/min) to be 10.16 mm (0.4 inch). To track the precise location to locate defects identified, a better position tracking system such as a motion capture system with an update rate of 120 Hz can be used to improve the resolving ability of the feed table position to within 0.51 mm (0.02 inch).

3.2.2 In-situ Doppler velocimetry

Vibration velocity of as-received Al-6061 foil stock that is 152 μm thick during the weld process was measured. Previous work in [50] required the use of thicker foil (300 μm) to enable accurate positioning of the laser. A positioning technique was developed using a commercial macro lens of appropriate aperture, and a lighting system to enable imaging of the precise laser spot location with a camera. A macro lens is used for the camera as it better illustrates the features of the order of 100 μm, which is the range of interest. A low exposure time of 1/4000, aperture size F10, and ISO 100 with manual focus were the settings used for capturing the images. The laser spot was centered near the welder contact region, and positioned on the weld foil using the servos in the vibrometer, and confirmed by taking an image, shown in Figure 3.2.

The normal force setpoint is set to 6000 N, and the welding program is initiated. The welding program moves the welder downward until the set-force is reached. Using the CNC feed gain-control knobs, this process is slowed down and the stopped when the force read by the welder load cell reaches 5000 N, the set point for the actual weld. T This ensures that the laser spot is positioned on the weld foil. The focused laser spot size is approximately 74 μm at the closest feasible standoff distance, and hence the spot can focus on a single foil to measure it's velocity. The resolution of movement using the software is 0.001° both in the vertical and horizontal plane.

Table 3.1: Signals measured using the NI cDAQ 9178.

Module	Update rate (kHz)	Signal
NI 9222	500	Laser spot velocity
	500	Voltage across slave transducer
	500	Current through slave transducer
NI 9379	50	Electrical power to transducers
	50	X-position of feed table
	50	Normal force measured from load cell

Using the geometry laser, the distance of the welder to the laser head is calculated to be close to 0.930 m. This corresponds to a 16.23 μm resolution for the laser spot.

As foil vibration velocity and transducer voltage are measured in the same experiment, their relative phase, and other rich information about the harmonic content of these signals will be processed to obtain a metric for in-line monitoring of the process and to calibrate FE models of the UAM process.

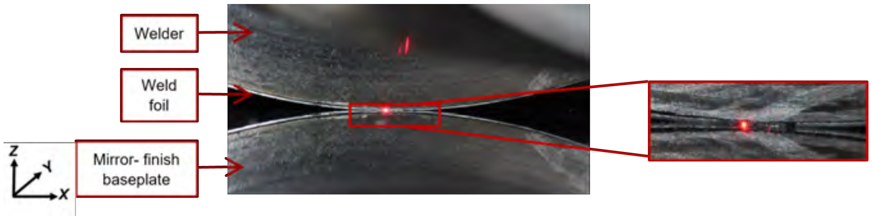

Figure 3.2: Focused image of welder and foil before welding taken with a macro lens and lighting system. The welder is applying the set weld normal force on the baseplate. The baseplate is machine flat and hence has a mirroring effect in the image. The zoomed image shows the laser spot completely positioned within the foil.

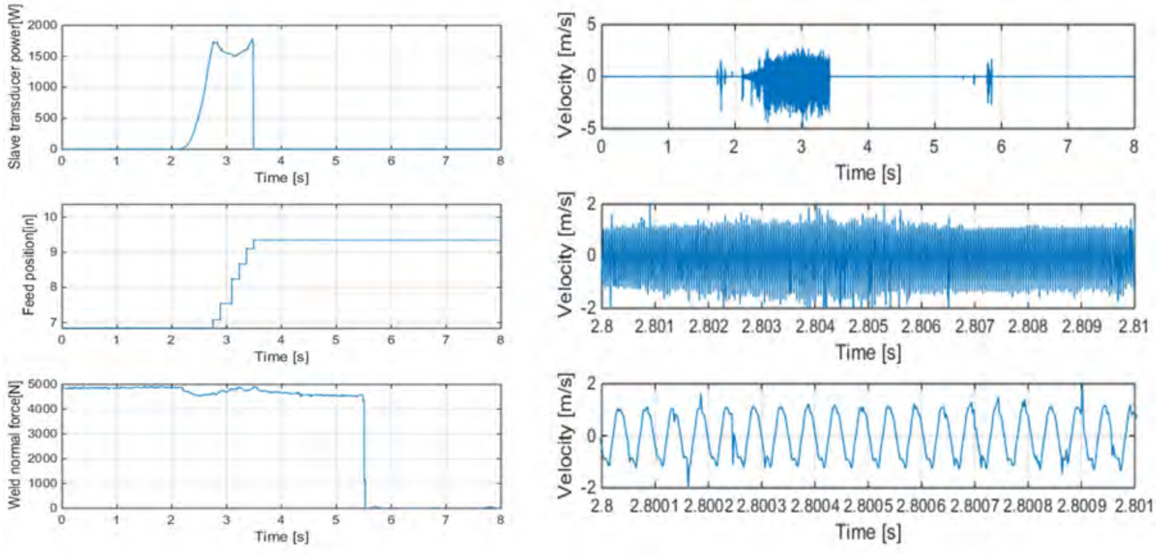

Figure 3.3: Representative data for a Al 6061-H18 foil-foil weld using the following weld parameters: 32 µm weld amplitude, 5000 N weld force, 84.67 mm/s (200 in/min) weld speed. The velocity plots on the right show that the foil vibration velocity is also a sinusoidal signal with some noise artifacts due to issues maintaining focus on the foil.

3.3 Weld quality assessment using Doppler velocimetry

The scanning feature of the laser vibrometer was used to create a 10x2 grid to measure the foil−foil relative velocity during UAM welding as seen in Figure 3.4. The density and number of points is limited by the resolution of the laser servo, and the delay to move the laser from one scan point to the next (20 points takes 4 seconds, although the scan time is only 50 ms x 20 = 1 s at 2.56 MHz).

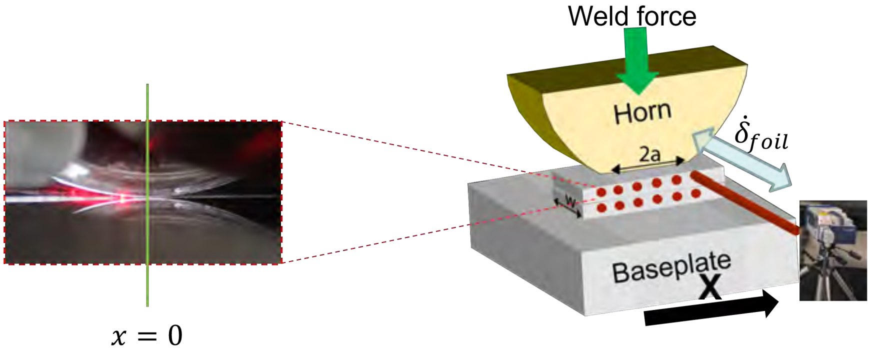

Figure 3.4: A Polytec PSV-400 scanning vibrometer is used to measure the velocity profile of the foils being welded using UAM. A grid of points are defined in the Polytec software, and the laser spot sequentially measures the vibration velocity at the given location.

In-situ foil velocity measurements as shown in Figure 3.4 were conducted during the welding of Al 6061-H18 foil using a fixed weld force of 5000 N, and weld speed of 84.67 mm/s (200 in/min). In the measurements in Figure 3.5(a), a clear asymmetry is seen in the measured velocity profile in the case of a successful weld (32 μm weld amplitude), with three clear demarcated zones of frictional slip between the foils being welded. In case of insufficient weld amplitude for welding, as is the case with the process conditions: 12 μm weld amplitude, 5000 N weld force, 84.67 mm/s (200 in-/min) weld speed, the foil velocity follows the velocity of the welder, and the entire contact region is a region of frictional slip.

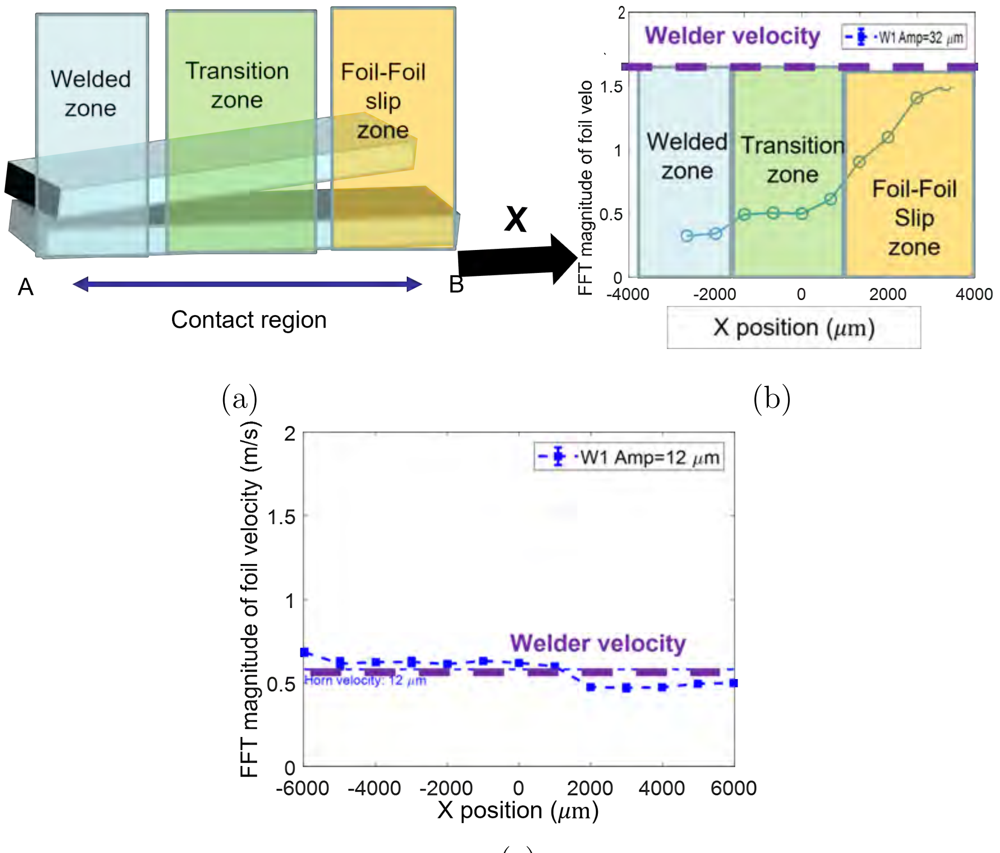

(a) (b)

(c)

Figure 3.5: Different slip regimes identified during the welding of Al 6061-H18 welded onto an Al 6061-T6 baseplate: (a) illustration of the welded zone (bottom surface of the foil being welded sticks to the workpiece), slip zone (the foil-foil interface has a constant slip velocity), and the transition zone in-between for a successful weld; (b) the three zones marked on a plot of the velocity profile for a successful weld (32 µm weld amplitude, 5000 N weld force, 84.67 mm/s (200 in/min) weld speed); (c) the velocity profile of an unsuccessful weld with insufficient weld amplitude (12 µm weld amplitude, 5000 N weld force, 84.67 mm/s (200 in/min) weld speed) where the entire contact region is the slip zone.

The velocity magnitude of the foil approaches that of the welder for increasing X-position, seen in Figure 3.5(b). The welded zone is the region trailing the welder

($x < 0$) with highly non-sinusoidal velocity and many stick-slip events, seen in Figure 3.6(a). The vibration speed of the foil in the welded zone is much lower than that of the welder.

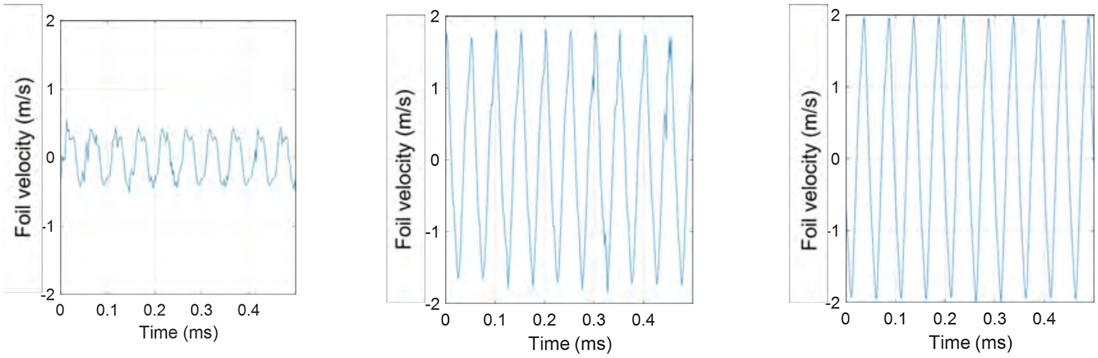

(a) (b) (c)

Figure 3.6: The velocity of the foil being welded at different positions: (a) welded zone; (b) transition zone; and (c) slip zone, as defined in Figure 3.5. The velocity of the foil in the slip zone approaches that of the welder, whereas that in the welded zone is non-sinusoidal and has higher harmonics, indicating non-linear stick/slip behavior.

The asymmetry in the velocity profile is observed for all successful welds of Al 6061-H18. Welds were considered successful when a welded foil could not be pulled off by hand. To test the hypothesis that this asymmetry will also be observed in successful welding of any material, Cu C11000-O60 foil with the same dimensions were welded onto the Al 6061-T6 baseplate using identical weld parameters by varying the weld amplitude with otherwise identical weld parameters. The threshold weld amplitude for bond formation was identified to be 20 μm. The foil velocity profile is normalized by the welder's vibration velocity, and plotted against the weld amplitude used for Al 6061-H18 and Cu C11000-O60 in Figure 3.7(a) and Figure 3.7(b), respectively.

A metric θ is defined to quantify the asymmetry to be:

$$\theta = \frac{\int_S \left(1 - \dot{\delta}_{foil}(x)/\dot{\delta}_{welder}\right) dx}{\int_S dx}, \tag{3.1}$$

where S denotes the contact region over which the velocity measurements were conducted. The metric is normalized so that $\theta = 0$ for unsuccessful welds when the foil and welder vibration velocities are close to each other (that is, $\dot{\delta}_{foil}(x) = \dot{\delta}_{welder}$ for $-a < x < a$), and there is no welded zone, and $\theta = 1$ for a hypothetical successful weld where the entire contact width of the foil is stuck to the previously welded foil or workpiece (that is, $\dot{\delta}_{foil}(x) = 0$ for $-a < x < a$). Here it is assumed that the velocity of the previous foil is small when compared with the vibration velocity of the welder.

The expression in (3.1) is computed for the different weld amplitudes tested to obtain the metric as a function of weld amplitude in Figure 3.7(c). It is seen that a threshold θ value of 0.25 can be used as a threshold to distinguish successful and unsuccessful welding process conditions. Note that this method cannot distinguish between the weak and strong welds once the threshold weld amplitude is reached. This technique can be used for an automated weld parameter search algorithm to determine if adequate weld quality was achieved without user intervention, detailed in Figure 3.8.

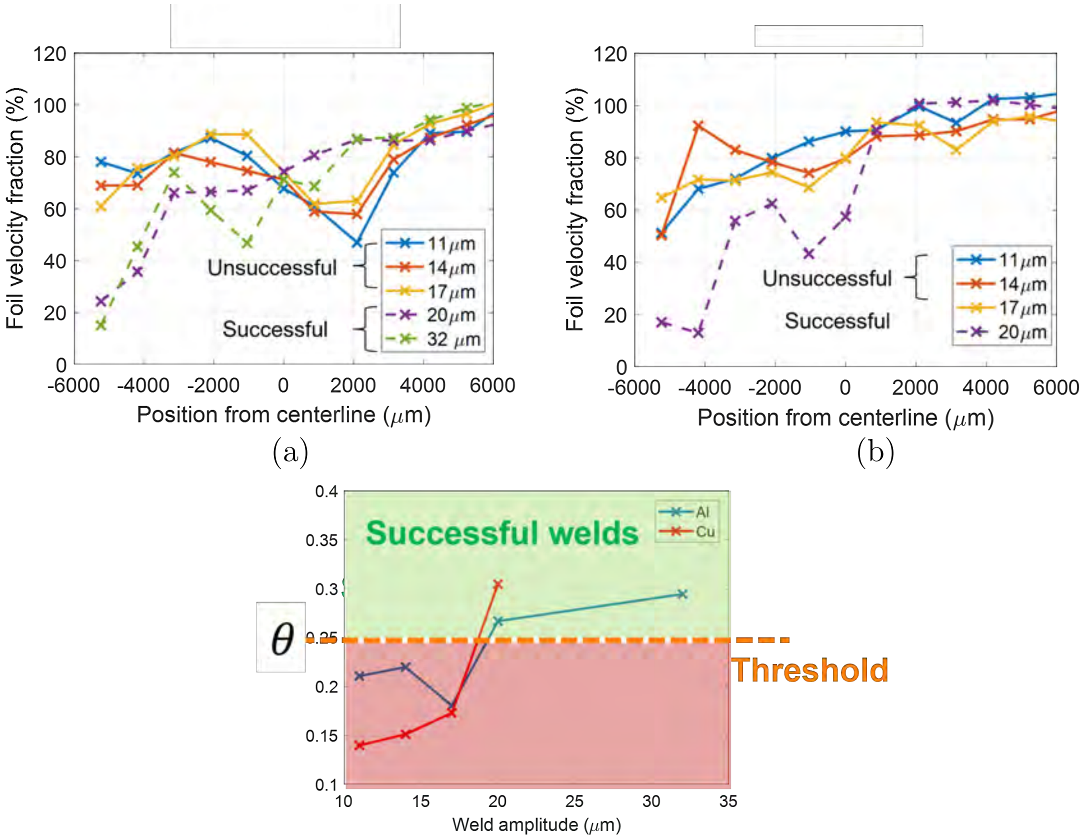

(a) (b)

(c)

Figure 3.7: Normalized velocity profile for different weld amplitudes for the UAM of: (a) Al 6061-H18, (b) Cu C11000-O60. (c) Metric θ defined in (3.1) to quantify the degree of asymmetry in the foil velocity profile.

3.4 Conclusions

A new experimental technique was developed to track the in-situ vibration velocities of either the weld stack, welder, or the standard 0.152 µm-thick weld foil used during the UAM process. This is the first-time that UAM foil velocity and transducer voltage during welding have been measured synchronously, and this will assist in real-time tracking of the UAM process, and better understand the in-situ velocity dynamics between the two foils being welded during UAM. This understanding is key to quantifying the energy dissipated due to friction in UAM as a function of process parameters.

The in-situ bond tracking technique developed using a Doppler velocimeter has been used to correlate dynamic vibration velocity behavior with bond quality. This was used to develop a weld quality monitoring setup with possible applications in the areas of in-line quality control and defect identification for UAM. This approach can also be used to enable closed-loop process control by monitoring the metric θ in-situ.

A binary indicator for weld quality for UAM was developed using laser Doppler velocimetry, and validated for the UAM of Al 6061-H18 and Cu C11000-O60 foils. It was found that using a threshold value of 0.25, the metric developed can reliably identify successful and unsuccessful UAM welds in-situ, and can be used to support an automated weld parameter search as detailed in Figure 3.8.

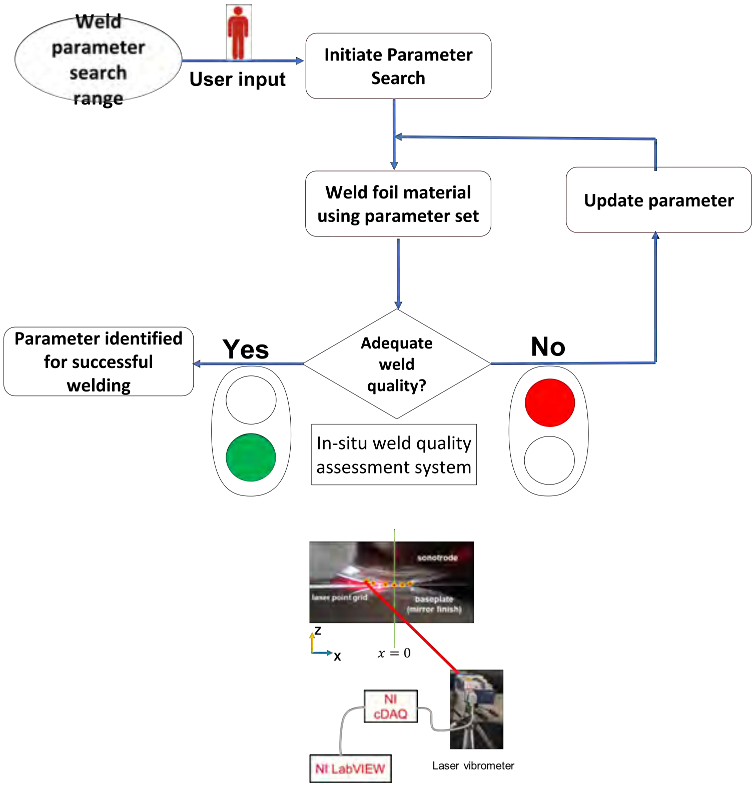
Weld parameter search range
User input
Initiate Parameter Search
Weld foil material using parameter set
Update parameter
Adequate weld quality?
Yes
No
Parameter identified for successful welding
In-situ weld quality assessment system
sonotrode
laser point grid
baseplate (mirror finish)
z
x
x = 0
NI cDAQ
NI LabVIEW
Laser vibrometer

Figure 3.8: Algorithm for parameter search using the weld quality detection technique identified in Figure 3.5.

Chapter 4

Investigation of Microstructural Energy Storage using EBSD and Hardness Testing

Overview

The chapter details the investigation on the effect of process variables on the resultant microstructure of the built-up part. The degree of recrystallization is quantified, and an energy metric, defined using the Read-Shockley relationship, is used to build an energy map of the welded part. The total energy stored in the resultant weld interface microstructure is quantified, and trends with weld parameters are studied. The effect of subsequent weld layers on the microstructure is also studied.

4.1 Introduction

The microstructure of structures built by UAM has been extensively investigated using EBSD. Such investigations in the UAM of aluminum alloys [52, 17, 53, 54] have shown that the weld interface comprises of a small, mostly equiaxed recrystallized grains. Recrystallization was observed to only occur at very local interface regions due to the local shear deformation, while the bulk region of each layer still remains unaffected. The extensive grain refinement at the metal-metal interfacial bonds was attributed in [55] to the continuous dynamic recrystallization process which is driven by the high strain rate plastic deformation and associated adiabatic heating at temperatures below 50% of the melting point of the constituent metals.

The

It has been also been shown that during the UAM of dissimilar metals, although the formation of brittle intermetallics is suppressed due to the lower formation temperature, there can be some metal interdiffusion during the process [56]. There has also been work on quantifying the amount of grain growth that occurs during the ultrasonic welding of nano-crystalline materials as a function of weld pressure and weld time [57]. Ion-channeling contrast imaging using a focused ion beam (FIB) has also been conducted for Al 3003-H18 to discover thin bands of nanograins near the welder and the modification in the grain morphology is explained by the accumulative thermomechanical processes due to sequential bonding of foils in [58]. Some studies such as [59] qualitatively analyzed SEM scans of UAM-ed Al 1100-O samples fabricated using different process parameters but neither a quantitative analysis to compare the samples nor any quantification of stored energy was conducted.

Two key metrics obtained from the EBSD analysis are the mean grain diameter and fraction of high angle (>15 degrees) grain boundaries [60]. The raw EBSD data can be re-analyzed to yield a substantial amount of quantitative information about grains, subgrains, grain boundaries [61]. Open-source toolboxes such as MTEX in MATLAB provide versatile functions to import, analyze and visualize diffraction EBSD data to estimate an orientation density function, to compute texture characteristics, to model orientation density functions, to simulate pole figure or EBSD data, and to manipulate pixel-level EBSD data directly [62].

The energy stored in the microstructure can be quantified from EBSD scans using the Read-Schockley equation, as shown for the accumulative roll bonding (ARB) process in [63]. The thermodynamic aspects of the conversion of cold working due to plastic deformation into stored energy in the microstructure is detailed in [64]. The stored energy in manufacturing processes such as rolling can be characterized using SEM and TEM [65].

This chapter discusses the use the EBSD (electron backscatter diffraction) and SEM (scanning electron microscopy) techniques to understand the effect of UAM process parameters on the dynamic recrystallization process during bond formation. The energy stored in the weld interface microstructure is also quantified to compare to the input energy of the process. To this end, two studies are conducted. The first study investigates the effect of subsequent weld layers on the microstructures of the previously welded UAM weld interface, up to 9 additional layers. The second study investigates the effect of two key process parameters, weld amplitude and weld speed, on the weld interface microstructure to better understand the flow of energy in the process from the electrical input to the microstructure. Nanoindentation is also used to verify the location and size of the weld interface region with recrystallized grains.

4.2 Electron backscatter diffraction (EBSD) and Nanoindentation analysis

4.2.1 EBSD technique

EBSD is performed in a scanning electron microscope (SEM), utilizing the tool to create an array of diffraction patterns that are captured on a detector. A diffraction pattern is captured at every point in the SEM scan, which are then indexed and the crystal orientation at each point is determined. For EBSD, a very carefully polished sample is required, which is obtained by polishing sections of UAM-ed samples using 0.05 μm colloidal silica solution. EBSD is an excellent tool for measuring crystal orientations and symmetry. The measurements are limited by the EBSD resolution of 2 μm, and hence smaller grains cannot be resolved using the detector. This will lead to an underestimation of the stored energy due to the smoothing algorithm used.

4.2.2 Quantitative analysis

For data cleanup and processing, the MTEX toolbox by Ralf Hielscher was used (https://mtex-toolbox.github.io/). The MTEX toolbox within MATLAB is used to process the raw data to obtain quantitative metrics: grain size distribution, misorientation angle distribution, and stored energy. It is also used to denoise and smooth the data to plot inverse pole figure (IPF) maps and grain boundary mapping. Single mis-indexed pixels were deleted and reconstructed together with single nonindexed pixels. The raw scan data from the EBSD detector has many regions with low confidence due to systematic noise, and hence contains many points that are not indexed (about 0.4%) or with low (<5%) confidence index (17%). Non-indexed areas less than two pixels wide were filled during noise removal using a half-quadratic filter. The alpha coefficient for the filter was chosen to by 0.25 and the level was chosen to be 3. A subgrain detection algorithm was used to identify the grain boundaries. A minimum subgrain size of 3 pixels and a boundary misorientation threshold of two degrees were used. A grain boundary is identified as a high-angle grain boundary (HAGB) if the misorientation between the neighboring pixels exceeds 15 degrees. Figure 4.1 shows these HAGBs in red and the other boundaries in black. The interface region is observed to have a high concentration of HAGBs.

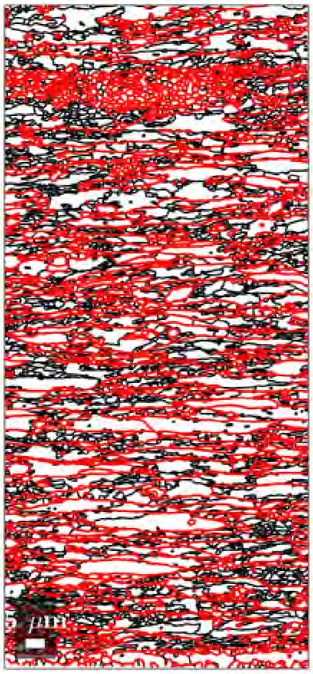

Figure 4.1: Using a cutoff angle θ_m of 15 degrees, low (LAGB) and high (HAGB) angle boundaries can be distinguished. HAGBs are shown in red and LAGBs in black. The minimum threshold size for a grain is 2 pixels. The UAM interface is seen near the top as a collection of dense HAGBs.

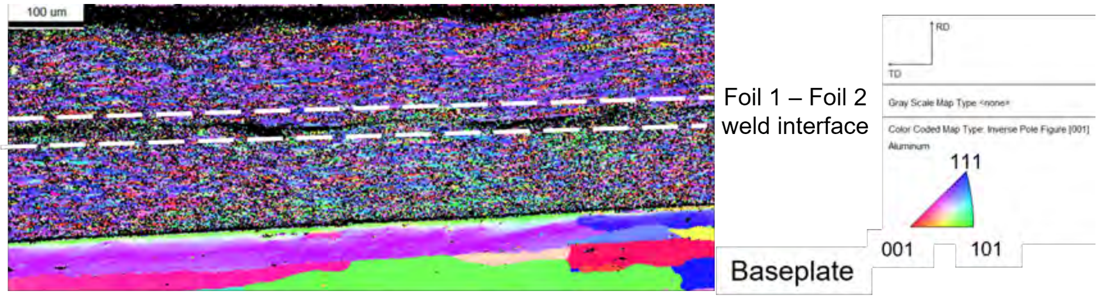
100 um
Foil 1 – Foil 2
weld interface
Baseplate
RD
TD
Gray Scale Map Type: <none>
Color Coded Map Type: Inverse Pole Figure [001]
Aluminum
111
001
101

Figure 4.2: The un-smoothed inverse pole figure (IPF) shows the point-by-point orientation of the sample. The 2-layer Al 6061-H18 sample was fabricated on an Al 6061-T6 baseplate using the following settings: 29 μm weld amplitude, 5000 N weld force, and 84.67 mm/s (200 in/min) weld speed. Black regions are areas that did not provide a high-confidence data fit. The different colors denote the different orientations of each pixel.

Figure 4.2 illustrates a visualization of the microstructure of the UAM weld interface in Al 6061-H18 where the different colors denote the different orientations of each pixel. The SEM imaging work was done with the help of collaborators at Battelle Memorial institute. The weld interface is approximately 15 μm tall. The bulk region of the foils away from the interface retains its pre-weld elongated microstructure typical of as-received rolled foil. For the weld interface in the sample shown in Figure 4.2, the mean grain diameter was 0.72 μm and the fraction of high angle grain boundaries was 0.66. There have been attempts at modeling the grain diameter d post-UAM using the Zener-Holloman parameter Z_h which found that the subgrain size was related to the strain rate $\dot{\varepsilon}$ and the temperature T as follows [66]:

$$d = (-0.6 + 0.08 Z_h)^{-1}, \tag{4.1}$$

$$Z_h = \dot{\varepsilon} \exp \frac{18772}{T}. \tag{4.2}$$

Using the value for typical strain rate (10000 /s) and temperature for the UAM of Al 6061-H18, the grain size estimated is 0.24 μm. This mismatch is attributed to the limit of the EBSD detector (0.25 μm) and the minimum pixel size of 2 per grain, and the background noise in the backscatter image near the weld interface due to the severe deformation.

4.2.3 Weld interface identification

The location of the weld interface needs to be determined quantitatively from the raw EBSD data. The fraction of indexed points was found to be a reliable metric to determine this location since the interface has severely deformed material with small recrystallized grains some of which can be smaller than the 2 μm resolution of the detector, which leads to many points not being indexed accurately. To this end, a 2-μm window is spanned across the sample to identify the interface center. The corresponding fraction of indexed points is shown in Figure 4.3. The width of the interface was identified by iterating over increasing widths from the center point until an inflection point was obtained in the mean grain size within the region.

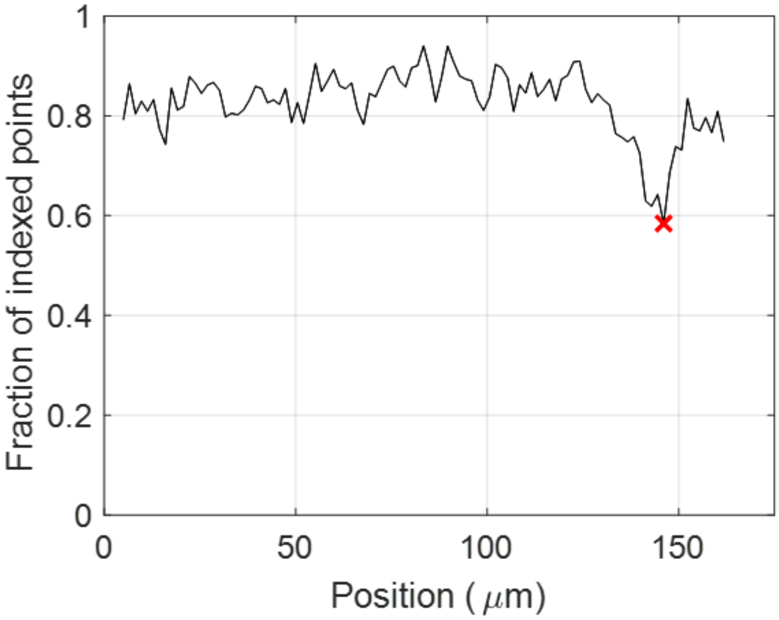

Figure 4.3: Interface location identified with a red cross using the location of the minimum of the fraction of unindexed points.

4.2.4 Nanoindentation for interface identification

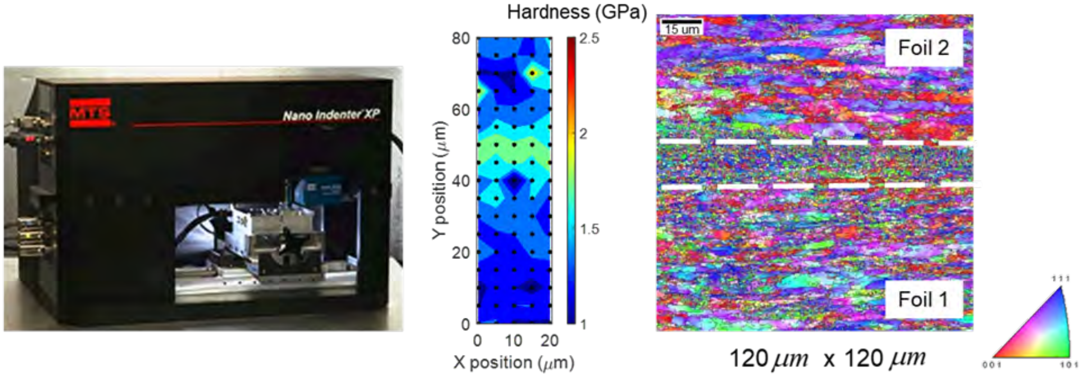

(a) (b) (c)

Figure 4.4: Measurement of local hardness of UAM-welded Al 6061-H18: (a) MTS Nano Indenter XP with a Berkovich indenter used to perform nanoindentation; (b) map of local hardness measured with a spacing of 5 µm; (c) Inverse Pole Figure (IPF) from EBSD analysis of a UAM weld with the weld interface region shown using dashed white lines.

A nanoindentation study was conducted to characterize the local hardness increase of the Al matrix near the foil 1–foil 2 weld interface in UAM builds. Previous work on hardness mapping of Al 3003-O / SiC composite matrices fabricated using UAM discovered that the harness increase near the interfaces of welds matched with the expected increase due to refined grains using the Hall-Petch relationship [67]. Nanoindentation has also been used as an alternative to microscopy to identify intermetallic compounds in laser joining processes in [68] from local hardness increases. The method has applications beyond measuring hardness, and can be used to measure the local yield strength and Young's modulus [69]. It was found in [70] that the yield stress of Al 6061-T6 alloy used in electric arc are directly comparable between indentation and micro-traction experiments.

The minimum spacing between indents is determined by the polishing particle diameter (0.05 µm), and was computed to be 3 µm. Another factor to consider is ISE or indent size effect which is a hardness-depth relationship observed for most materials that exhibit artificially higher hardness measurements at low penetration depths of the indenter into the material. This dependence can be very different for different alloys of steels, brass, and aluminum [71], and hence a study needs to be conducted to determine the appropriate indent size. This effect can be more pronounced in softer materials like aluminum [72]. To this end, an array of indentations were created on a Al 6061-T6 baseplate using loads ranging from 0.4 gf to 50 gf. The hardness of the baseplate was found to plateau for a indentation depth of 2 µm, and hence a 0.4 gf load was chosen which results in an indent spacing resolution of 5 µm.

The resulting hardness map is shown in Figure 4.4(b), where the Al 6061-T6 baseplate in the bottom has the highest hardness values, and a clear 10-15 µm-wide interface region is observed between the two Al 6061-H18 weld foils with higher hardness when compared to the surrounding bulk material. The size of the weld interface region matches the weld interface width estimate from EBSD analysis (14 µm) seen in Figure 4.2.

The weld interface region was observed to have a measurably higher hardness than bulk foil, which is expected from the Hall-Petch relationship due to the small equiaxed grains. The bulk Al 6061-H18 material hardness is identical to the as-received foil hardness value since the H-18 temper is 100% cold-worked, and cannot be further work-hardened by the thermo-mechanical processes in UAM. It is expected that the bulk hardness of annealed materials such as Al 6061-O will increase post-UAM.

4.3 Estimation of energy storage in the microstructure

4.3.1 Study A: Effect of subsequent weld layers

Al 6061-H18 samples with 2, 3, 5, and 10 layers were welded onto a 12.7 mm (0.5 inch) thick Al 6061-T6 baseplate using identical UAM process conditions: 32 µm weld amplitude, 5000 N weld force, and 84.67 mm/s (200 in/min) weld speed. The thickness of the 25.4 mm (1 inch) wide foil feedstock is 0.152 µm. The objective of the study is to investigate the effect of subsequent weld layers on the weld interface microstructure. The samples were sectioned as shown in Figure 4.5.

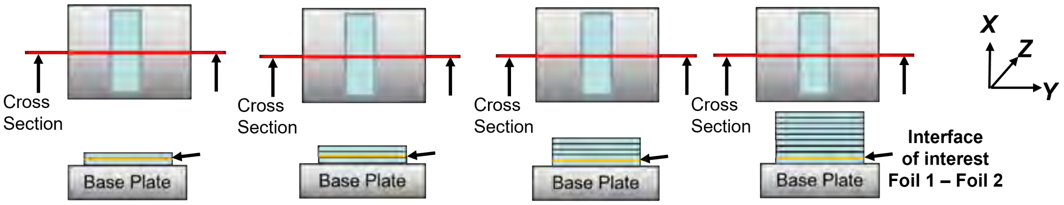
Cross Section
Base Plate
Cross Section
Base Plate
Cross Section
Base Plate
Cross Section
Base Plate
Interface of interest Foil 1 – Foil 2
X
Z
Y

Figure 4.5: Samples fabricated with 2, 3, 5, and 10 layers of Al 6061-H18 foil UAM-ed on a 12.7 mm (0.5 inch) thick Al 6061-T6 baseplate to study the effect of subsequent weld layers on the weld interface microstructure.

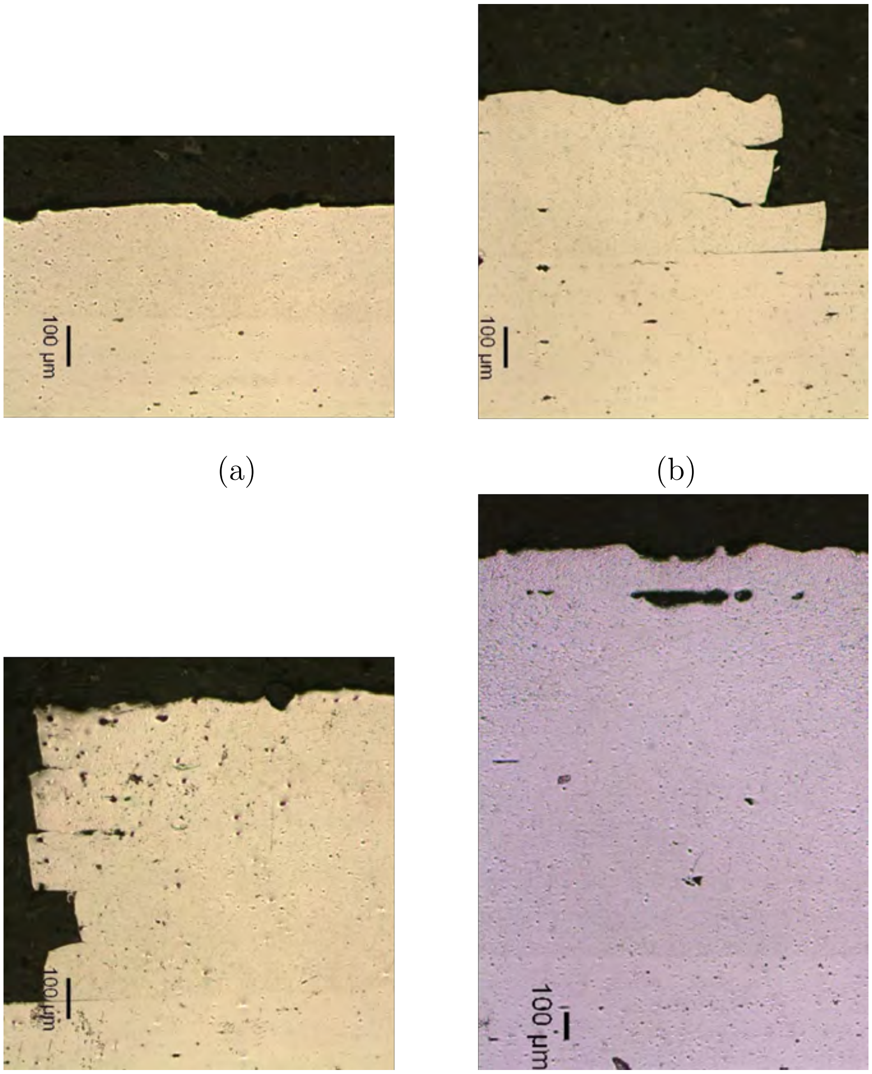

(a) (b)

(c) (d)

Figure 4.6: Optical images of (a) 2-, (b) 3-, (c) 5-, and (d) 10-layer Al 6061-H18 welds constructed on a 12.7 mm (0.5 inch) thick Al 6061-T6 baseplate using weld parameters: 32 μm welder amplitude, 5000 N weld force, and 84.67 mm/s (200 in/min) weld speed.

Figure 4.6 show cross-section images of the four samples taken using an optical microscope. The Al 6061-T6 baseplate and the Al 6061-H18 foils can be distinguished by the difference in color due to the difference in precipitates (seen as black spots) in the aluminum matrix. Voids are not observed between the first and second foil in all the samples. A large void is seen in the foil 9 - foil 10 interface for the 10-layer sample but that may be attributed to poor weld quality in taller builds due to lack of power compensation [15].

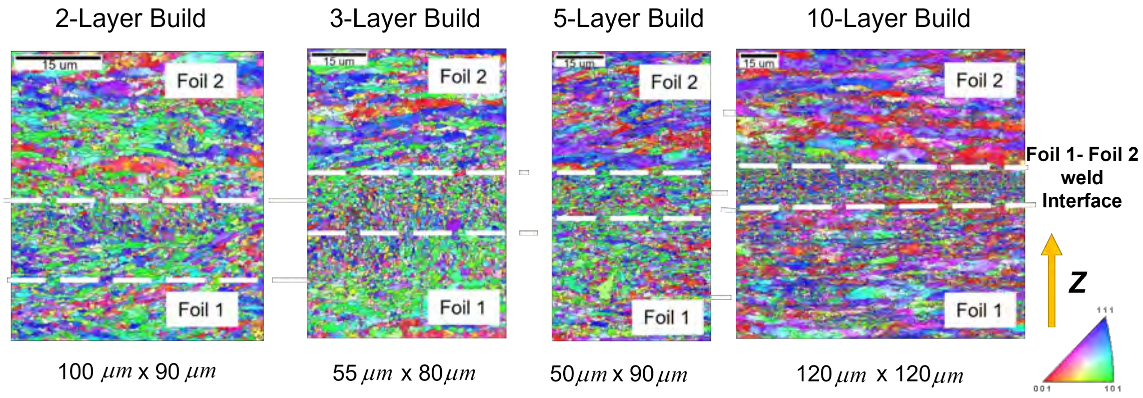
2-Layer Build
3-Layer Build
5-Layer Build
10-Layer Build
15 um
Foil 2
Foil 1
Foil 1- Foil 2 weld Interface
Z
111
001
101
100 μm x 90 μm
55 μm x 80μm
50μm x 90μm
120μm x 120μm

(a) (b) (c) (d)

Figure 4.7: Inverse pole figures of (a) 2-, (b) 3-, (c) 5-, and (d) 10-layer Al 6061-H18 welds constructed on a 12.7 mm (0.5 inch) thick Al 6061-T6 baseplate using weld parameters: 32 µm welder amplitude, 5000 N weld force and 84.67 mm/s (200 in/min) weld speed. The centerpoint of the interface was identified from Figure 4.3, and the approximate weld interface region is shown using dotted white lines.

EBSD analysis was conducted to quantify differences in the weld interface microstructure between the first and second foil welded due to subsequent layers being welded using a detector with a point resolution of 0.25 µm. Inverse pole figures (IPF) are a visual representation of grain orientations and grain boundaries. The IPF plots in Figure 4.7 show a dense collection of refined grains at the foil-foil weld interface. The grains away from the interface retain their as-rolled texture and are elongated along the direction of rolling.

Figure 4.8(a) shows that the histograms of grain sizes near the weld interface for the four samples are very similar, which indicates that the deformation due to subsequent welding does not induce further grain refinement in the foil 1 − foil 2 interface. The mean grain size seen in Figure 4.8(b) is also similar for all the samples at around 0.7 μm. Figure 4.9(a) compares the misorientation angle distribution with the theoretical Mckenzie distribution for equiaxed grains and it is found that the four samples have similar misorientation angle distributions. The zoomed image in Figure 4.9(b) shows that there is an increase in the fraction of grains with higher misorientations with their neighbors when compared to the that expected for rolled foil material.

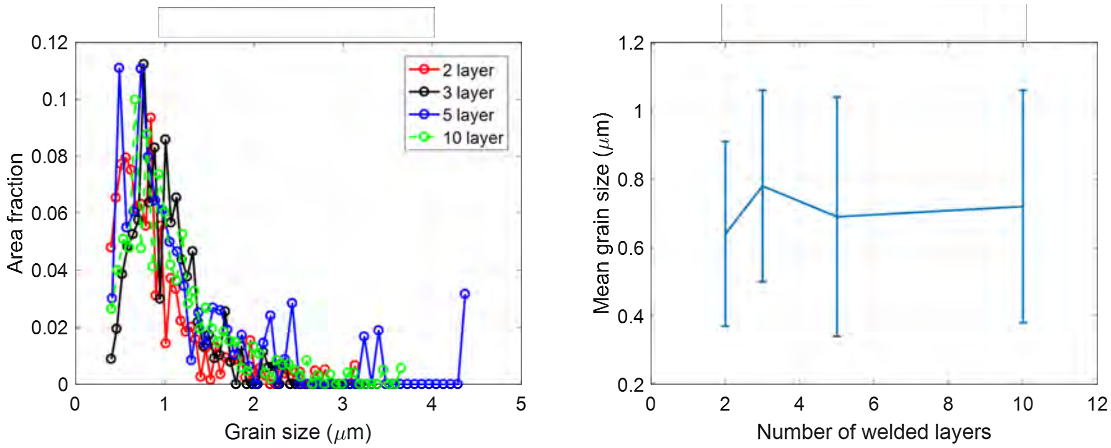

(a) (b)

Figure 4.8: Analysis of the size distribution of grains in the 2-, 3-, 5-, and 10-layer samples: (a) Histogram of the area of the grains vs. the grain size near the weld interface; (b) Mean grain size near the foil 1 - foil 2 weld interface plotted vs. the total number of layers welded.

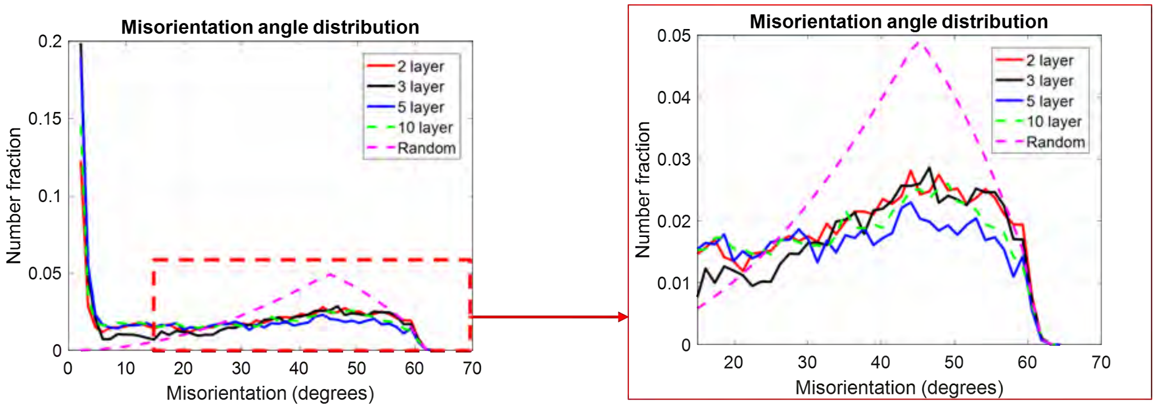

(a) (b)

Figure 4.9: Analysis of the misorientation angle distribution of grains in the 2-, 3-, 5-, and 10-layer samples: (a) Histogram of the number of the grains vs. the misorientation angle near the weld interface; (b) Zoomed-in section with higher misorientation angles showing a peak for all the samples with similar distributions.

Table 4.1: Summary of the welding trials.

	2-layer	3-layer	5-layer	10-layer
Mean grain diameter in weld interface (μm)	0.64	0.78	0.69	0.72
Standard deviation of grain diameter (μm)	0.27	0.28	0.35	0.34
Interface width (μm)	12	12	16	16
% High angle grain boundaries (HAGB)	71	66	60	66

Grain refinement and misorientation are direct indicators of the degree of recrystallization, hence mean grain diameter and fraction of HAGBs in the weld interface region are used as a comparison metric in Table 4.1. Interface width shows a slight increase for the 5 and 10-layer samples, but given that the resolution of the EBSD detector is 2 μm, the interface width can be assumed to be constant at 14 μm. Average grain diameter does not significantly increase, and the differences between the cases are within error bounds. Proportion of high angle grain boundaries, a metric of recrystallization, is also within 10% variation from the value for the 2-layer sample. Within the range of parameters tested, no significant difference in the microstructure was detected using mean grain diameter and fraction of HAGBs as metrics. Using these metrics, the effect of subsequent welds on the weld microstructure of Al 6061-H18 UAM builds is not significant up to 10 layers of build up.

4.3.2 Study B: Effect of process settings

The objective of this study is to quantify the effect of UAM process parameters on the weld interface microstructure by measuring the energy stored in the microstructure. Trends between weld parameters used and the energy stored in the microstructure are obtained to guide mapping the energy flow in the UAM process from the input electrical energy to the weld interface microstructure. To this end, Al 6061-H18 UAM samples with 2 layers were prepared and in-situ process signals were measured for 10 different parameter sets, varying welder vibration amplitude and weld speed. Weld force was not varied based on previous work in [9] showing no statistical dependence of weld strength on weld force.

The weld force was thus fixed at a value of 5000 N. The lowest welder vibration amplitude at which stick occurs was found to be 21 μm. Hence, 23 μm was chosen as the lowest parameter value for amplitude of welder vibration. The upper limit of weld amplitude was chosen to avoid the sticking of the foil to the welder (nugget formation), which is observed at 35 μm. The nominal weld speed was chosen as 84.67 mm/s

(200 in/min), and values were chosen on either side covering the operating parameter range of use, up to 179.92 mm/s (425 in/min). Weld speeds above 211.67 in/min are not typical.

Sample fabrication

The length of each weld was 63.5 mm (2.5 inches). The weld foil is 0.152 μm thick, 25.4 mm (1 inch) wide Al 6061-H18. The Al 6061-T6 baseplate on which the foil was welded is 9 mm (0.35 inch) thick. Before welding, the baseplate was machined flat using a 25.4 mm (1 inch) diameter steel end-mill with a spindle speed of 5000 RPM at a feed rate of 63.5 mm/s (150 in/min). A single layer of foil was welded to the machined baseplate, and then a second layer was welded on top of the first layer. Both welds were made using the same weld parameters.

The first set of welds was processed by fixing the weld normal force at 5000 N, and the weld speed at 84.67 mm/s (200 in/min). The weld amplitude is varied between 23 μm and 35 μm, shown in Figure 4.10(a). The weld amplitude of 32 μm is the optimal value found for Al 6061-H18 foil on a 9 mm (0.35 inch) thick Al 6061-T6 baseplate [9]. The weld speeds were varied by fixing the weld amplitude at 29 μm as shown in Figure 4.10(b). Transverse sections were cut such that the normal to the plane of cutting was along the rolling direction of the welder during fabrication. The sections were characterized using SEM and EBSD (Electron Backscatter Diffraction). A sample inverse pole figure is seen in Figure 4.2. The raw EBSD data was then analyzed using the MTEX toolbox in MATLAB.

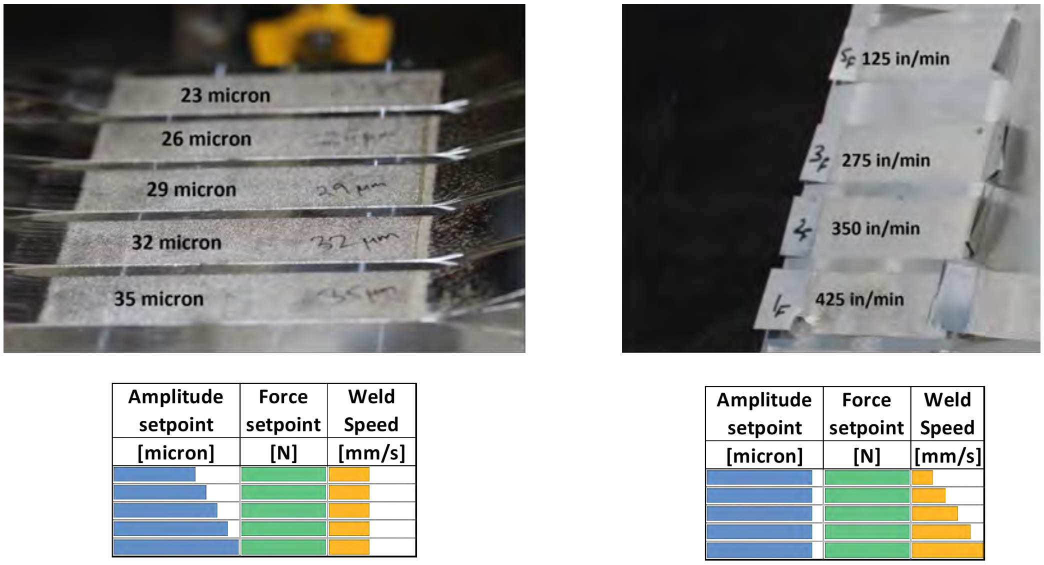
23 micron
26 micron
29 micron
32 micron
35 micron
125 in/min
275 in/min
350 in/min
425 in/min
Amplitude setpoint [micron]
Force setpoint [N]
Weld Speed [mm/s]

(a) (b)

Figure 4.10: Study to determine the effect of UAM process settings on the weld interface microstructure at a fixed weld force of 5000 N: (a) Weld amplitude varied by fixing the weld speed at 84.67 mm/s (200 in/min); (b) Weld speed varied by fixing the weld amplitude at 29 μm.

In-situ process measurements

Weld power, weld speed, weld force, voltage and current to the transducers are acquired using National Instruments cDAQ-9178 for in-situ process measurements. Two DAQ modules on an NI c-DAQ 9178 record the relevant signals. A NI 9222 module records signals sampled at 500 kHz and a NI 9239 module records signals sampled at 50 kHz, shown in Figure 4.11. All signals measured by a single DAQ module are synchronous. For this study only the NI 9239 signals were used. Input energy per unit length of the weld, E_{ip}, is expressed as a function of the electrical power input and the traversal speed of the workpiece as

$$E_{ip} = \frac{\text{Electrical power input}}{\text{Weld speed}}. \tag{4.3}$$

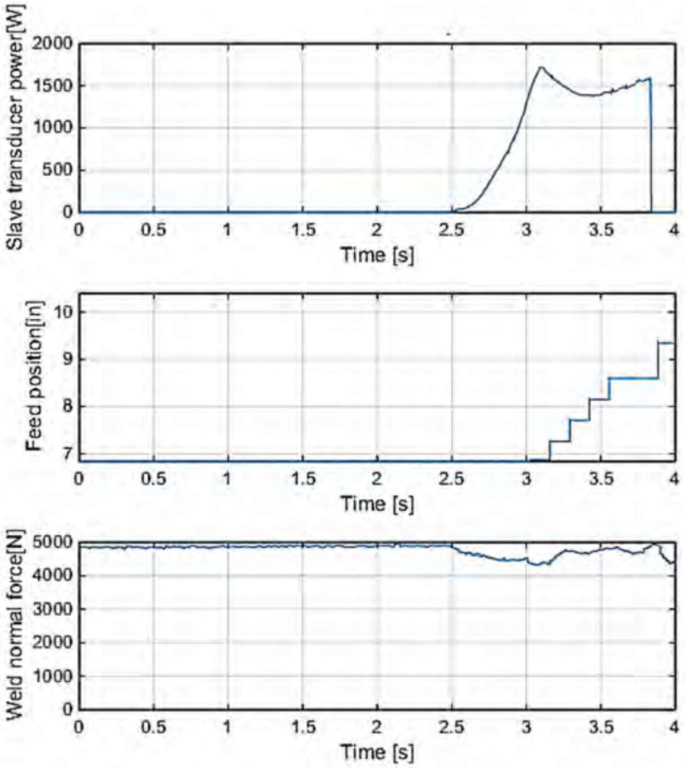

Figure 4.11: Weld power, X-position of the workpiece, and weld force as recorded by NI 9239 sampled at 50 kHz using weld parameters: 35 µm welder amplitude, 5000 N weld force and 84.67 mm/s (200 in/min) weld speed.

Stored energy estimation

The stored energy in the microstructure S was computed using the Read-Schockley equation, to be

$$S = \sum_{\theta} \Omega_{GB}.\gamma_{GB}. \begin{cases} \frac{\theta}{\theta_m}(1 - \ln \frac{\theta}{\theta_m}), & \text{if } \theta \leq \theta_m \\ 1, & \theta > \theta_m \end{cases}, \tag{4.4}$$

where θ is the angle of misorientation between a boundary pixel and its neighboring pixels, γ_{GB} is the grain boundary energy density of aluminum (=0.324 J/m^2 [73]),

Ω_{GB} is the cross-section area. The value for pure aluminum is used and the effect of alloying elements and precipitates are ignored. The expression for the area assumes spherical grains, which is appropriate for the equiaxed grains in the weld interface region. The procedure to obtain the stored energy in the microstructure is detailed in Figure 4.12.

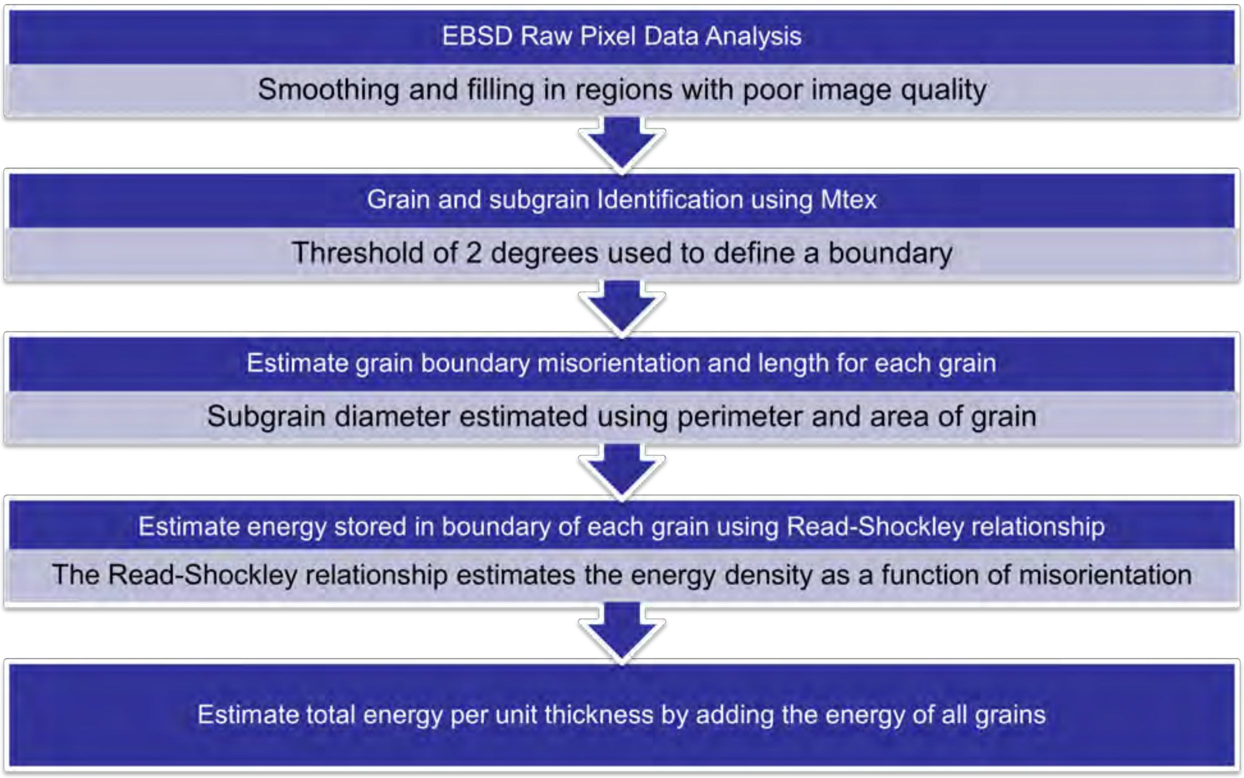
EBSD Raw Pixel Data Analysis
Smoothing and filling in regions with poor image quality
Grain and subgrain Identification using Mtex
Threshold of 2 degrees used to define a boundary
Estimate grain boundary misorientation and length for each grain
Subgrain diameter estimated using perimeter and area of grain
Estimate energy stored in boundary of each grain using Read-Shockley relationship
The Read-Shockley relationship estimates the energy density as a function of misorientation
Estimate total energy per unit thickness by adding the energy of all grains

Figure 4.12: Flowchart showing the method to calculate energy stored in the microstructure from raw EBSD data.

The energy values per unit length (in J/m) plotted were calculated by adding the GB energy throughout the thickness of the UAM sample, with a peak near the weld interface, and deducting the GB energy in the as-received material of the same thickness, which was flat (or homogeneous). That is, stored GB energy = (GB energy in the UAM material) − (GB energy in the as-received material). Grains at the interface with low scan quality were not indexed (noisy), and were smoothed by the data analysis, which leads to underestimation of the stored energy.

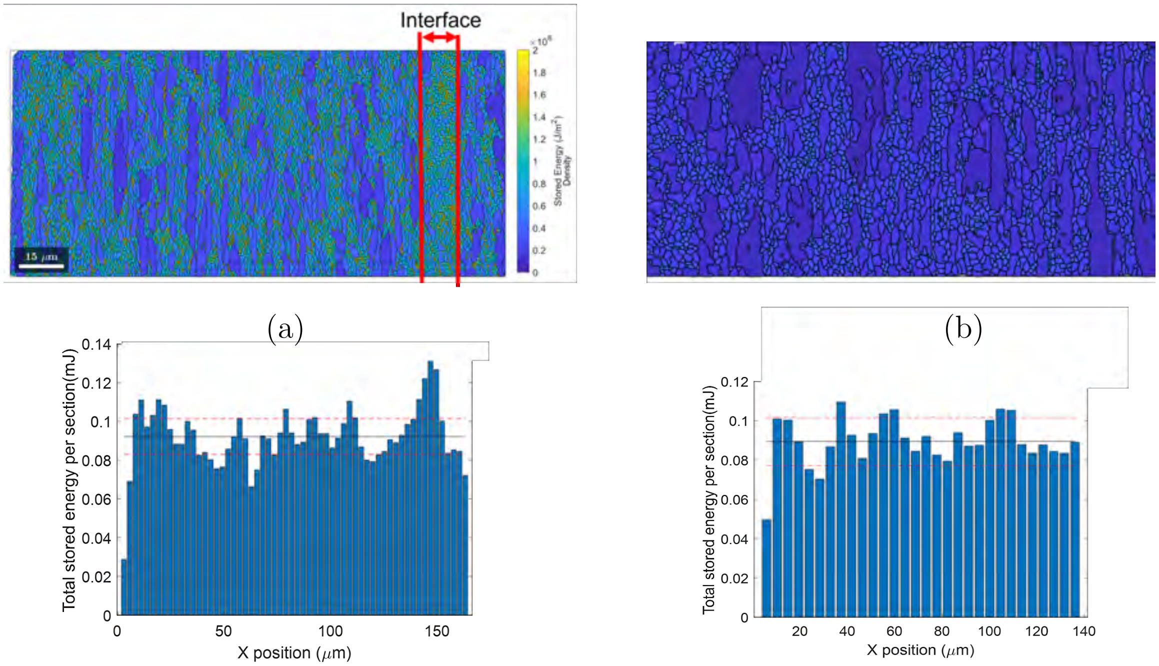

(a) (b)

(c) (d)

Figure 4.13: Comparison of post-UAM microstructure to control: (a) Stored energy map for sample prepared using 23 μm weld amplitude; (b) Histogram of stored energy showing a peak near the weld interface; (c) Stored energy map for the as-received rolled foil (control) showing elongated grains with low misorientations; (d) Histogram of stored energy for the control.

The stored energy profile for the UAM sample prepared using 5000 N weld force, 84.67 mm/s (200 in/min) weld speed and 23 μm weld amplitude was compared against the as-received control foil in Figure 4.13. A clear peak at the weld interface which was

10% above the mean energy was observed in the energy histogram in Figure 4.13(c), unlike the flat stored energy profile of the control sample in Figure 4.13(d).

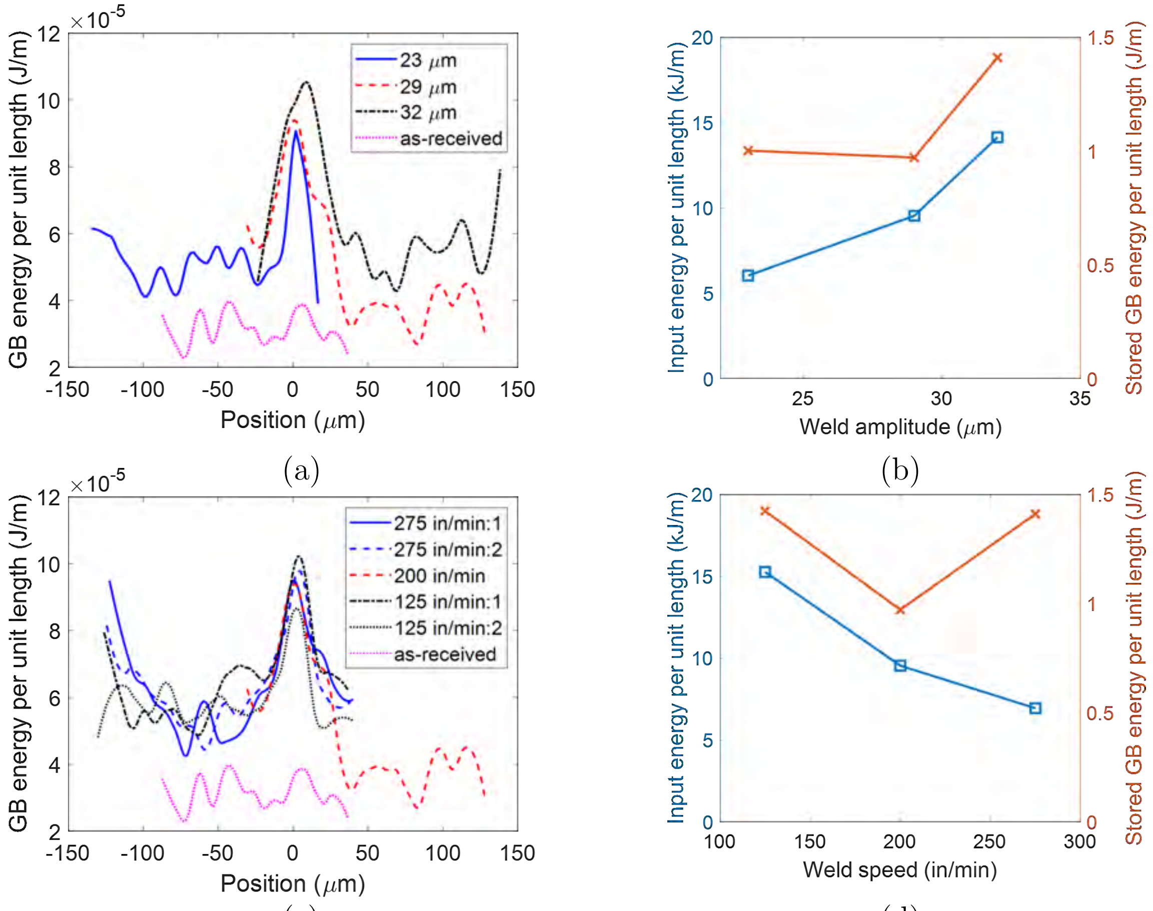

(a) (b)

(c) (d)

Figure 4.14: Trends in the stored energy in the microstructure with the weld parameters used for fabrication in UAM: (a) stored energy map for the control vs. samples prepared using 23, 29, and 32-μm weld amplitude; (b) total stored energy in the microstructure per unit length compared against the input electrical energy per unit length of weld as a function of weld amplitude; (c) stored energy map for the control vs. samples prepared using 125, 200, and 275 in/min weld speed; (d) total stored energy in the microstructure per unit length compared against the input electrical energy per unit length of weld as a function of weld speed.

The stored energy profile of the four sample sets analyzed − control vs. samples prepared using 23, 29, and 32-µm weld amplitude are compared in Figure 4.14(a). The cumulative stored energy is shown in Figure 4.14(b). The stored GB energy (approximately 1 J/m) is about 0.1% of the input electrical energy, or the energy budget (approximately 10000 J/m). There is a clear increase in interface width with increase in weld amplitude, and much higher energy is stored for the 32 µm case. This is believed to be due to the increase in the recrystallized region from a narrow region at the weld interface to a much wider region after a threshold weld amplitude is reached. Since 32 µm corresponds to the optimum weld amplitude found to give the highest interface shear strengths, there seems to be a correspondence between the growth in the interface width and the increase in weld strength.

The stored energy profile of the other set of four samples analyzed - control vs. samples prepared using 125, 200, and 275 in/min weld speed are compared in Figure 4.14(c). No clear trend in the total stored energy can be seen with weld speed, indicating that the weld amplitude of 29 µm is sufficiently higher than the threshold parameters required, such that there is no increase in the volume of recrystallized grains or the extent of grains refinement in the weld interface.

4.4 Conclusions

EBSD was used a tool for quantitative comparison of post-UAM microstructures. First, the effect of subsequent weld layers on weld microstructure was investigated by welding up to 9-subsequent layers of foil over a Al 6061-H18 foil-foil weld built using the following settings: 32 µm weld amplitude, 5000 N weld force, and 84.67 mm/s (200 in/min) weld speed. A technique was developed to determine the location and width of the interface region. The interface width was estimated to be about 14 μm for the 2-, 3-, 5-, and 10-layer samples, which is within previous literature estimates of the weld interface region. Nanoindentation was also introduced as a companion testing method to obtain the location and size of the weld interface region as a region of higher hardness compared to the bulk microstructure. The interface width from nanoindentation matches with the estimate from EBSD.

The following metrics were developed to quantify differences in weld interface microstructure – interface width, average grain size and percentage of grain boundaries that are High Angle Boundaries (% HAGB). The mean grain diameter was found to be around 0.7 μm, and 65% fraction of high angle grain boundaries in the weld interface region. Within the margin of error of EBSD due to its resolution limit, there is no significant effect of subsequent welds on the UAM weld interface microstructure for the sample heights and dimensions investigated with the metrics used.

Second, a study was developed to quantify the effect of UAM process parameters on the weld interface microstructure by measuring the energy stored in the microstructure. The Read-Shockley relationship was used to computed the stored energy in the grain boundaries obtained using the MTEX toolbox from the EBSD scans. A peak in the density and magnitude of stored energy greater than 10% of the mean energy was observed at the weld interface, which was absent in the control as-received foil sample. The stored energy was found to be approximately 0.1% of the input energy at 1 J/m for the UAM samples. Stored energy and interface width was observed to monotonously increase with weld amplitude at a fixed weld speed of 84.67 mm/s (200 in/min), but found not to be sensitive to weld speed at a fixed weld amplitude of 29 μm.

Chapter 5

Influence of Surface Roughness in UAM

Overview

This chapter entails a study to examine the effects of pre-weld foil surface roughness on weld energy and weld quality, characterized the shear strength of the weld interface measured using an in-plane shear testing fixture. Pretexturing using the welder and sandblasting with different particles will be used to prepare controlled surfaces on the top surface of the first welded foil before welding the next foil.

5.1 Introduction

The input energy from the welder in the UAM process is influenced by the coupling between the welder and workpiece surface. Previous work on the UAM of Al 6061-H18 [74] compared welders with 7 and 14 µm surface roughness (R_a) values, and discovered that the welder with 14 µm R_a produced welds with higher peak strength when tested using a push-pin test. The work, however, did not find a statistically significant strength improvement by changing the surface roughness of the foil from 0.12 µm to 5.7 µm for every third layer from the fifth layer in a twenty-layer build.

There are many metal-metal joining processes such as adhesive bonding, resistance welding, and roll bonding where physical or chemical preparation of the surface is crucial to obtain a good bond quality [75]. The physical methods include wire brushing, while the chemical methods include the use of etchants like phosphoric acid on the surface before the joining process. UAM typically does not require special surface cleaning or treatments, but the effect of surface roughness on the strength of an individual foil-foil weld has not been studied in detail. Work in [76] shows that for the UAM of Al 3003 to copper, changing the roughness of the copper foil from 0.17 to 1.17 µm does not produce a statistically significant increase in mechanical strength measured using a push-pin test. The same study also found a small anecdotal increase in the energy required for push-pin failure for the samples prepared with higher roughness.

The surface roughness profile of a surface can be characterized using different metrics [77]. The most common statistical measures used are R_a and R_q. For a surface with profile $z(x)$, these metrics are given by

$$R_a = \frac{\int |z(x)| dx}{\int dx} \tag{5.1}$$

$$R_q = \sqrt{\frac{\int |z(x)|^2 dx}{\int dx}} \tag{5.2}$$

These expressions can be found in [78]. The surface of the welder is textured to increase the grip between the weld foil and the welder. The texture is produced using electric discharge machining (EDM) to create a roughened texture typically with an R_a value between 11 and 14 μm [79]. The surface texture of an EDM-ed surface can be optimized using process conditions [80].

It is therefore necessary to develop an understanding of the relationship between surface roughness and bond strength by varying the surface roughness profiles of the foil-foil interface. To this end, the welder was rolled on machined foils at different vibration amplitudes, in a process called pretexturing. In this process, the UAM welder is rolled on top of a machined surface of previously deposited foil at a prescribed vibration amplitude, which imparts a roughness profile with R_a values correlated to the pretexturing amplitude on Al 6061-H18 foil. Other techniques such as sandblasting with alumina or steel pellets were also attempted to modify the surface texture. Sandblasting parameters such particle size and velocity can be used to control the resulting surface texture [81, 82]. A machined surface using a 63.5 mm (2.5 inch) diameter fly cutter using a spindle speed of 3000 RPM and feed speed of 12.7 mm/s (30 in/min) was used as the control case. Mechanical testing of the weld interface of interest between the first and second foil on the baseplate is conducted using a custom designed shear test fixture was used to discern the effect of the changing pre-weld surface texture on the resulting weld strength. The electrical power drawn by the transducers during welding is also measured during the welding of foils with different surface textures to detect any difference in input energy for the different cases.

5.2 Surface roughness measurements using optical profilometry

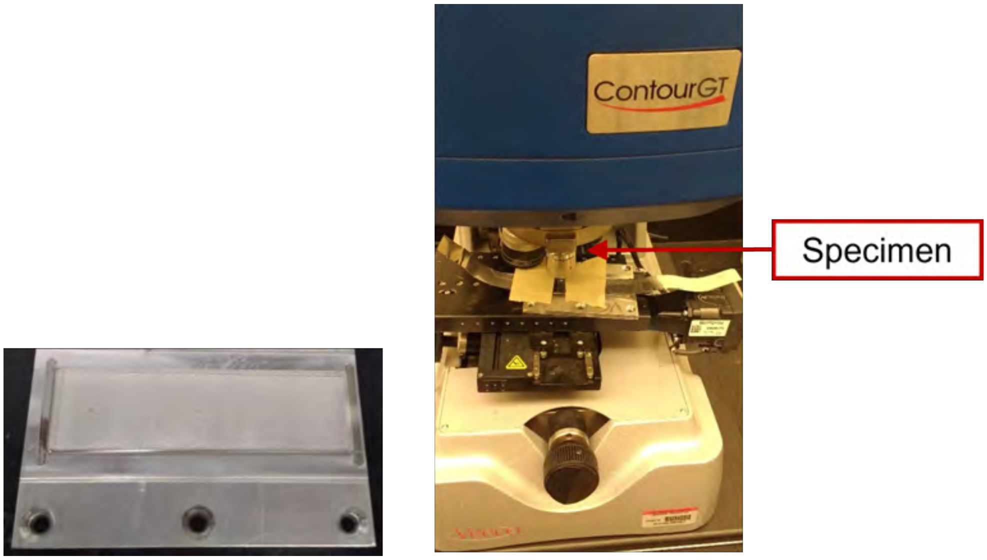

(a) (b)

Figure 5.1: Optical profilometry setup: (a) Specimen with 2-layers of Al 6061-H18 foil welded onto a Al 6061-T6 baseplate; (b) Bruker Contour GT-K optical profilometer used for non-contact roughness measurement.

The profile of a surface can be measured using contact and non-contact methods. The R_a value for sandblasted samples in Figure 5.4 was measured using a Mitutoyo SJ210 roughness tester. The tester measures a one-dimensional surface profile and computes the statistical measures of roughness such as R_a and R_q. Green light interferometry, a non-contact method was used to measure the texture of as-welded UAM surfaces to avoid modifying the surface, shown in Figure 5.1. This method also provides 3-dimensional profile data which can be used for more detailed analysis of roughness along different axes. This data is presented in Figure 5.2, where the as-received foil is found to have a very low R_a value of 0.11 μm and the as-welded foil has an R_a value of 9.66 μm.

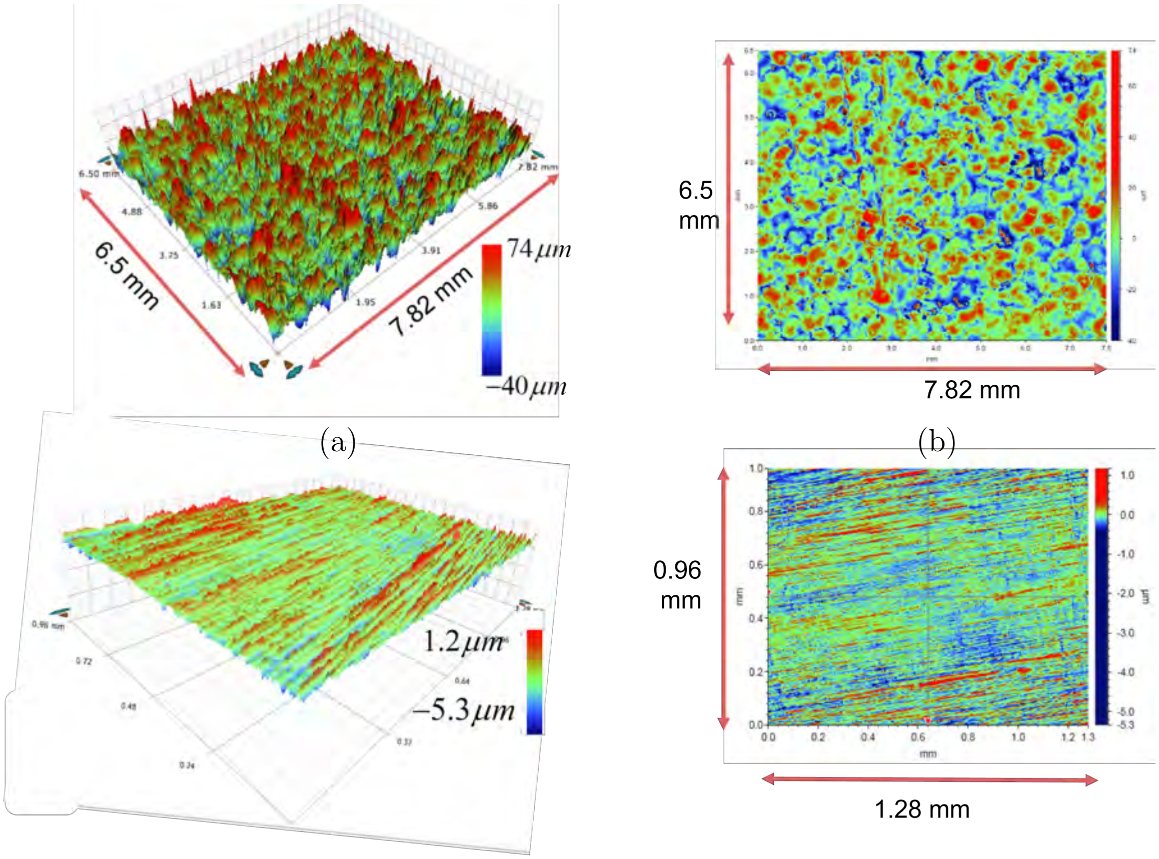

(a) (b)

(c) (d)

Figure 5.2: Bruker Contour GT-K optical profilometer used for non-contact roughness measurement: (a) 3-D surface profile of an as-welded UAM foil prepared using the following weld parameters: 28 μm weld amplitude, 5000 N weld force, and 84.67 mm/s (200 in/min) weld speed. with 2-layers of Al 6061-H18 foil welded onto a Al 6061-T6 baseplate with $R_a = 9.66$ μm; (b) The 2-D projection of (a); (c) 3-D surface profile of an as-received foil of Al 6061-H18 with $R_a = 0.11$ μm; (d) the 2-D projection of (c).

5.3 Roughness transfer experiments

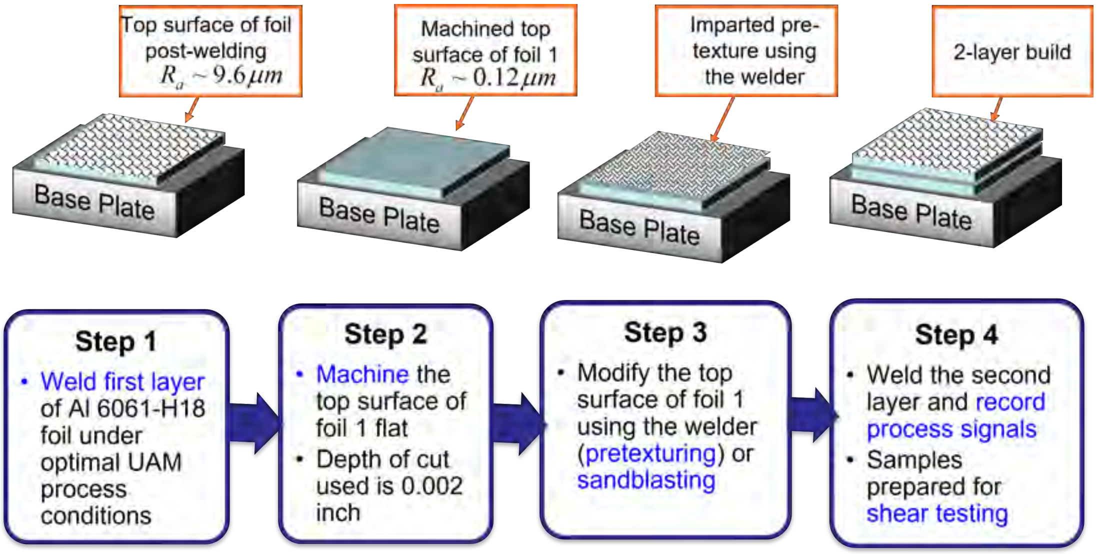
Top surface of foil post-welding $R_a \sim 9.6\mu m$
Machined top surface of foil 1 $R_a \sim 0.12\mu m$
Imparted pre-texture using the welder
2-layer build
Base Plate
Base Plate
Base Plate
Base Plate

Step 1
- Weld first layer of Al 6061-H18 foil under optimal UAM process conditions

Step 2
- Machine the top surface of foil 1 flat
- Depth of cut used is 0.002 inch

Step 3
- Modify the top surface of foil 1 using the welder (pretexturing) or sandblasting

Step 4
- Weld the second layer and record process signals
- Samples prepared for shear testing

Figure 5.3: Flowchart to produce different surface textures on the first welded foil before welding foil 2. Optimal process conditions used for Al 6061-H18 are 32 µm weld amplitude, 5000 N weld force, and 84.67 mm/s (200 in/min) weld speed.

The pretexturing process can both work harden the material near the surface by cold working and change the surface roughness. To avoid confounding the effect of these two factors on bond strength, the H18 temper of the Al 6061 material was chosen. The H18 temper is fully work hardened and cannot be strengthened by further cold working. In this study, all the foils to build the sample for mechanical testing are prepared using identical weld parameters. The weld force was set at 5000 N; weld speed at 84.67 mm/s (200 in/min); and the weld amplitude at 32 µm based on previous work with UAM of aluminum. Only the top surface of foil 1 was modified by machining it flat, and then pretexturing at the prescribed amplitude before welding. The pretexturing amplitude was increased from 10 to 30 µm with a step of 5 µm.

The top surface of the first welded foil is machined flat first to remove the effect of previous welding. A range of pretexture amplitudes are then used to create different surface profiles, with R_a shown in Figure 5.5. This process is shown in Figure 5.3. The R_a values for the resulting surface obtained range from 3.5 to 7.5 µm vs. a control of 0.1 µm by varying the pretexture amplitude at a fixed traversal speed of 84.67 mm/s (200 in/min). The surface texture welder used has an R_a value of 11 µm.

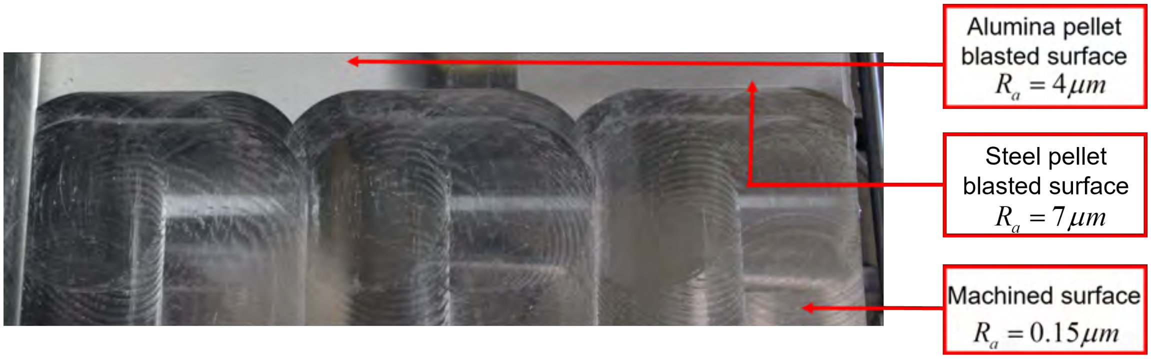
Alumina pellet blasted surface
$R_a = 4\mu m$
Steel pellet blasted surface
$R_a = 7\mu m$
Machined surface
$R_a = 0.15\mu m$

Figure 5.4: The surface of a machined Al 6061-T6 baseplate was modified using sandblasting using steel and alumina pellets to obtain surface textures with R_a values of 7 and 4 µm, respectively.

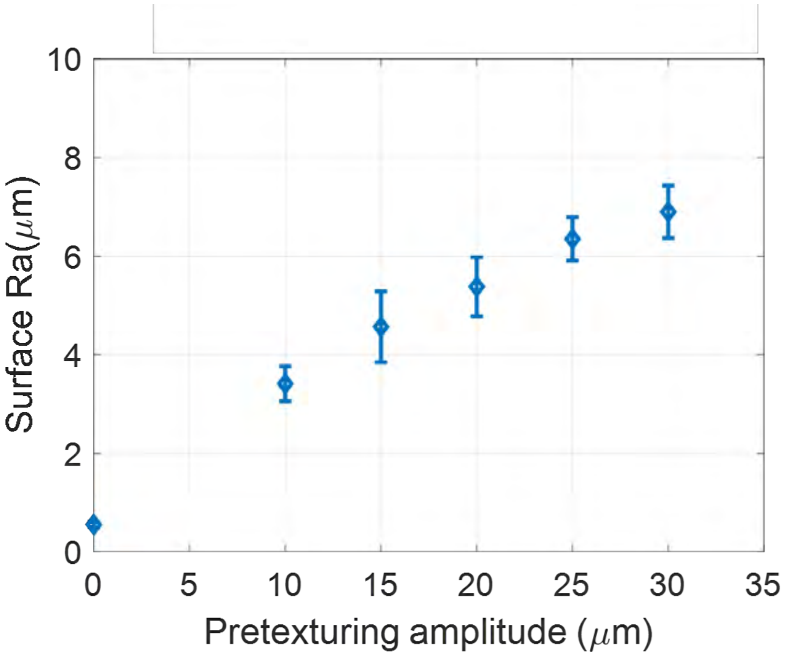

Figure 5.5: The R_a value of the surface texture produced using different pretexturing amplitudes at a fixed traversal speed of 84.67 mm/s (200 in/min).

5.4 In-plane shear strength measurements

UAM samples have a thin laminated construction with subsequent layers usually welded on previous ones, and this provides a challenge for mechanical characterization. In previous work, characterization has been limited to push pin testing [15] and peel testing [83], which provided a means for comparing interfacial strength of builds. These tests were not benchmarked against bulk properties. A fixture to characterize the absolute shear strength of a specific weld interface in a UAM build used in is shown in Figure 5.6. This method will be used in this study to measure bond strength of a UAM weld.

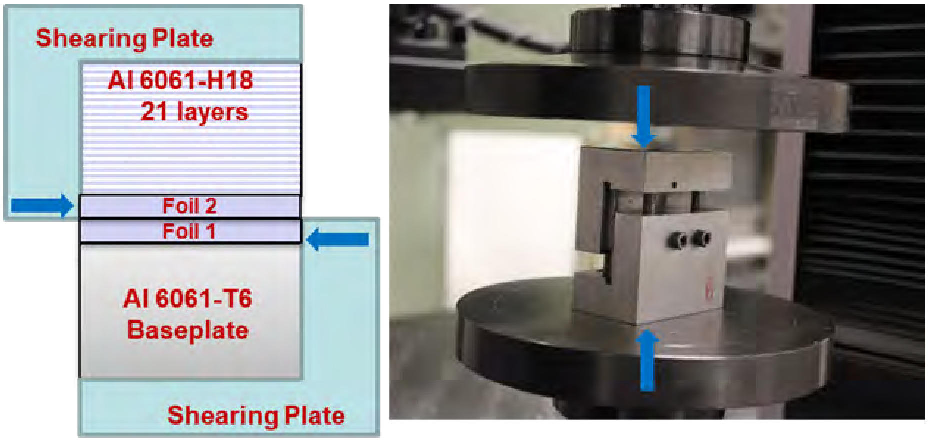

Figure 5.6: The shear testing rig used with compression platens in an MTS load frame used to test the foil−foil weld strength in shear.

A full-size shear sample was constructed by welding 23 layers of Al 6061-H18 foil. The samples were built to size as shown in Figure 5.8(a). The weld power was measured in-situ, shown in Figure 5.7, and was observed to not vary significantly with the changing surface texture for the different pretexture amplitudes used to texture the foil-foil interface before welding. This indicates that the energy input to the system is not dependent on the pre-weld surface preparation. Hence, the pre-weld surface preparation does not significantly change the friction coefficient of the foil−foil interface during welding. This is expected to be because the normal pressure collapses the asperities before the ultrasonic vibrations are applied.

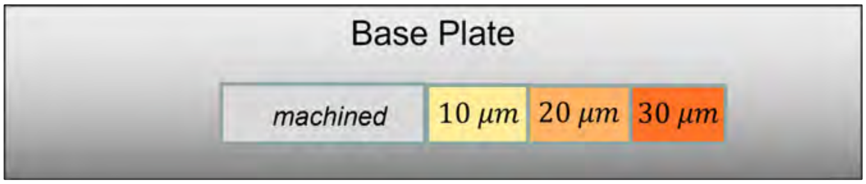

(a)

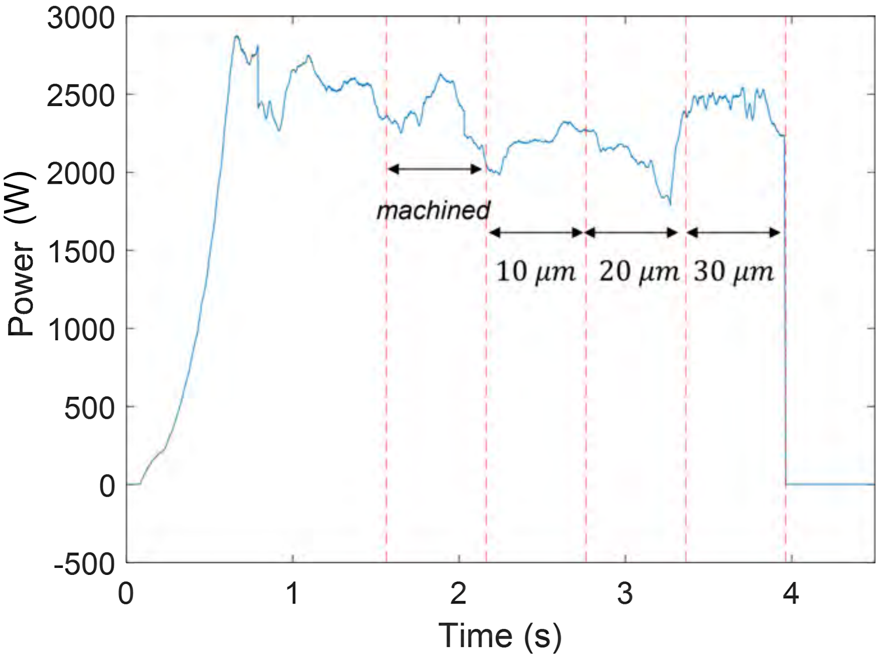

(b)

Figure 5.7: In-situ process power measurements for the welding of a second Al 6061-H18 foil onto Al 6061-H18 foil with different surface preparations: (a) The surface of the first foil is machined per Figure 5.3 and pretextured using different amplitudes; (b) weld power drawn by the transducers is monitored for the welding over the different sections, and was found to be invariant with pretexturing amplitude.

Samples for mechanical testing were cut out as shown in Figure 5.8(b). The geometry of the samples was designed so that the samples would fail by shearing at the foil 1 – foil 2 interface as seen in Figure 5.6. The strength of the weld between the first and second welded foil was tested in shear for samples prepared using different pretexturing amplitudes.

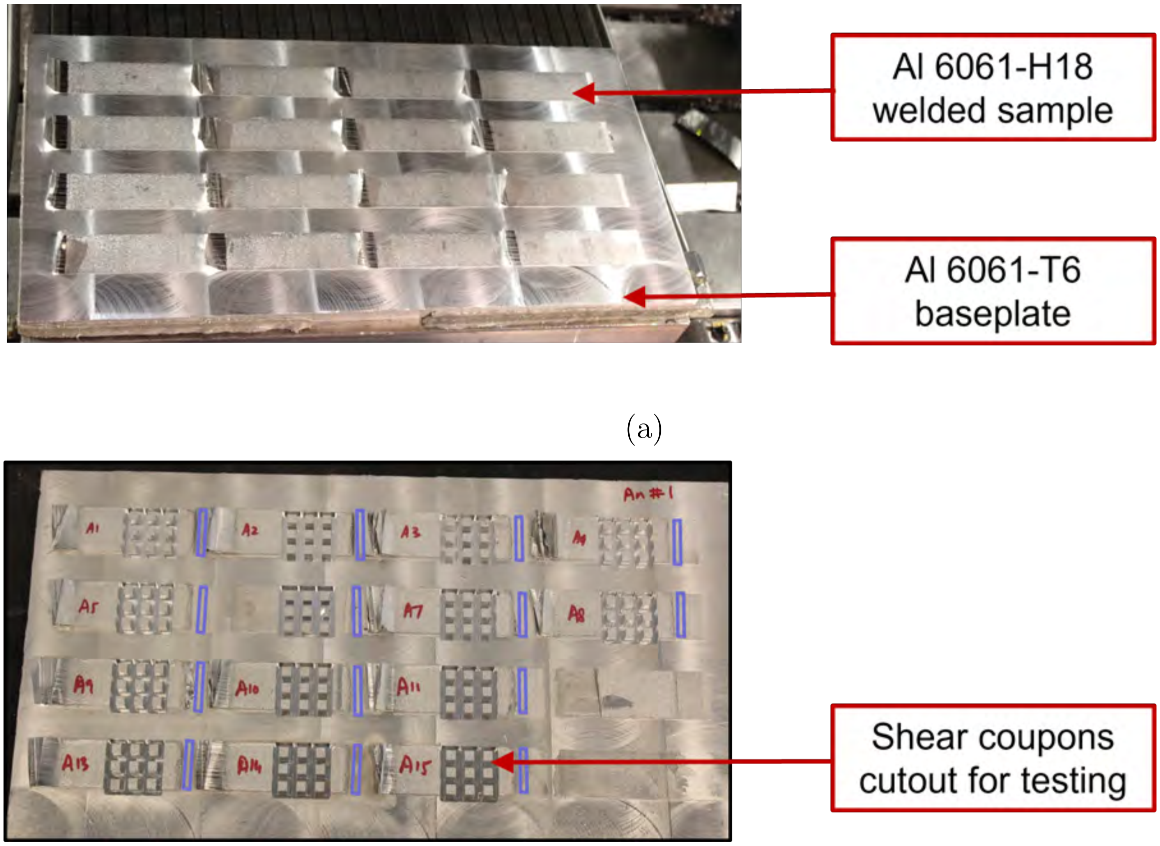
Al 6061-H18 welded sample
Al 6061-T6 baseplate
An #1
A1
A2
A3
A4
A5
A7
A8
A9
A10
A11
A13
A14
A15
Shear coupons cutout for testing

(a)

(b)

Figure 5.8: Samples prepared with different pre-weld surface textures using pretexturing: (a) Image of 23-layers of Al 6061-H18 welds welded onto the Al 6061-T6 baseplate by varying the welder vibration amplitude set point using a fixed 5000 N normal force and 84.67 mm/s (200 in/min) weld speed; (b) Mechanical testing coupons prepared at different surface preparation conditions for foil-foil welding between the first and second layer.

All samples built on the sandblasted surfaces in Figure 5.4 failed to form strong welds, and had inadequate strength to build a full-sized 23-layer sample. Hence the shear testing was conducted only for the samples which used the pretextured and the control surfaces. The shear area during testing is a square cross-section with side 0.195 mm. Representative load-displacement curves from the test are shown in Figure 5.9(a), and the shear stress at failure in Figure 5.9(b). The shear stress was obtained by dividing the peak load by the shearing area of the sample. Note that the zero values of displacement do not align due to small differences in sample dimensions which led to different strokes before engaging, but this does not affect the peak load reading. An optical section was taken of the samples post-failure to ensure that the expected foil 1 − foil 2 interface had failed.

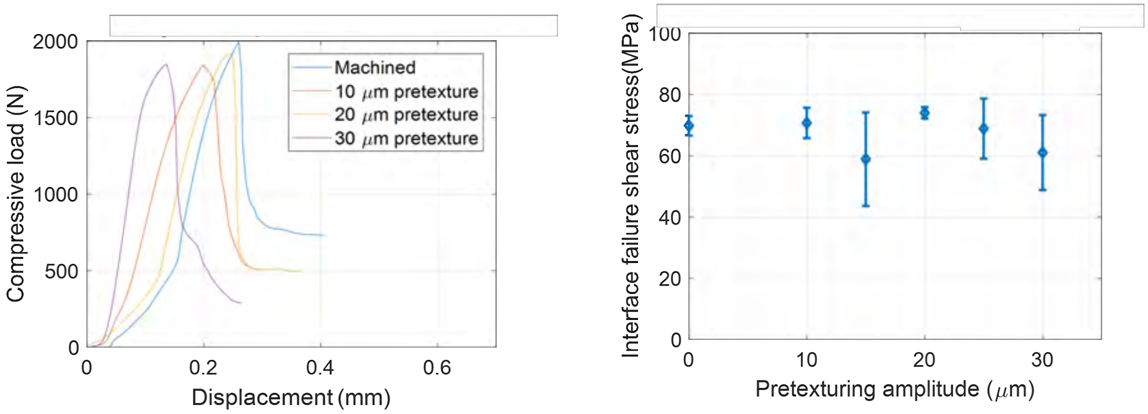

(a)

(b)

Figure 5.9: Shear testing results: (a) Individual stress versus displacement curves of full-size samples prepared using different surface textures between foil 1 and foil 2 before welding; (b) failure stress in shear as a function of the pretexturing amplitude which shows no significant effect of pretexturing on the resulting weld strength. Error bars are added to indicate 95% confidence intervals from multiple replicate shear samples. Some replicates were damaged during the fabrication of the shear sample.

5.5 Conclusions

The strength of foil−foil interface between the first and second Al 6061-H18 foil was measured to be between 60 and 70 MPa. Changing the surface texture of pre-weld Al 6061-H18 foil using pretexturing causes no measurable change in the shear strength of the weld interface for the range of parameters tested. The R_a value of the surfaces was varied between 3.5 and 7.5 µm and a control machined surface with an R_a value of 0.1 µm was used for comparison. Surface preparation using pretexturing hence is not a viable method to improve bond quality in UAM for Al 6061-H18 in the range of parameters tested. Changing the pre-weld surface roughness is also not found to affect the input energy into the weld for Al 6061-H18 within the range of parameters tested. It is thus proposed that the asperities are completely collapsed due to the normal pressure before cyclic deformations from the welder.

Chapter 6

Energy-based Process Model for UAM with Temperature-dependent Plasticity

Overview

This chapter details the development of an energy-strength correlation to map process parameters to the mechanical strength of UAM welds by identifying the driving energy (the energy of plastic deformation) for bond formation for Al-Al joining from the participating energies in UAM. To this end, a transient thermal finite element (FE) model is built to investigate the temperature increase from heat generation in UAM. The heat energy generated is estimated from the energy of plastic deformation and the frictional dissipation energy as a function of process parameters. An empirical relationship between the energy of plastic deformation and the strength of the weld interface is developed. The flow of energy in the UAM of aluminum is mapped, and the different energies involved in the UAM process are quantified.

6.1 Introduction

Mapping the flow of energy in UAM is necessary to quantify the relationship between process parameters, weld temperature, and weld strength. To that end, a model needs to be developed to quantify the partition of the input energy into the energy of plastic deformation, which drives bond formation, and friction, which contributes to heat generation. Understanding the role of heat generation and weld temperature in the UAM process is critical to developing this energy flow model. A transient thermal finite element (FE) model is thus developed to predict the weld temperature as a function of heat energy generated.

A key feature of the UAM process is the low formation temperature, which enables joining of dissimilar metals without the formation of brittle intermetallic phases. The low temperature aspect of the process enables the joining of many different metal combinations [4]. Using thermocouples embedded at the weld interface, the work in [5] showed that the peak temperature reaches near 150°C for welding aluminum and copper alloys with a 9 kW welder. Intermetallics often form in fusion processes with dissimilar metals because elevated temperatures permit mixing and diffusion. In contrast, melting and subsequent solidification are absent in UAM, and diffusion is minimal. Higher temperatures have been reported to improve inter-diffusion and localized melting at the interface in the ultrasonic welding of aluminum and zinc [84].

Real-time monitoring of the ultrasonic welding process was developed in [85] by monitoring the weld temperature. A 2-D finite element thermal model for UAM was developed in [86], and it was reported that the heat generation due to friction is twice the heat generation due to plastic deformation for AA1100 aluminum alloy. However, it was reported in [87] that heat generation due to plastic deformation is much higher than that from friction. Simple analytical expressions were used to estimate the heat generation and the 3-D temperature fields, which were compared against weld temperature measurements taken using thermocouples, which are the conventional means to measure weld temperature. Thermocouple measurements have some inherent disadvantages when compared to non-contact methods. Thermocouples also only provide a single-point measurement. Adding a thermocouple to a workpiece in a channel modifies the heat capacity of the surrounding region, and the measured temperature could be different from the temperatures reached if the thermocouple were not placed. The thermocouple also needs to be very sensitive with a high frequency bandwidth to accurately measure the very high heating rates of over 3000°C/s reported [88, 89].

Non-contact infrared (IR) imaging has several improvements over the use of thermocouples for temperature monitoring in UAM. IR cameras have detectors that absorb a narrow band of infrared radiation in the electromagnetic spectrum and transform it into a 2-dimensional temperature field. The detector converts the infrared photons emitted by the surface of the welder with spectrum given by Planck's law and Stefan Boltzmann's law. The wavelength emitted is given by Wein's displacement law [90]. The main advantages of using IR cameras are their quick response time and high sensitivity. A high-resolution 2-dimensional grid of data points can be obtained which provides a more detailed thermal field data. IR imaging has been used to predict small welding defects with high resolving power in arc welding [91] and laser welding [92]. The estimated weld temperature can be used to estimate the heat generated in the UAM process in conjunction with a thermal finite element (FE) model.

6.2 Analytical model development

In this section, an analytical model is developed to express the plastic deformation and the frictional dissipation energy as a function of process parameters.

6.2.1 Modeling assumptions

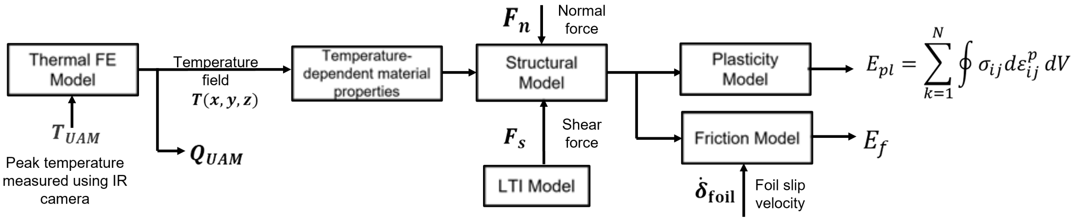

Thermal FE Model
Temperature field
$T(x,y,z)$
T_{UAM}
Peak temperature measured using IR camera
Q_{UAM}
Temperature-dependent material properties
F_n
Normal force
Structural Model
F_s
Shear force
LTI Model
Plasticity Model
$E_{pl} = \sum_{k=1}^{N} \oint \sigma_{ij} d\varepsilon_{ij}^{p} \, dV$
Friction Model
E_f
$\dot{\delta}_{\mathrm{foil}}$
Foil slip velocity

Figure 6.1: Schematic of the thermal-structural model to estimate the energy of plastic deformation E_{pl} and the energy dissipated due to friction E_f.

Developing a comprehensive coupled thermal-mechanical model for UAM requires the simulation of several thousand cycles of high-frequency 20 kHz vibrations, which is computationally very expensive. Hence, an analytical framework is developed to approximate the stress, strain, and temperature fields in the UAM process. The thermal and structural problems are decoupled, and the weld temperature from the thermal FE model is used as input in the structural problem to determine the temperature-dependent yield strength, seen in Figure 6.1. The heat energy generated is estimated from the structural model.

The following simplifying assumptions are made. First, it is assumed that the variation of the Z-direction normal stress from the welder-foil contact surface to the foil-foil contact surface is neglected since the thickness t of the foil (150 μm) is significantly lower than its width w (25.4 mm). Second, the elongation in the rolling direction (X-direction) due to rolling is neglected, and X-direction stresses and strains are neglected. This leads to the overestimation of the energy of plastic deformation in soft materials like Al 6061-O where some elongation is observed in the weld foil after UAM. Third, the elastic component of the total strain is considered to be small compared to the plastic strain due to the large plastic deformations imparted by the welder (10-20 μm) and are neglected.

Fourth, the von-Mises criterion is used as the yield criterion for the initiation of plasticity. Previous work in [93] on the mechanical behavior of 2024 aluminum alloys found that there was no strain-rate dependence on plastic deformation up to strain rates of 5000 s^{-1}, which is close to the typical strain rate in UAM calculated from the maximum shear strain $\gamma = |\delta_{welder}|/t$ and the welder frequency of 20 kHz. Hence strain-rate dependence is not modeled, but this assumption can be modified for the UAM of different materials. The anisotropy in the material yield parameters is also ignored for simplicity, but the rolled foil is expected to have some anisotropy between the rolled and transverse directions. Fifth, no slip is assumed between the welder and the weld foil since the roughened welder surface will produce sufficient grip to prevent slipping.

6.2.2 Model for plastic deformation energy

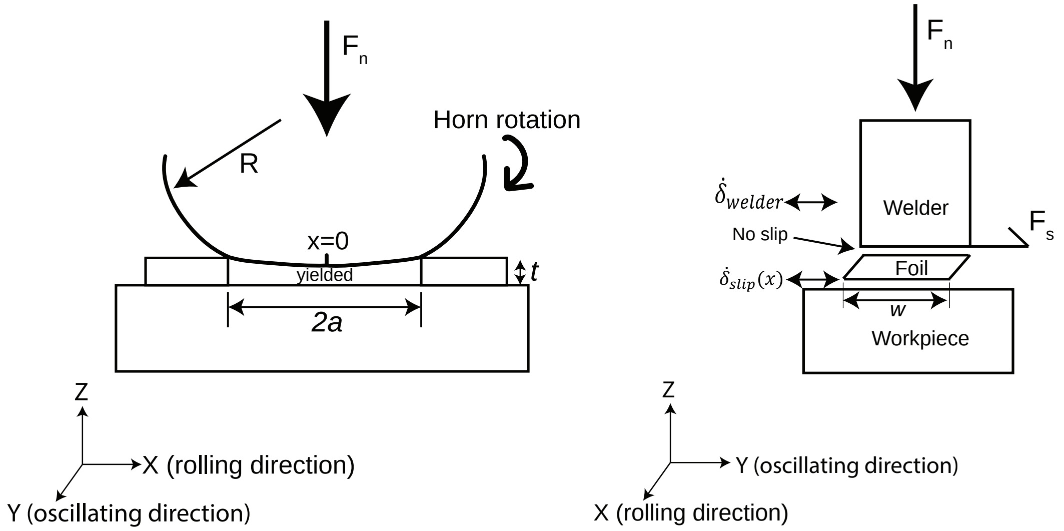
F_n
Horn rotation
R
x=0
yielded
t
2a
Z
X (rolling direction)
Y (oscillating direction)
F_n
Welder
$\dot{\delta}_{welder}$
No slip
F_s
Foil
$\dot{\delta}_{slip}(x)$
w
Workpiece
Z
Y (oscillating direction)
X (rolling direction)

(a) (b)

Figure 6.2: Illustration of the forces and vibration velocities during UAM: (a) the contact width $2a$ of the weld foil of thickness t with the yielded foil material under the welder; (b) the top of the foil of width w sticks to the welder and the bottom of the foil has a slip velocity profile $\dot{\delta}_{slip}(x)$ with the workpiece (previously welded foil or baseplate). The vibration velocity of the workpiece is assumed to be small in comparison to the welder's vibration velocity.

Normal and shear stresses

If Hertzian contact were assumed, the normal stress $\sigma_{zz}^{Hz}(x)$ under the welder, the maximum normal stress P_{max}^{Hz}, and the contact half-width a^{Hz} would be given by

$$\sigma_{zz}^{Hz} = P_{max}^{Hz}\sqrt{1-\left(\frac{x}{a^{Hz}}\right)^2} \tag{6.1}$$

$$P_{max}^{Hz} = \sqrt{\frac{W_d E^*}{\pi R}},\ E^* = \frac{1-\gamma_{St}^2}{E_{St}} + \frac{1-\gamma_{Al}^2}{E_{Al}} \tag{6.2}$$

$$a^{Hz} = 2\sqrt{\frac{W_d R}{\pi E^*}}, \tag{6.3}$$

where E^* is the effective modulus of the steel-aluminum interface calculated from the modulus, $W_d = F_n/w$ is the normal load F_n per unit width w, and R is the radius of the steel welder [41]. Note that $x = 0$ is directly under the axis of rotation of the welder.

For a steel welder on aluminum foil, the maximum stress for a 5000 N normal force would be 276 MPa, which is higher than the yield strength of even work-hardened foil materials such as Al 5052-H38 (yield strength = 255 MPa) and Al 6061-H18 (yield strength = 230 MPa). Thus, the key Hertzian assumption of elastic behavior is invalid, and the stress distributions obtained cannot be directly used. The model is extended to include effect of the material yielding by proposing that after yielding, the contact half-width continues to increase to distribute the normal load over a larger load-bearing area until the forces are balanced. Note that the product $P_{max}^{Hz}.a^{Hz}$ is a constant that is only dependent on the normal load per unit length W_d. It is assumed that the normal load distribution in the plastic regime has a similar distribution as (6.1) with a new maximum normal stress P_{max} and contact half-width a, as shown in Figure 6.2(a).

The normal stress distribution under the welder in the plastic regime is given by

$$\begin{aligned} \sigma_{zz} &= P_{max}\sqrt{1-\left(\frac{x}{a}\right)^2}, && (6.4)\\ P_{max}a &= 2W_d/\pi. && (6.5) \end{aligned}$$

The term $\sigma(x)$ will henceforth be used in place of $\sigma_{zz}(x)$ for brevity.

The shear force F_s applied by the welder results in a shear stress distribution $\tau(x)$ in the YZ-plane such that

$$\int_{-a}^{a} \tau(x) w dx = F_s. \tag{6.6}$$

Yield criterion

The state of stress of a stress element taken at a location x with breadth dx can be represented using the Cauchy stress tensor σ_{ij} to be

$$\sigma_{ij} = \begin{bmatrix} 0 & 0 & 0 \\ 0 & 0 & \tau(x) \\ 0 & \tau(x) & -\sigma(x) \end{bmatrix}. \tag{6.7}$$

The deviatoric stress is calculated as the difference of the stress tensor and one-third of its trace to be

$$s_{ij} = \begin{bmatrix} \frac{\sigma(x)}{3} & 0 & 0 \\ 0 & \frac{\sigma(x)}{3} & \tau(x) \\ 0 & \tau(x) & -2\frac{\sigma(x)}{3} \end{bmatrix}. \tag{6.8}$$

J-2 flow theory is used to describe the yield behavior of the material, and the von-Mises criterion is used for the yield criterion. Since the material in the region $-a < x < a$ is assumed to be yielded, The von-Mises criterion states that

$$J_2 = \frac{1}{2} s_{ij} s_{ij} = \sigma(x)^2/3 + \tau(x)^2 = \sigma_y^2/3, \tag{6.9}$$

where $\sigma_y = \sigma_y(T_{weld})$ is the temperature-dependent yield strength of the foil material at the weld temperature T_{weld}. The expression in (6.9) can be used to obtain the shear stress distribution from a given normal stress distribution as follows:

$$\tau(x) = \frac{1}{3}\sqrt{\sigma_y^2 - P_{max}^2\left(1 - (\frac{x}{a})^2\right)} \tag{6.10}$$

Substituting (6.10) in (6.6) and using $\alpha = \frac{x}{a}$ gives

$$\begin{aligned} F_s &= \int_{-a}^{a} \frac{1}{3}\sqrt{\sigma_y^2 - P_{max}^2\left(1 - (\frac{x}{a})^2\right)}.w.dx & (6.11)\\ &= \int_{\alpha=-1}^{\alpha=1} \frac{a.w}{3}\sqrt{\sigma_y^2 - P_{max}^2(1-\alpha^2)}.d\alpha, & (6.12)\\ &= \frac{a.w.P_{max}}{3}\int_{-1}^{1}\sqrt{\left(\frac{\sigma_y^2}{P_{max}}^2 - 1\right) + \alpha^2)}.d\alpha. & (6.13)\end{aligned}$$

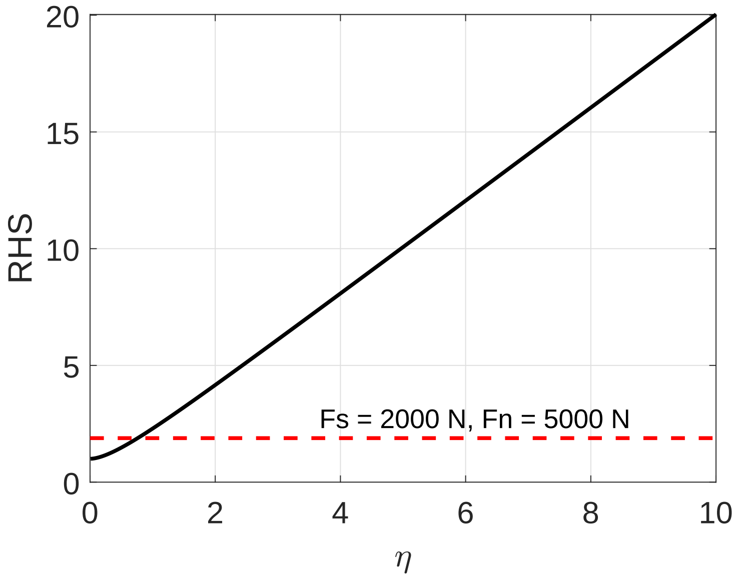

ol

Figure 6.3: The expression in (6.16) is plotted as a function of the variable η. The minimum value for the expression is 1 when $\eta = 0$. The dotted red line denotes the value of the expression at a weld force $F_n = 5000$ N and shear force $F_s = 2000$ N.

Using (6.5) and the substitution $\frac{\sigma}{P_{max}} = 1 + \eta^2$ for $\eta > 0$,

$$F_s = \frac{2.W_d.w}{3\pi} \int_1^1 \sqrt{\eta^2 + \alpha^2}.d\alpha, \tag{6.14}$$

$$\frac{3\pi F_s}{2F_n} = \Big|_{\alpha=-1}^{\alpha=1} \frac{1}{2}\alpha\sqrt{\alpha^2 + \eta^2} + \frac{\eta^2}{2}\ln \alpha + \sqrt{\alpha^2 + \eta^2} \tag{6.15}$$

$$\underbrace{\frac{3\pi F_s}{2F_n}}_{LHS} = \underbrace{\sqrt{1 + \eta^2} + \frac{\eta^2}{2}\ln \frac{\sqrt{1 + \eta^2} + 1}{\sqrt{1 + \eta^2} - 1}}_{RHS} \tag{6.16}$$

Expression (6.16) provides a direct way to calculate the maximum normal pressure P_{max} for a given shear and normal force. The expression in (6.16) is plotted as a function of η in Figure 6.3. From expression (6.16), it is clear that the RHS is always greater than 1, which gives a minimum shear force for a given weld force as

$$F_{s,min} = \frac{2}{3\pi}F_n = 0.21.F_n. \tag{6.17}$$

For shear forces below this minimum value, the complete contact region is not plastically yielded.

Example case

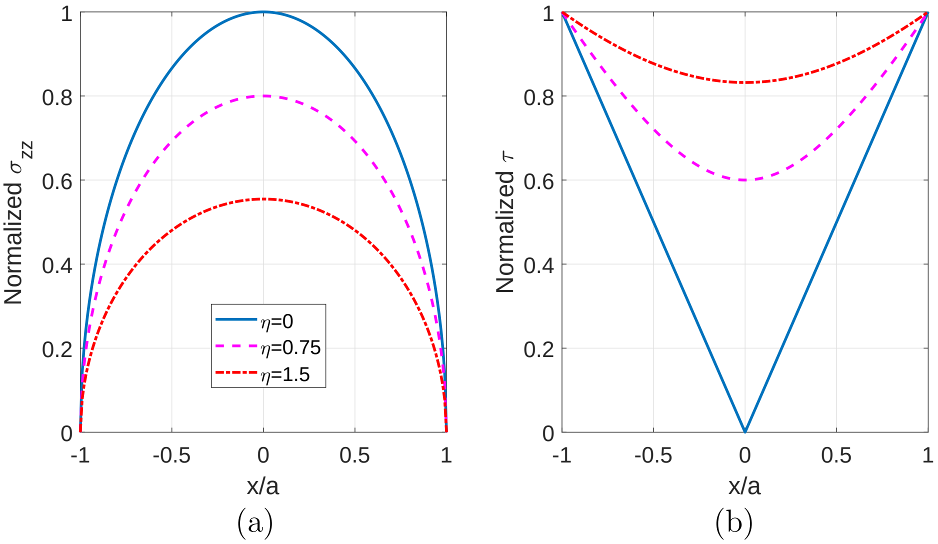

(a) (b)

Figure 6.4: The normal and shear stresses along the contact width are plotted vs. the X-position normalized with the contact width a: (a) normalized normal stress $= \frac{\sigma(x)}{\sigma_y}$ from (6.5) and (b) normalized shear stress $= \frac{\tau(x)}{\sigma_y/3}$ from (6.10) for three different values of $\eta = 0$, 0.75, and 1.5. The value of $\eta = 0$ corresponds to the shear force $F_s = F_{s,min}$ from (6.17).

For the typical weld parameters used to weld Al 6061-H18 onto a Al 6061-T6 baseplate, the weld force applied in the Z-direction is 5000 N. This corresponds to $F_{s,min} = 1061$ N from (6.17). The shear force depends both on the weld amplitude and the compliance on the system. The applied shear force using optimized welding parameters for Al 6061-H18 is 2000 N [35], and substituting these force values in (6.16) gives an LHS value of 1.885. Solving (6.16) numerically using MATLAB, this corresponds to a η value of approximately 0.75. Note that this value is not material-dependent.

The maximum normal pressure P_{max}, contact half-width a, and shear stress distribution $\tau(x)$ for this case are this computed using (6.5) and (6.10) to be

$$\begin{align} P_{max} &= \frac{\sigma_y}{\sqrt{1+\eta^2}} = 0.8\sigma_y \tag{6.18} \\ a &= \frac{2W_d}{\pi\sigma_y}\sqrt{1+\eta^2} = \frac{5W_d}{2\pi\sigma_y} \tag{6.19} \\ \tau(x) &= \frac{2W_d}{\pi P_{max}}\sqrt{\frac{\sigma_y^2\eta^2}{1+\eta^2} + \frac{\sigma_y^2}{1+\eta^2}\big(\frac{x}{a}\big)^2} = \frac{\sigma_y}{3\sqrt{1+\eta^2}}\sqrt{\eta^2 + \big(\frac{x}{a}\big)^2} \tag{6.20} \\ &= \frac{\sigma_y}{3}\sqrt{0.36 + 0.64\big(\frac{x}{a}\big)^2} \tag{6.21} \end{align}$$

The value of $\tau(x)$ at the end of the contact patch equals one-third of the yield strength as expected since the normal pressures are zero. Note the maximum normal pressure is always proportional to the material yield strength and the contact half-width is inversely proportional to the material yield strength. The normal and shear stress profiles in the contact width region are plotted in Figure 6.4(a) and Figure 6.4(b) respectively for different values of η.

Plastic deformation energy estimation

The UAM welder imparts a sinusoidal motion to the top of the foil being welded. Starting at the mean position, the incremental displacement dy leads to an incremental shear plastic strain $d\gamma = d(y - y_{slip})/t$ where t is the thickness of the foil and dy_{slip} is the incremental frictional slip, as illustrated in Figure 6.2(b). It is not expected that asperity-level deformations result in significant differences in the energy of plastic deformation. From the studies in chapter 5, it was found that changing the height of asperities in the pre-weld surface by an order of magnitude (R_a value from 0.1 to

7.5 μm) does not change the input energy or the strength of the weld interface in shear. Asperity-level deformation can thus be neglected. Since the elastic component of the strains are also neglected, the incremental plastic strain tensor is given as

$$d\varepsilon_{ij} = \begin{bmatrix} 0 & 0 & 0 \\ 0 & 0 & d\gamma/2 \\ 0 & d\gamma/2 & 0 \end{bmatrix} \tag{6.22}$$

The incremental work done for plastic deformation of the weld foil dW_{pl} for an incremental welder displacement dy and incremental slip dy_{slip} between the foils is given by

$$\begin{aligned} dW_{pl} &= \int_{-a}^{a} \frac{1}{2} s_{ij}(x) d\varepsilon_{ij}(x).w.t.dx & (6.23) \\ &= \int_{-a}^{a} \tau(x) \frac{dy - dy_{slip}(x)}{t} wtdx = F_s dy - \int_{-a}^{a} \tau(x) dy_{slip}(x) wdx & (6.24) \end{aligned}$$

The rate of plastic work $\dot{W}_{pl}$ can be calculated as

$$\dot{W}_{pl}(t) = \frac{dW_{pl}}{dt} = F_s.\frac{dy}{dt} - \int_{-a}^{a} \tau(x) \frac{dy_{slip}(x)}{dt} dx = F_s \dot{\delta}_{welder} - \int_{-a}^{a} \tau(x) \dot{\delta}_{slip}(x) wdx \tag{6.25}$$

Assuming that the slip velocity and welder velocity are in phase, the rate of work averaged over one time-period T of oscillation can be computed as

$$\dot{W}_{pl}^{avg} = \frac{1}{2} F_s |\dot{\delta}_{welder}| - \frac{1}{2} F_s \int_{-a}^{a} \frac{\tau(x)}{F_s} |\dot{\delta}_{slip}(x)| wdx. \tag{6.26}$$

Note that the first term is the rate of total mechanical work done by the welder, defined in [94], and the second term is the portion lost due to slip. The energy of plastic deformation E_{pl} at a single location in the foil is given by the product of the average rate of work and the time spent by the welder over the location:

$$E_{pl} = \dot{W}_{pl}^{avg} \frac{2a}{|\dot{x}|} = \frac{a}{|\dot{x}|} F_s \left(|\dot{\delta}_{welder}| - \int_{-a}^{a} \frac{\tau(x)}{F_s} |\dot{\delta}_{slip}(x)| wdx \right), \tag{6.27}$$

where $|\dot{x}|$ is the weld speed. For the case of unsuccessful welds, when $|\dot{\delta}_{slip}(x)| = |\dot{\delta}_{welder}|$, the energy of plastic deformation $E_{pl} = 0$.

6.2.3 Model for frictional dissipation energy

The heat generation due to friction between foils per unit time is given by the following equation:

$$\dot{q}_f(t) = \int_{-a}^{a} \tau_f(x)\dot{\delta}_{slip}(x)wdx. \tag{6.28}$$

Here Q_f is the heat generation due to friction, a is the half-width of the contact region, $\dot{\delta}_{slip}(x)$ is the slip between the foils at a distance x away from the welder, $\tau_f(x)$ is the frictional stress at that position, and w is the width of the foil. Assuming Coulomb friction and averaging over one time-period of vibration, (6.28) simplifies to

$$\dot{q}_f^{avg} = \frac{1}{2}\int_{-a}^{a} \mu\sigma(x)|\dot{\delta}_{slip}|(x)wdx \tag{6.29}$$

where μ is the Al-Al friction coefficient and $|\dot{\delta}_{slip}|(x)$ is the magnitude of the slip velocity between the foils. The friction coefficient can be process parameter-dependent, as found in [95]. In the limiting case, it is assumed that there is pure slip between two foils being welded. This leads to all the deformation of the welder being transformed to frictional slip deformation between the weld foils. Then,

$$\dot{q}_f^{avg} = \frac{1}{2}\int_{-a}^{a} \mu\sigma(x)|\dot{\delta}_{welder}|wdx = \frac{1}{2}\mu F_N.|\dot{\delta}_{welder}|, \tag{6.30}$$

where $|\dot{\delta}_{welder}|$ is the magnitude of the welder's vibration velocity.

The frictional energy dissipation E_f at a single location in the foil is given by the product of the average rate of work and the time spent by the welder over the location:

$$E_f = \dot{q}_f^{avg}\frac{2a}{|\dot{x}|} = \frac{a}{|\dot{x}|}\int_{-a}^{a} \mu\sigma(x)|\dot{\delta}_{slip}|(x)wdx, \tag{6.31}$$

where $|\dot{x}|$ is the weld speed. In the case where there is no plastic deformation in the foil, the friction coefficient μ will take the value of F_s/F_n.

6.3 Thermal model

The total heat generation comes from losses in plastic deformation and frictional dissipation. The fraction of plastic energy that is converted to heat, the Taylor−Quinney coefficient, is β and a typical value of 0.9 for aluminum is chosen [5].

$$
\begin{aligned}
q_{total} &= \beta E_{pl} + E_f \qquad (6.32)\\
&= \frac{a}{|\dot{x}|}\left(\beta F_s|\dot{\delta}_{welder}| - \beta\int_{-a}^{a}\tau(x)|\dot{\delta}_{slip}(x)|w dx + \int_{-a}^{a}\mu\sigma(x)|\dot{\delta}_{slip}|(x) w dx\right)
\end{aligned}
$$

During the ultrasonic metal additive manufacturing (UAM) process, heat is generated from two sources, i.e. interfacial friction and plastic deformation. The transient temperature field can be estimated using the following equation:

$$\rho c\frac{\partial T}{\partial t} = k\left(\frac{\partial^2 T}{\partial x^2} + \frac{\partial^2 T}{\partial y^2} + \frac{\partial^2 T}{\partial z^2}\right) + q_{total} \qquad (6.33)$$

Here $\frac{\partial T}{\partial t}$ is the change in the temperature with respect to time, ρ is the material density, c is the material specific heat, q is the heat generation rate and k is the thermal conductivity. Boundary conditions for convection is shown in (6.34) and those for heat flux are shown in (6.35):

$$
\begin{aligned}
-k\frac{\partial T}{\partial n} &= h(T_a - T_i), \qquad (6.34)\\
k\frac{\partial T}{\partial n} &= q_b. \qquad (6.35)
\end{aligned}
$$

Here h is the material surface heat transfer coefficient, n is the normal direction, T_a is the air temperature and T_i is the boundary temperature and q_b is the boundary heat flux.

Table 6.1: Summary of thermal properties used for the transient thermal finite element (FE) analysis using COMSOL.

		Aluminum	AISI 4340	Copper
Specific Heat Capacity	(J/(kg.K))	900	55	475
Density	(kg/m^3)	2700	7850	8960
Thermal Conductivity	(W/(m.K))	201	44.5	386

6.3.1 Transient thermal finite element model

A transient thermal simulation of the rotating welder and the translating workpiece simulated using COMSOL. Properties of the materials used are listed in Table 6.1. The welder rotates such that there is no rolling slip with the workpiece. The weld foils and the baseplate are modeled as one piece since they are all made of aluminum alloys. A pairwise thermal contact is defined between the welder and the workpiece, with heat generation.

A rotating domain deforming geometry was used to rotate the welder at a constant angular velocity. A prescribed deformation deforming geometry was used to translate the workpiece at the weld speed. A pairwise thermal contact is defined between the steel welder and the aluminum workpiece. AISI 4340 was used for the steel material properties for the welder and Aluminum 6063-T83 was used for the workpiece material properties.

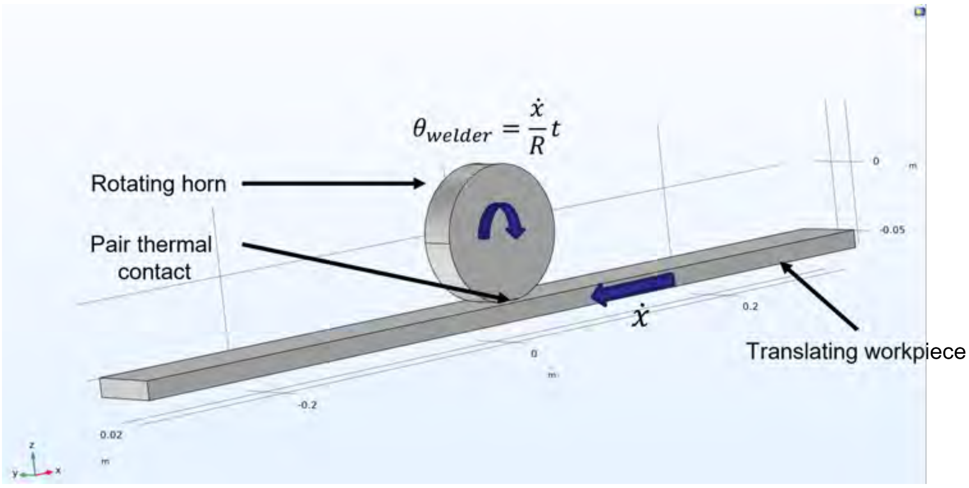

Figure 6.5: A transient thermal simulation of the rotating welder and the translating workpiece simulated using COMSOL. The welder rotates such that there is no rolling slip with the workpiece. The weld foils and the baseplate are modeled as one piece since they are all made of aluminum alloys. A pairwise thermal contact is defined between the welder and the workpiece, with heat generation at the interface.

The combined heat generated due to friction and plastic deformation (q_{total}) is partitioned at the contact interface in accordance with the Charron's relationship [96] where the generated heat is partitioned into rQ_{total} into the steel welder and $(1-r)q_{total}$ to the foils. The expression for r is given as

$$r = \frac{1}{1+\xi}, \quad \text{where } \xi = \sqrt{\frac{\rho_1 C_{p,1} k_1}{\rho_2 C_{p,2} k_2}}. \tag{6.36}$$

Here ρ_1, $C_{p,1}$, and k_1 are the density, specific heat capacity, and thermal conductivity of the weld foil, and similarly with subscript 2 for the steel welder. For welding aluminum, 16.5% of the heat generated is lost to heating the steel welder. It is assumed that the heat generated due to plastic deformation can be approximated to be at the horn−foil interface due to the small thickness of the feedstock.

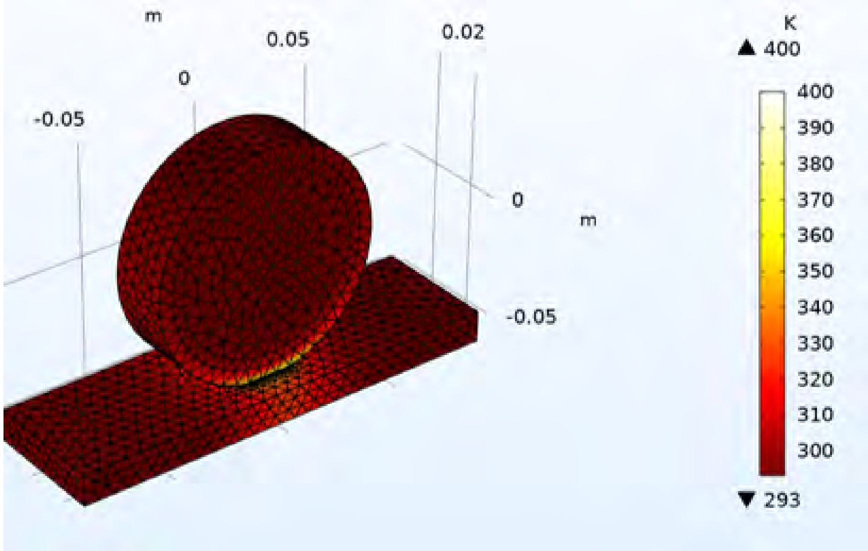

Figure 6.6: Temperature field in K under a rotating welder and a feedstock translating at a speed of 84.67 mm/s (200 in/min) simulated using COMSOL. Thermal power of 2000 W is input to the welder-workpiece interface which is partitioned based on Charron's rule (6.36). A temperature increase of 107 K from ambient was estimated.

The transient simulation is run with a sample heat generation of 2000 W at the welder−foil interface in Figure 6.6, which results in a predicted temperature increase of 107 K for a weld speed of 84.67 mm/s (200 in/min). Trial simulations showed that the peak temperature was not sensitive to the convection coefficient between the welder and air, and hence a typical surface-to-air value of 20 $W/m^2.K$ was used.

6.3.2 Parametric study using FE model - effect of weld speed

A simple analytical moving heat source model for heat generation UAM like the model used in [97] do not account for the rotation of the welder in the model. The welder rolls without slip on the foil during the UAM process. The effect of weld speed on weld temperature is estimated using the FE model by varying the weld speed between 125, 200, and 275 in/min and plotting the FE estimates of peak welder temperature in Figure 6.7(a). The results show that the peak temperature values reach a steady value after about 0.5 seconds and the steady peak temperature increases with decreasing weld speed. The actual temperature profile of the welder surface is shown in Figure 6.7 (b), (c), and (d) for 52.92 mm/s (125 in/min), 84.67 mm/s (200 in/min), and 116.4 mm/s (275 in/min) respectively. The profiles show a peak temperature at the welder contact point, and very high temperature gradients as a function of angle.

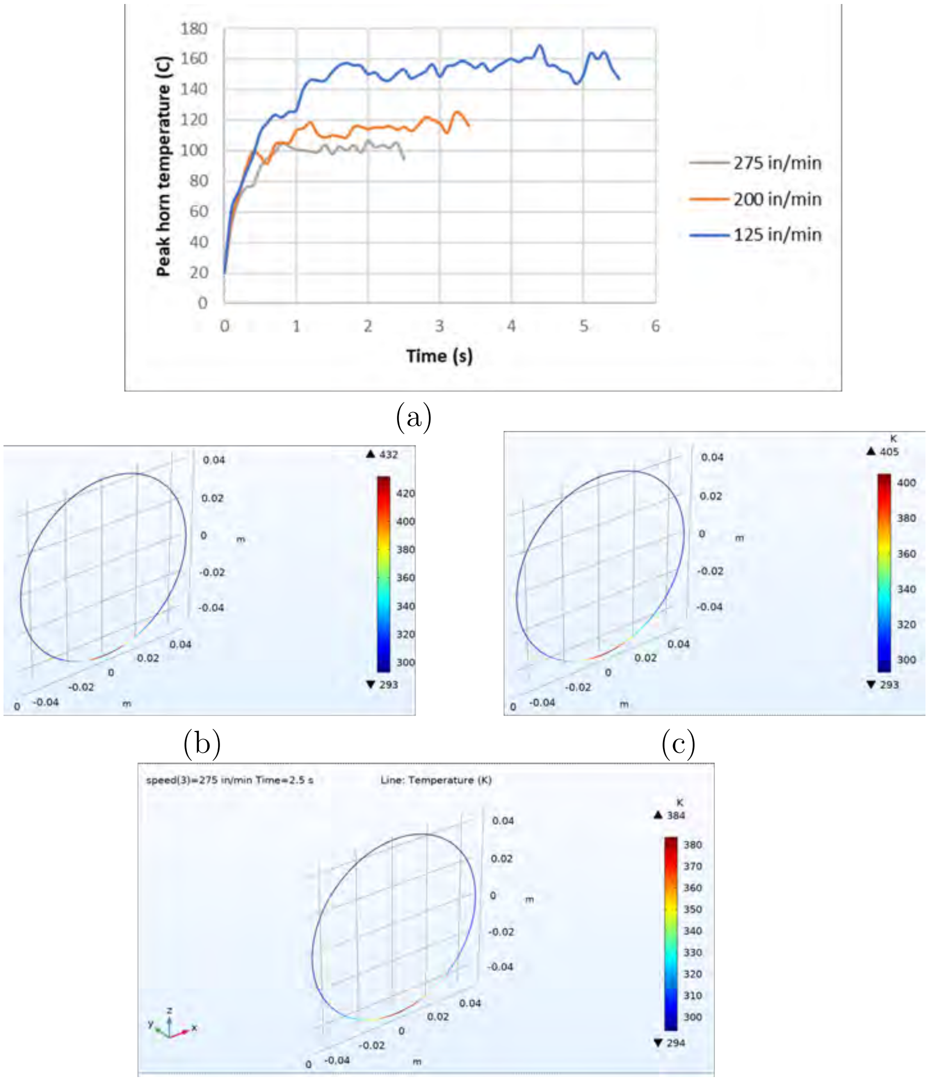

(a)

(b) (c)

(d)

Figure 6.7: Temperature field in K under a rotating welder with a translating feedstock simulated using COMSOL at different weld speeds, and the corresponding temperature profile on the welder for a 2000 W reference heat input at the welder-workpiece interface: (a) The temperature at the foil-welder interface as a function of time from the FE model. The temperature reaches a steady value which corresponds to the weld temperature measured by the IR camera in subsection 6.3.3; Temperature vs. angle plots of the welder for weld speed $\dot{x}$ of (b) 52.92 mm/s (125 in/min), (c) 84.67 mm/s (200 in/min), and (d) 116.4 mm/s (275 in/min).

6.3.3 IR Experiments and data analysis

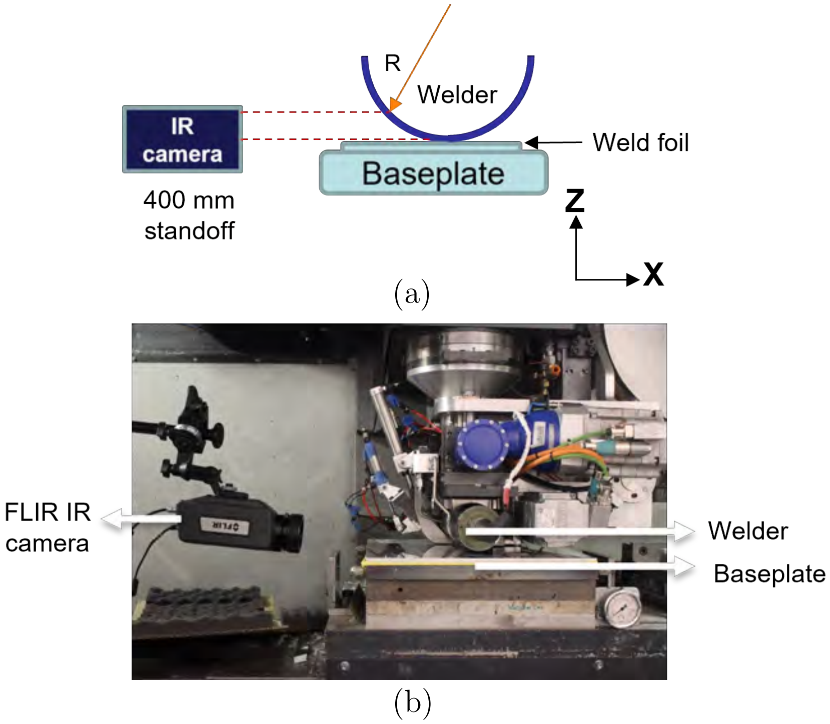
R
Welder
IR camera
Weld foil
Baseplate
400 mm standoff
Z
X
(a)
FLIR IR camera
Welder
Baseplate
(b)

Figure 6.8: Setup to measure the weld temperature during UAM in-situ: (a) illustration of the IR camera positioned to view the front of the welder during welding; (b) image of the FLIR A6751sc camera positioned using a Manfrotto boom arm.

The in-situ temperature distribution during welding was measured using a non-contact (IR) longwave infrared camera (FLIR A6751sc). A frame rate of 30 Hz was used and the response time for the IR camera to capture a temperature change is 190 µs. The spectral range chosen for the temperature range of interest for UAM was 7.5 to 11 µm. The sensor in the camera converts the incoming infrared photons into a 640x480 voltage map using the emissivity of the welder surface, which was measured to be 0.9 in a calibration experiment using a K-type thermocouple, detailed in Appendix C. The camera was mounted on a Manfrotto boom arm as shown in Figure 6.8 in the CNC machine. A standard ruler was used to calibrate the pixel-to-pixel distance at the standoff distance used. A total of 13 pixels were required for 1 mm marking on the ruler, which translates to a pixel size of 76 μm, which is about half the thickness of the UAM foil.

6.3.4 Model validation

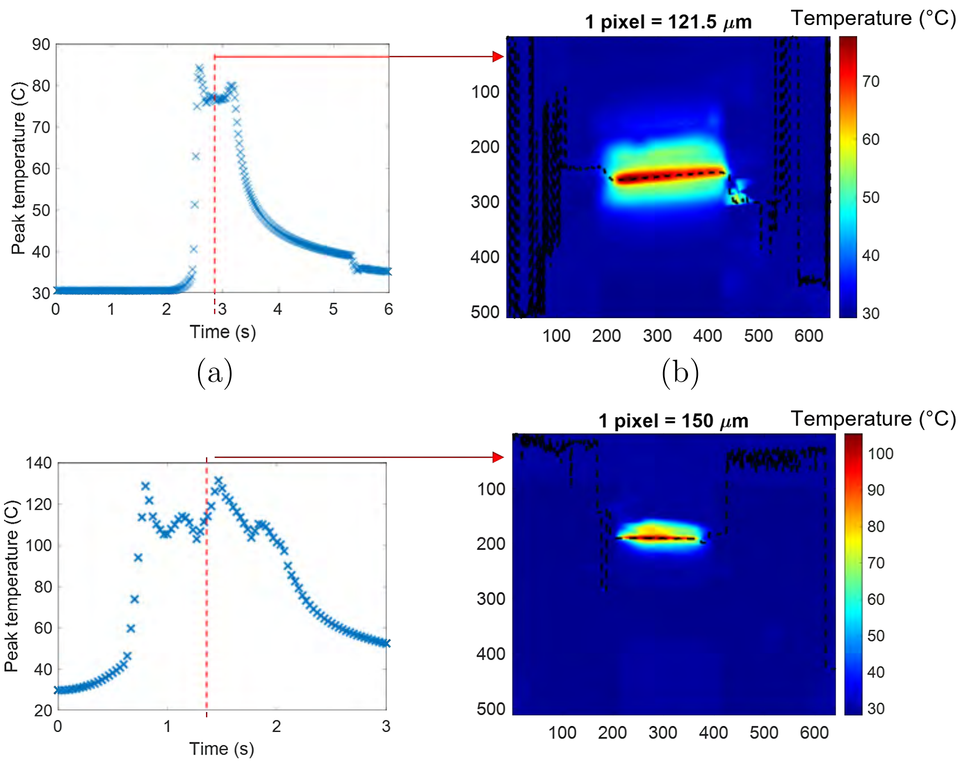

(a) (b)

(c) (d)

Figure 6.9: IR temperature measurements during the UAM of Al foils onto a 0.5 in thick Al 6061-T6 baseplate: (a) Peak temperature vs. time for Al 5052-H38, with a steady weld temperature of 74° C; (b) Infrared image during welding the welding of Al 5052-H38, where the black dotted line follows the point with maximum temperature from left to right; (c) Peak temperature vs. time for Al 6061-O, with a steady weld temperature of 118° C; (d) Infrared image during welding the welding of Al 6061-O, where the black dotted line follows the point with maximum temperature from left to right.

Al 6061-O, 6061-H18, 5052-O, and 5052-H38 feedstock were welded onto a 12.7 mm (0.5 inch) thick Al 6061-T6 baseplate. The temperature was found to be similar for the first foil to baseplate weld and the first foil to second foil welds. A representative IR image for Al 5052-H38 and Al 6061-O foils are shown in Figure 6.9(b) and Figure 6.9(d). Three key features are observed in these IR images: (i) the machined Al 6061-T6 baseplate acts as a perfect mirror creating a mirror image of the welder infrared image; (ii) the peak temperature on the welder is reached at the welder-foil interface and is uniform along the width of the foil interface; and (iii) the peak temperature of the welder is steady during the welding process, as seen in Figure 6.9(a) and Figure 6.9(c). The peak temperature estimated as the time-average of the measured maximum temperature from the infrared video during welding. The peak temperature estimated as the time-average of the measured maximum temperature from the infrared video during welding. The temperature increase for Al 6061-O foil is 88 K (peak temperature is 118° C), while the temperature increase for Al 5052-H38 is 44 K (peak temperature is 74° C). This difference is attributed to the potential difference in the Taylor-Quinney coefficient between 5000-series and 6000-series aluminum alloys.

Temperature-dependent mechanical properties for Al 6061-O, Al 5052-O, and Al 5052-H38 were obtained from the ASM materials handbook [44] for the respective alloy and temper combinations. Properties for Al 6061-H18 were experimentally obtained from uniaxial tensile testing measurements in a temperature-controlled chamber, shown in Appendix B. The yield strength of all the foils reduce by less than 10% up to 120°C, which is the maximum measured weld temperature for the range of weld parameters used. Hence, the effect of thermal softening on the yield strength of the foils is neglected in the analytical model. If the material being welded exhibits significant thermal softening during UAM, the weld temperature needs to be iterated over a range of possible values until the estimate of heat generation from the structural model with thermal softening matches that from the thermal model.

The experimentally obtained weld temperatures from infrared imaging and the corresponding temperature estimate from the analytical model are shown in Figure 6.10. The model with $\beta = 0.9$ underestimates the temperature increase for Al 6061-O, and this is attributed to the the following factors not included in the model: elongation in the X-direction, which is significant for the soft annealed material, and the energy expended in permanent work hardening (cold working) of the material during UAM. The model also overestimates the temperature increase for the 5052-series alloys, and this could be due to be an overestimation of the parameter β. The model with $\beta = 0.6$ is a better fit for the weld temperatures for Al 5052-O and Al 5052-H38.

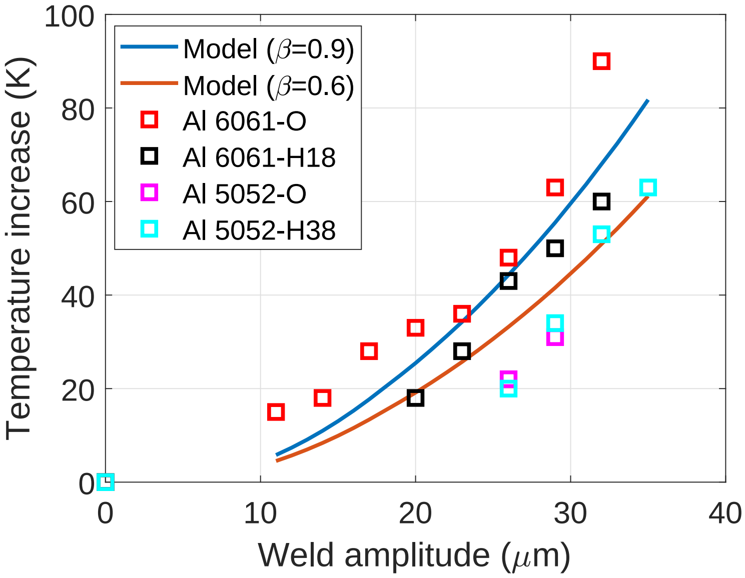

Figure 6.10: Weld temperatures for the welding of Al 6061-O, Al 6061-H18, Al 5052-O, and Al 5052-H38 measured using infrared imaging using a weld force of 5000 N and a weld speed of 84.67 mm/s (200 in/min) and varying weld amplitude. The measurements are compared against estimates from the analytical model. The total heat generated was estimated using (6.32) and input to the thermal finite element model to predict the temperature increase. Two possible values of the parameter β are chosen to account for the differences between the alloys.

6.4 Process-property relationships for the UAM of Aluminum

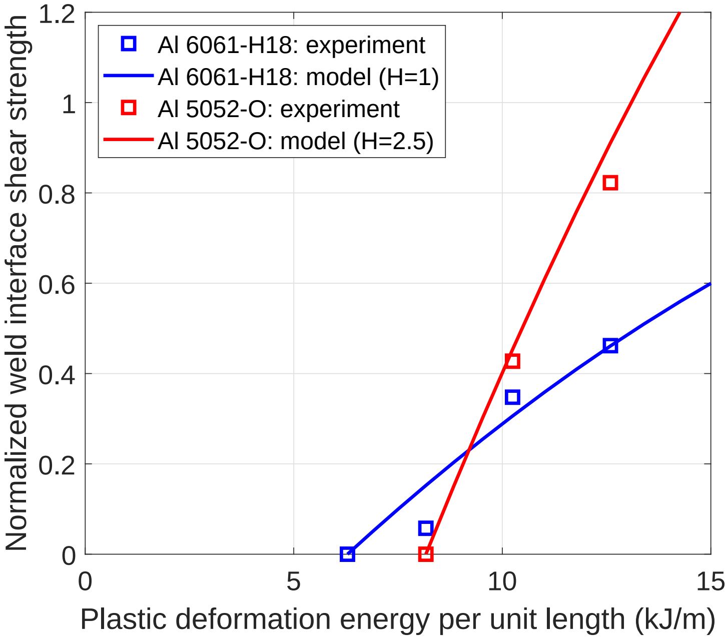

Figure 6.11: The foil−foil weld interface shear strength is measured for UAM-ed Al 6061-H18 and Al 5052-O samples welded using a weld force of 5000 N and a weld speed of 84.67 mm/s (200 in/min), and is normalized by the bulk shear strength of the foil material. The weld amplitude was varied between 23 and 32 µm to fabricate the welds. The expression in (6.37) was used to estimate the normalized weld interface shear strength. The higher increase in shear strength for Al 5052-O material is attributed to work hardening, and an empirical hardening coefficient of 2.5 was used to account for this.

A simple empirical model for the weld interface shear strength $\tau_{s,weld}$ was developed similar to the model in [24] for cold roll bonding. The shear strength of the bulk material ($\tau_{s,bulk}$) is used to normalize the shear strength of the weld. The model was modified to use the energy of plastic deformation per unit length E_{pl} instead of the thickness reduction:

$$\frac{\tau_{s,weld}}{\tau_{s,bulk}} = H\left(1 - \frac{(1 - E_{pl}/A)^2}{(1 - E_{pl}^{th}/A)^2}\right) \tag{6.37}$$

where H is an empirical hardening coefficient, Epl^{th} is the threshold energy of plastic deformation for bond formation, and A is a coefficient used to normalize the energy of plastic deformation. The value for A is chosen by fitting the model against the measurements for Al 6061-H18 to be 30 kJ/m. The value of H is set as 1 for Al 6061-H18 since the temper is fully cold-worked. The value of H for Al 5051-O is determined by fitting the model with the same value for A against measurements for Al 5052-O. The value chosen for Al 5052-O for a good fit was $H = 2.5$. The hardening coefficient H accounts for the effect of work-hardening to improve the strength of the foil material. This calibrated model can be used to determine the weld interface shear strength for the UAM of aluminum and other metals. The model is compared against experiments in Figure 6.11 and found to be in good agreement.

6.5 Energy flow map for the UAM of aluminum

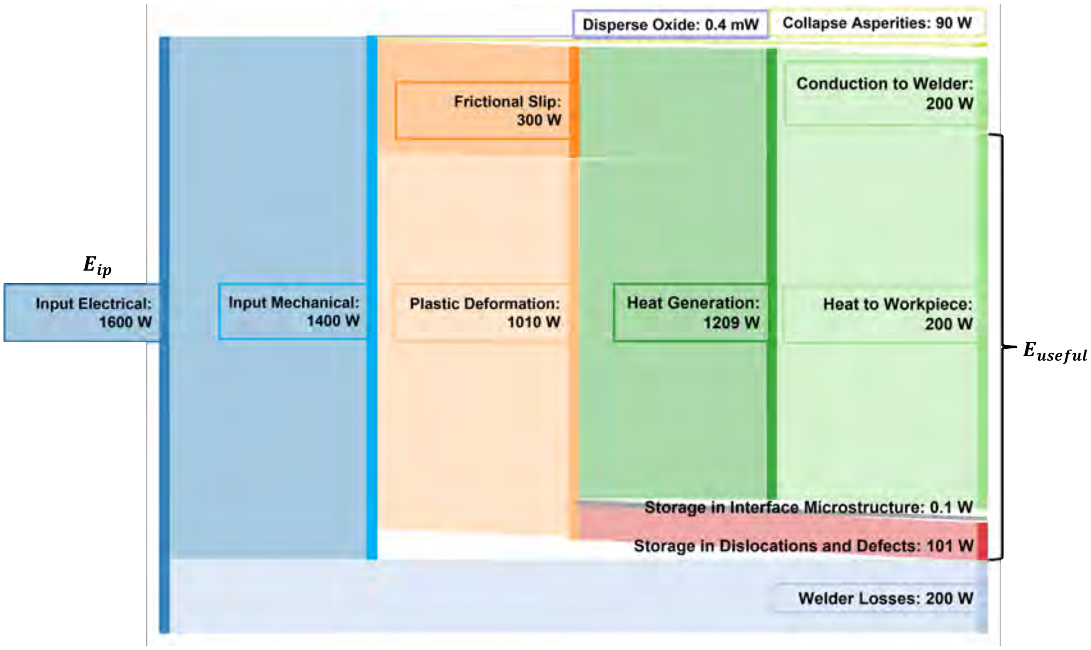
Disperse Oxide: 0.4 mW
Collapse Asperities: 90 W
Frictional Slip: 300 W
Conduction to Welder: 200 W
E_{ip}
Input Electrical: 1600 W
Input Mechanical: 1400 W
Plastic Deformation: 1010 W
Heat Generation: 1209 W
Heat to Workpiece: 200 W
E_{useful}
Storage in Interface Microstructure: 0.1 W
Storage in Dislocations and Defects: 101 W
Welder Losses: 200 W

Figure 6.12: Flow of electrical energy per unit time (E_{ip}) from the welder (electrical) to the different energies involved in the UAM process. A energies were estimated using the following weld parameters for the UAM of Al 6061-H18: weld amplitude of 32 μm, weld speed of 84.67 mm/s (200 in/min), and a weld force of 5000 N. The useful energy E_{useful} for bond formation is defined in (6.38).

A comprehensive map of all the energies involved in the UAM process is shown in Figure 6.12. The input electrical energy E_{ip} is converted into mechanical work at the welder−foil interface, and this efficiency is computed in [35] to be about 85% during the welding process. The remaining energy is lost as heat in the piezoelectric transducers and the wave guide.

The rate of energy required to disperse the oxide layer for aluminum is computed in Appendix A, and is found to be an insignificant fraction of the input energy. The remaining mechanical energy is converted predominantly into the two key energies involved in the process − plastic deformation and frictional slip. The rest is assumed to be used to collapse the asperities in the surface of the two foils being welded. About 90% of the plastic deformation energy is assumed to be converted to heat ($\beta = 0.9$), and the frictional dissipation is completely converted to heat. About 16.5% of the generated heat is conducted to the steel welder, and the remaining 83.5% increases the temperature of the foil and workpiece.

About 10% of the plastic deformation energy is used for the creation, rearrangement of crystal defects and the formation of dislocation structures [98]. It is expected from the dislocation density-based crystal plasticity model developed in [99] that the geometrically-necessary dislocation (GND) density increases with each cycle of vibration from the welder, which is a means to store the energy of plastic deformation. The work found that a GND density of 6×10^{15} m^{-2} is expected after 3000 cycles of deformation for the UAM of Al 3003-H18. The statistically-stored dislocation density is much smaller than the geometrically-necessary dislocation density, and can be neglected. This dislocation density determines the sub-grain diameter in the resulting microstructure.

A figure of merit can defined for the UAM process from the energy flow map as the fraction of input electrical energy that is used for bond formation. Plastic deformation is the key driver of solid-state bond formation, and hence $1 - \beta$, or 10% of the plastic deformation energy is used directly for bond formation. In addition, part of the heat generated also lowers the yield stress of the foil material, reducing the weldability threshold E_{pl}^{th} from (6.37). This reduction is characterization by the relationship between the flow stress (or yield stress) and temperature which is typically modeled as a power law relationship for most aluminum alloys [100]. The useful energy is thus the portion of heat generation that is not lost via conduction to the welder. The useful energy E_{useful} and the figure of merit α are thus defined as

$$\begin{aligned} E_{useful} &= (1-\beta)E_{pl} + 0.83 q_{total}, && (6.38) \\ \alpha &= \frac{E_{useful}}{E_{ip}}. && (6.39) \end{aligned}$$

The figure of merit for the case described in Figure 6.12 is computed to be 69.4%. This value is lower than the efficiency of the welding assembly, which is close to 85%.

The figure of merit α in (6.39) is dependent on the following factors: (i) the thermal properties of the foil and horn which determines the heat partition coefficient at the interface; (ii) Taylor-Quinney coefficient β of the foil material; (iii) success of weld formation which determines the partition between plastic deformation and frictional slip; (iv) foil and workpiece geometry. Each of these factors can be adjusted to improve the figure of merit of UAM. The modification of the horn surface with a surface coating to improve thermal insulation has been shown to increase the weld temperature [101].

6.6 Conclusions

A model for the flow of energy in the UAM of aluminum is developed by quantifying the different energies involved in the UAM process. To guide model development, the UAM of annealed and fully work-hardened tempers of 6061 and 5052 aluminum alloys was investigated. Infrared thermography is used to measure in-situ weld temperature as a function of vibration amplitude. A temperature increase of up to 100 K was observed for the UAM of Al foils using weld amplitudes between 11 and 35 μm.

A transient thermal FE model for heat transfer was developed and validated using the infrared temperature measurements. The validated model is able to estimate the relative fraction of heat generation from plastic deformation and friction, enabling the estimation of weld temperature. This model is useful for the embedding of sensitive sensors and materials using UAM, since the process parameters can be chosen such that the weld temperature reached is below the critical or highest safe temperature of the sensitive material to avoid thermal degradation.

The strength of the weld interfaces is quantified utilizing a shear tester. Shear strengths of up to 50% of the bulk value were measured for the UAM of Al 6061-H18 and up to 80% for the UAM of Al 5052-O. The stronger dependence of weld strength on weld amplitude for Al 5052-O is attributed to the work hardening of the annealed foil during the cyclic plastic deformation in UAM, which is absent for the fully-hardened Al 6061-H18. An empirical relationship between the energy of plastic deformation as a function of weld parameters and weld strength was also established using expressions from cold roll bonding literature. The expression accounts for the strength increase with a hardening coefficient and the calibrated model can be used to predict the strength of UAM Al as a function of process parameters.

The flow of energy in the UAM of aluminum is mapped, and the different energies involved in the UAM process are quantified. The formulation is used to develop a figure of merit to qualify the proportion of input energy that is used for bond formation, which is computed to be 69.4%. This figure of merit can be used as a design criterion for an improved use of the input electrical energy for bond formation in UAM, reducing wasted forms of energy such as conduction to the welder or losses in the piezoelectric transducers.

Chapter 7

Conclusions and Future Work

7.1 Summary of findings

In Chapter 2, a lumped parameter LTI model of the UAM welder coupled to the materials being welded during UAM has been developed to predict the weld power at a given weld amplitude as a function of the overall system's compliance, considering the contributions of the foil material being welded, the workpiece being welded onto, and the fixture. The non-linear relationship between weld power and system stiffness has been presented, along with a linearized relationship that has been shown to provide a good approximation. Prior to this study, predictive relations for UAM weld power have not been successfully developed.

Modal analysis and finite element modeling are used to estimate the different component compliances, and an equivalent circuit model is used to describe the overall system's compliance, which is then used to compute the weld power for a given weld amplitude setting. The model shows good agreement with measurements for a variety of build and fixture configurations tested: up to 20 layers of Al welded onto baseplates with different stiffnesses; up to 10 layers of Cu welded onto an Al baseplate; and a 2-layer build with different alloys and tempers of Al and Cu foil. Model predictions of higher weld power for stiffer (lower compliance) builds agree with experimental data. Weld power is also found to be largely insensitive to foil type (and hence foil strength) within the Al foils, although different welder effort is required to satisfactorily weld different foil types. A framework has been developed to determine the weld amplitude setpoint to obtain a target weld power for a given build configuration.

These observations support the conclusion that the elastic compliance of the system has the most dominant influence on weld power. This modeling framework, using a calibrated damping coefficient, can predict the weld amplitude required to reach a certain target weld power for different welder, workpiece, and fixture designs. This reduces the need for time-consuming pilot weld studies for new UAM build materials, configurations, and systems.

In Chapter 3, a new experimental technique was developed to track the in-situ vibration velocities of either the weld stack, welder, or the standard 0.152 μm thick weld foil used during the UAM process. This is the first-time that UAM foil velocity and transducer voltage during welding have been measured synchronously, and used for real-time tracking of the UAM process and better understanding of the dynamics of the vibration velocity of the two foils being welded during UAM. The in-situ bond tracking technique developed using a Doppler velocimeter has been used to correlate dynamic vibration velocity behavior with bond quality. A binary indicator for weld quality for UAM was developed using laser Doppler velocimetry, and validated for the UAM of Al 6061-H18 and 110Cu foils. The metric developed can reliably identify successful and unsuccessful UAM welds in-situ, and can be used to support an automated weld parameter search as detailed in Figure 3.8. The weld quality monitoring setup enables in-line quality control and defect identification for UAM. This approach can also be used for closed-loop process control of UAM by monitoring the metric θ in-situ.

In Chapter 4, EBSD was used a tool for quantitative comparison of post-UAM microstructures. First, the effect of subsequent weld layers on weld microstructure was investigated by welding up to 9-subsequent layers of foil over a Al 6061-H18 foil-foil weld built using the following settings: 32 µm weld amplitude, 5000 N weld force, and 84.67 mm/s (200 in/min) weld speed. A technique was developed to determine the location and width of the interface region from the raw EBSD data. The interface width was estimated to be about 14 µm for the 2-, 3-, 5-, and 10-layer samples, which is within previous literature estimates of the weld interface region.

Nanoindentation was also introduced as a companion testing method to obtain the location and size of the weld interface region as a region of higher hardness compared to the bulk microstructure. The interface width from nanoindentation matches with the estimate from EBSD. The following metrics were developed to quantify differences in weld interface microstructure – interface width, average grain size and percentage of grain boundaries that are High Angle Boundaries (% HAGB). Within the margin of error of EBSD due to its resolution limit, there is no significant effect of subsequent welds on the UAM weld interface microstructure for the sample heights and dimensions investigated with the metrics used.

Second, a study was developed to quantify the effect of UAM process parameters on the weld interface microstructure by measuring the energy stored in the microstructure. The Read-Shockley relationship was used to computed the stored energy in the grain boundaries obtained using the MTEX toolbox from the EBSD scans. A peak in the density and magnitude of stored energy was observed at the weld interface, which was absent in the control as-received foil sample. Stored energy and interface width was observed to monotonously increase with weld amplitude at a fixed weld speed of 84.67 mm/s (200 in/min), but found not to be sensitive to weld speed at a fixed weld amplitude of 29 μm.

In Chapter 5, it was found that changing the surface texture of pre-weld Al 6061-H18 foil using pretexturing causes no measurable change in the weld interface strength for the range of parameters tested. Surface preparation using pretexturing hence is not a viable method to improve bond quality in UAM for Al 6061-H18 in the range of parameters tested. Changing the pre-weld surface roughness is not found to affect the input energy into the weld for Al 6061-H18 within the range of parameters tested. It is thus proposed that the asperities are completely collapsed due to the normal pressure before cyclic deformations from the welder.

In Chapter 6, infrared thermography is used to measure in-situ process temperature as a function of vibration amplitude and weld speed. The strength of the weld interfaces is quantified utilizing a shear tester. A transient thermal FE model for heat transfer was developed and validated using infrared temperature measurements. The validated model is able to estimate the relative fraction of heat generation from plastic deformation and friction, enabling the estimation of weld temperature. This model is useful for the embedding of sensitive sensors and materials using UAM, since the process parameters can be chosen such that the weld temperature reached is below the critical or highest safe temperature of the sensitive material to avoid thermal degradation. An empirical relationship between the energy of plastic deformation as a function of weld parameters and weld strength was also established using expressions from cold roll bonding literature. The expression accounts for the strength increase with a hardening coefficient and the calibrated model can be used to predict the strength of UAM Al as a function of process parameters. A figure of merit is developed which is used to compute the fraction of input energy used for bond formation, and thus a metric that can be used for designing UAM systems to be more effective by reducing energy losses.

7.2 Contributions

1. The interrelation between workpiece materials and the UAM process was studied with three different weld foil materials, and it was found that the failure properties of the weld foil do not substantially affect the weld power draw. Instead, the elastic system compliance, including the baseplate material and fixture, was found to have a dominant effect on welder effort [94].

2. Developed an in-situ process quality monitoring technique using Doppler velocimetry to distinguish between successful and unsuccessful UAM welds without human intervention, enabling closed-loop process control and automated process parameter search.

3. Quantified the energy stored in the weld interface microstructure and evaluated trends of energy stored as a function of process settings and input energy.

4. Built a calibrated thermal model for UAM capable of predicting weld temperatures, enabling process parameter design for the embedment of temperature-sensitive materials.

5. Developed an empirical process-property relationship between the energy of plastic deformation as a function of process parameters and the shear strength of the weld interface.

6. Developed a figure of merit which can be used to optimize the different components of the UAM process to reduce wasted energy not used for bond formation.

7.3 Future work

Process control

The weld power-compliance relationship developed requires a comprehensive modal analysis and finite element analysis to be conducted with previous knowledge of the material properties and dimensions of the workpiece. The first future work would be to develop a simple in-situ dynamic stiffness estimation method which uses a high-frequency modal hammer to directly estimate the system stiffness without the need for a CAD geometry. This will be very useful in the UAM of foil onto complex shapes and large support structures which might require extensive modeling. The technique developed would involve a modal hammer attached to the weld assembly which uses an impact and the structural response measured either using an accelerometer or a non-contact laser vibrometer. The welder controller would be augmented to be able to compute the force-response transfer function and the dynamic system stiffness directly from these measurements.

Another future work is to build a closed-loop process controller using the in-situ quality monitoring method as a check on weld quality. Closed-loop control is crucial to improve process robustness enabling the adoption of UAM for high-throughput manufacturing. There are unpredictable factors which can cause a failed weld: feedstock quality issue, surface contamination, poor welder surface quality, fixture misalignment, etc. In-line quality inspection using the scanning Doppler vibrometer should be used to scan for instances of unsuccessful bonding. The scanning vibrometer could be replaced with a multi-point laser vibrometer. This will avoid the delay due to the time required for the servo motors in the vibrometer to move the laser spot between points in the grid, enabling an instantaneous weld quality detection. The vibration velocity of the foil has components at frequencies that are multiples of the excitation frequency (40 kHz, 60 kHz, 80 kHz). Another future work could investigate the relationship between the magnitude and phase of these components in the frequency domain and the quality of the welds produced.

Modeling

The analytical model developed for the energy of plastic deformation accounts for the effect of weld temperature from the thermal model, but the model was only tested against measurements conducted at room temperature. The threshold for bond formation is found to typically decrease with an increase in pre-heat temperature in solid-state processes, and pre-heat is often used for the UAM of high-strength materials such as steel or titanium. Another future work is to validate the thermal-structural model developed for varying pre-heat temperature, and investigate the effect of weld temperature on the threshold for bond formation. Some steels undergo phase transformation at critical temperatures, and this could affect the material properties substantially during UAM. Hence, a detailed investigation on the pre-heat temperature as a process variable needs to conducted, especially for high-strength materials such as steels.

The analytical framework developed for the estimation of plastic deformation energy does not account for work hardening which is typical in annealed foils used in UAM. Work hardening will increase the bulk hardness and the resulting bond strength of UAM-ed parts. Another future work is the use of nanoindentation studies to characterize this change in hardness due to cold working in UAM, and augment the plasticity model to include work hardening in the flow stress model.

The model developed for process-property relationships still requires some empirical parameters to match experimental results. An important future work is the determination of the threshold plastic deformation energy without the need for experimental studies. The threshold needs to be obtained directly from mechanical and thermal properties of the foil material being welded that can easily be obtained from characterization tests or material databases. This will enable the selection of process parameters for novel materials to be welded without the need for expensive and time-consuming trials.

Appendix A

Energy required to disperse the oxide layer

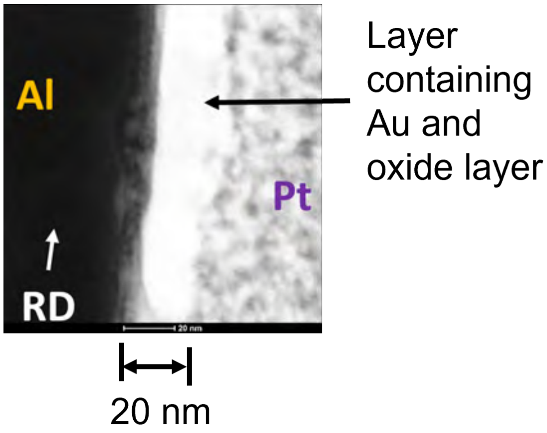

Figure A.1: TEM measurements of air-grown oxide layer of as-received Al 6061-H18 foil at room temperature. The thickness of the oxide layer is found to be less than 20 nm. RD denotes the rolling direction of the welder. To the left is as-received foil, and to the right is the deposited platinum and gold. The bright segment in the middle contains the oxide layer of Al.

To enable metal-metal contact for consolidation to occur during UAM, it is required that the oxide layer be removed by the scrubbing action of the welder during welding. The energy required to remove the oxide layer, which is related to its thickness, can be estimated as follows. The thickness of the layer is measured by depositing a layer of gold and platinum on as-received Al 6061-H18 foil, and cutting a cross-section sample using FEI Helios DualBeam FIB. Technai 20 TEM was used to produce the TEM image to identify the oxide layer thickness. The thickness t_{oxide} was measured to be less than 20 nm, shown in Figure A.1, which is much smaller than the 0.15 mm thickness of the foil. This agrees with previous oxide film thickness measurements in aluminum in [102].

The failure strain of alumina oxide film is typically in the order of 0.1% to 0.5% and can be as high as 2% in steels at high temperature [103]. Since the films behave elastically to the point of fracture due to their brittle nature [104], the modulus E_{oxide} and failure strain $\varepsilon_{f,oxide}$ can be used to estimate the energy to fail a volume V_{oxide} the oxide layer, E_{oxide}. The modulus of the alumina layer is between 2 and 4 GPa [102].

$$E_{oxide} = \frac{1}{2} E_{oxide} \varepsilon_{f,oxide} V_{oxide}. \tag{A.1}$$

This expression can be used to calculate the fraction of electrical power input expended to fracture the oxide layer in Figure 6.12 by substituting the upper limits of the expected values, as 0.4 mW.

Appendix B

Temperature-dependent flow stress of Al 6061-H18 foil

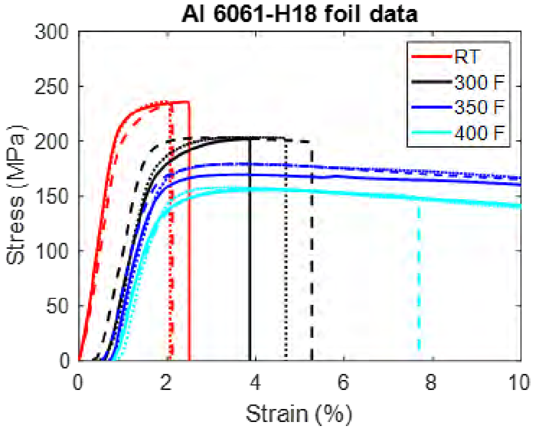

Figure B.1: Stress vs. strain curves from uniaxial tensile testing of as-received Al 6061-H18 foil conducted at different controlled temperatures (86, 300, 350, and 400 F).

As-received Al 6061-H18 foil which was 0.152 mm thick and 25.4 mm wide was tested to failure using a tensile tester in a temperature-controlled chamber. These measurements were used to estimate the temperature-dependence of the tensile behavior of as-received foil material. The yield strength decreases with an increase in temperature, while the ductility increases, seen in in Figure B.1. The tensile yield strength estimated from these curves are tabulated as a function of temperature in Table B.1.

Table B.1: Summary of temperature-dependent yield strength of as-received Al 6061-H18 foil.

Temperature (F)	Temperature (K)	Flow stress (MPa)
85	303	230
300	422	200
350	450	170
400	478	150

Appendix C

Calibration of infrared emissivity of the welder surface

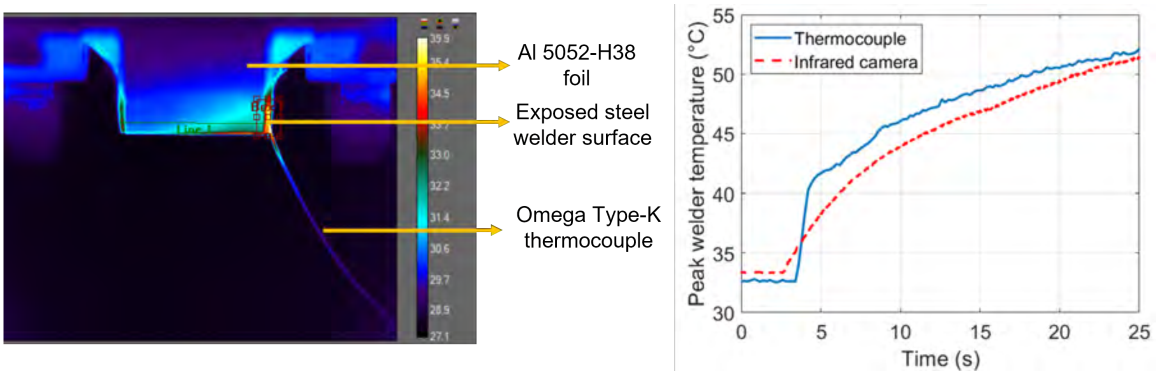

(a) (b)

Figure C.1: Calibration of the infrared emissivity of the steel welder using a OMEGA Type K AWG 40 thermocouple (0.080 mm tip diameter): (a) Infrared image of the setup showing the thermocouple bonded to the side of the welder and the infrared camera estimating the welder temperature from the exposed surface of the steel welder (enclosed in the red rectangle); (b) Comparison of the measured temperatures estimated using the thermocouple and infrared images.

Al 5052-H38 foil which was 0.152 mm thick and 25.4 mm wide was fed using the tape feeder and tensioned using a force of 90 N around the welder. An OMEGA Type K AWG 40 thermocouple (0.080 mm tip diameter) was bonded to the side of the steel welder using superglue to measure the temperature at the interface of the steel welder, shown in Figure C.1(a). Figure C.1(a) also shows the exposed portion of the welder where the infrared measurements are made. This is possible since the welder is 10% wider than the foil. The transducers were excited at a vibration amplitude of 26 μm to generate heat through sliding friction between the vibrating welder and the aluminum foil. The foil surface does not reflect its true temperature to the infrared camera since the emissivity of shiny aluminum foil is too low (<0.1). The emissivity value of the steel surface was varied until good agreement (within 3 K) was seen between the infrared and thermocouple temperature estimates. The small differences are attributed to the effect of the superglue on the time constant of the thermocouple and the small distance between the location of thermocouple bonding and the surface seen by the camera. An emissivity value of 0.9 was chosen for the steel welder using this method.

Bibliography

[1] L Li, K Nagai, and F Yin. Progress in cold roll bonding of metals. Science and Technology of Advanced Materials, 9(2):023001, 2008.

[2] K Graff, M Short, and M Norfolk. Very high power ultrasonic additive manufacturing (VHP UAM) for advanced materials. In Solid Freeform Fabrication Symposium, Austin, TX, 2010.

[3] D White. Ultrasonic consolidation of aluminum tooling. Advanced Materials & Processes, 161(1):64–65, 2003.

[4] J O Obielodan, A Ceylan, L E Murr, and B E Stucker. Multi-material bonding in ultrasonic consolidation. Rapid Prototyping Journal, 16(3):180–188, 2010. `https://doi.org/10.1108/13552541011034843`.

[5] M R Sriraman, M Gonser, H T Fujii, S S Babu, and M Bloss. Thermal transients during processing of materials by very high power ultrasonic additive manufacturing. Journal of Materials Processing Technology, 211(10):1650–1657, 2011. `https://doi.org/10.1016/j.jmatprotec.2011.05.003`.

[6] Tianyang Han. Ultrasonic Additive Manufacturing of Steel: Process, Modeling, and Characterization. PhD thesis, The Ohio State University, 2020.

[7] K Graff, M Short, and M Norfolk. Very high power ultrasonic additive manufacturing (vhp uam). In International solid freeform fabrication symposium, Austin, TX, 2011.

[8] C Y Kong, R C Soar, and P M Dickens. Optimum process parameters for ultrasonic consolidation of 3003 aluminium. Journal of Materials Processing Technology, 146(2):181–187, 2004. `https://doi.org/10.1016/j.jmatprotec.2018.02.001`.

[9] P J Wolcott, A Hehr, and M J Dapino. Optimized welding parameters for Al 6061 ultrasonic additive manufactured structures. Journal of Materials Research, 29(18):2055–2065, 2014. `https://doi.org/10.1557/jmr.2014.139`.

[10] T Han, C H Kuo, N Sridharan, L M Headings, S S Babu, and M J Dapino. Effect of preheat temperature and post-process treatment on the microstructure and mechanical properties of stainless steel 410 made via ultrasonic additive manufacturing. Materials Science and Engineering: A, 769:138457, 2020. `https://doi.org/10.1016/j.msea.2019.138457`.

[11] R Gonzalez and B E Stucker. Experimental determination of optimum parameters for stainless steel 316l annealed ultrasonic consolidation. Rapid Prototyping Journal, 18(2):180–182, 2012. `https://doi.org/10.1108/13552541211212159`.

[12] N Sridharan, P J Wolcott, M J Dapino, and S S Babu. Microstructure and texture evolution in aluminum and commercially pure titanium dissimilar welds

fabricated using ultrasonic additive manufacturing. Scripta Materialia, 117:1–5, 2016. `https://doi.org/10.1016/j.scriptamat.2016.02.013`.

[13] Y Gao and C Doumanidis. Mechanical analysis of ultrasonic bonding for rapid prototyping. Journal of Manufacturing Science and Engineering, 124(2):426–434, 2002.

[14] P J Wolcott. Ultrasonic Additive Manufacturing: Weld Optimization for Aluminum 6061, Development of Scarf Joints for Aluminum Sheet Metal, and Joining of High Strength Metals. PhD thesis, The Ohio State University, Columbus, OH, USA, 2015.

[15] A Hehr, P J Wolcott, and M J Dapino. Effect of weld power and build compliance on ultrasonic consolidation. Rapid Prototyping Journal, 22(2):377–386, 2016. `https://doi.org/10.1108/rpj-11-2014-0147`.

[16] D Li. A review of microstructure evolution during ultrasonic additive manufacturing. The International Journal of Advanced Manufacturing Technology, pages 1–19, 2021.

[17] M R Sriraman, S S Babu, and M Short. Bonding characteristics during very high power ultrasonic additive manufacturing of copper. Scripta Materialia, 62(8):560–563, 2010.

[18] G S Kelly, S G Advani, and J W Gillespie. A model to describe stick–slip transition time during ultrasonic consolidation. The International Journal of Advanced Manufacturing Technology, 79(9):1931–1937, 2015.

[19] D Yi, S Zhang, H Zhang, L Zheng, and M Norfolk. Power consumption and friction coefficient in the ultrasonic consolidation of aluminium alloys. Materials Science and Technology, 33(6):744–750, 2017. `https://doi.org/10.1080/02670836.2016.1254912`.

[20] C Zhang and L Li. A friction-based finite element analysis of ultrasonic consolidation. Welding Journal, 87(7):187, 2008.

[21] H A Mohamed and J Washburn. Mechanism of solid state pressure welding. AWS Welding Journal, 1975.

[22] A A Ward and Z C Cordero. Junction growth and interdiffusion during ultrasonic additive manufacturing of multi-material laminates. Scripta Materialia, 177:101–105, 2020.

[23] G S Kelly, M S Just Jr, S G Advani, and J W Gillespie Jr. Energy and bond strength development during ultrasonic consolidation. Journal of Materials Processing Technology, 214(8):1665–1672, 2014.

[24] P K Wright, D A Snow, and C K Tay. Interfacial conditions and bond strength in cold pressure welding by rolling. Metals Technology, 5(1):24–31, 1978.

[25] R Jamaati and M R Toroghinejad. Cold roll bonding bond strengths. Materials Science and Technology, 27(7):1101–1108, 2011.

[26] D R Cooper and J M Allwood. The influence of deformation conditions in solid-state aluminium welding processes on the resulting weld strength. Journal of Materials Processing Technology, 214(11):2576–2592, 2014.

[27] N Bay, C Clemensen, O Juelstorp, and T Wanheim. Bond strength in cold roll bonding. CIRP Annals, 34(1):221–224, 1985.

[28] W Zhang and N Bay. A numerical model for cold welding of metals. CIRP annals, 45(1):215–220, 1996.

[29] W J Joost. Reducing vehicle weight and improving us energy efficiency using integrated computational materials engineering. JOM, 64(9):1032–1038, 2012.

[30] S C Davis and P S Hu. Transportation energy data book. NASA STI/Recon Technical Report N, 91:24681, 1991.

[31] H Ahn, M B Gingerich, R Hahnlen, M J Dapino, and F Pourboghrat. Numerical modeling of mechanical properties of uam reinforced aluminum hat sections for automotive applications. International Journal of Material Forming, pages 1–12, 2021.

[32] S K Chilelli, J J Schomer, and M J Dapino. Detection of crack initiation and growth using fiber bragg grating sensors embedded into metal structures through ultrasonic additive manufacturing. Sensors, 19(22):4917, 2019.

[33] A K Ramanathan, M B Gingerich, L M Headings, and M J Dapino. Metal structures embedded with piezoelectric PVDF sensors using ultrasonic additive manufacturing. Manufacturing Letters, 2021.

[34] R J Friel. Power ultrasonics for additive manufacturing and consolidating of materials. In Power Ultrasonics, pages 313–335. Elsevier, 2015. `https://doi.org/10.1016/B978-1-78242-028-6.00013-2`.

[35] A Hehr and M J Dapino. Dynamics of ultrasonic additive manufacturing. Ultrasonics, 73:49–66, 2017. `https://doi.org/10.1016/j.ultras.2016.08.009`.

[36] C W De Silva. Vibration damping, control, and design. CRC Press, 2007. `https://doi.org/10.1201/9781420053227`.

[37] M Wiercigroch, R D Neilson, and M A Player. Material removal rate prediction for ultrasonic drilling of hard materials using an impact oscillator approach. Physics Letters A, 259(2):91–96, 1999. `https://doi.org/10.1016/s0375-9601(99)00416-8`.

[38] Z Y Wang and K P Rajurkar. Dynamic analysis of the ultrasonic machining process. Journal of Manufacturing Science and Engineering, 118(3):376–381, 1996. `https://doi.org/10.1115/1.2831039`.

[39] E Diez, E Leal-Muñoz, H Perez, and A Vizan. Dynamic analysis of a piezoelectric system to compensate for workpiece deformations in flexible milling. Mechanical Systems and Signal Processing, 91:278–294, 2017. `https://doi.org/10.1115/1.2831039`.

[40] J M Gibert, E M Austin, and G Fadel. Effect of height to width ratio on the dynamics of ultrasonic consolidation. Rapid Prototyping Journal, 16(4):284–294, 2010. `https://doi.org/10.1108/13552541011049306`.

[41] B Bhushan. Contact between solid surfaces. In Introduction to tribology. John Wiley and Sons Ltd, West Sussex, United Kingdom, 2013. `https://doi.org/10.31399/asm.hb.v02.9781627081627`.

[42] A Hehr. Process Control and Development for Ultrasonic Additive Manufacturing with Embedded Fibers. PhD thesis, The Ohio State University, Columbus, OH, USA, 2016.

[43] B Ducharne, D Guyomar, G Sébald, and B Zhang. Modeling energy losses in power ultrasound transducers. In Power Ultrasonics, pages 241–256. Elsevier, 2015. `https://doi.org/10.1016/B978-1-78242-028-6.00010-7`.

[44] ASM Handbook Committee. Properties and selection: Nonferrous alloys and special-purpose materials . In ASM Handbook Vol. 2. ASM International, Materials Park, OH, 1990. `https://doi.org/10.31399/asm.hb.v02.9781627081627`.

[45] H Zheng, B Qi, and M Yang. Dynamic analysis of the ultrasonic-frequency pulsed gmaw metal transfer process. Journal of Manufacturing Processes, 62:283–290, 2021.

[46] K Zhou and P Yao. Overview of recent advances of process analysis and quality control in resistance spot welding. Mechanical Systems and Signal Processing, 124:170–198, 2019.

[47] S Shawn Lee, C Shao, T Hyung Kim, S Jack Hu, E Kannatey-Asibu, W W Cai, J Patrick Spicer, and J A Abell. Characterization of ultrasonic metal welding by correlating online sensor signals with weld attributes. Journal of Manufacturing Science and Engineering, 136(5), 2014.

[48] S Ling, D Zhang, S Yi, and S W Foo. Real-time quality evaluation of wire bonding using input impedance. IEEE Transactions on Electronics Packaging Manufacturing, 29(4):280–284, 2006.

[49] Eugen Foca, Juergen Carstensen, Georgi Popkirov, and Helmut Foell. Controlling macropores etching in n-si by means of in-situ fft voltage-and photoimpedance spectroscopy. ECS Transactions, 6(2):345, 2007.

[50] D R Foster, G A Taber, S S Babu, and G S Daehn. In situ velocity measurements of very high power ultrasonic additive manufacturing using a photonic doppler velocimeter. Science and Technology of Welding and Joining, 19(2):157–163, 2014.

[51] V K Nadimpalli, J K Na, D T Bruner, B A King, L Yang, and B E Stucker. In-situ non-destructive evaluation of ultrasonic additive manufactured components. In Solid Freeform Fabrication: 27th Annual International, Solid Freeform Fabrication Symposium—An Additive Manufacturing Conference (TOC), Austin, TX, USA, pages 8–10, 2016.

[52] N Sridharan, P Wolcott, M J Dapino, and S S Babu. Microstructure and texture evolution in aluminum and commercially pure titanium dissimilar welds fabricated using ultrasonic additive manufacturing. Scripta Materialia, 117:1–5, 2016.

[53] S Shimizu, H T Fujii, Y S Sato, H Kokawa, M R Sriraman, and S S Babu. Mechanism of weld formation during very-high-power ultrasonic additive manufacturing of al alloy 6061. Acta Materialia, 74:234–243, 2014.

[54] P Li, Z Wang, M Diao, C Guo, J Wang, C Zhao, and F Jiang. Dynamic recrystallization and recovery in very high-power ultrasonic additive manufacturing. Advanced Engineering Materials, 23(3):2000958, 2021.

[55] N Sridharan, M Norfolk, and S S Babu. Characterization of steel-Ta dissimilar metal builds made using very high power ultrasonic additive manufacturing (VHP-UAM). Metallurgical and Materials Transactions A, 47(5):2517–2528, 2016.

[56] M Pagan, C Petrie, D Leonard, N Sridharan, S Zinkle, and S S Babu. Interdiffusion of elements during ultrasonic additive manufacturing. Metallurgical and Materials Transactions A, 52(3):1142–1157, 2021.

[57] A A Ward, M R French, D N Leonard, and Z C Cordero. Grain growth during ultrasonic welding of nanocrystalline alloys. Journal of Materials Processing Technology, 254:373–382, 2018.

[58] H T Fujii, M R Sriraman, and S S Babu. Quantitative evaluation of bulk and interface microstructures in Al-3003 alloy builds made by very high power ultrasonic additive manufacturing. Metallurgical and Materials Transactions A, 42(13):4045–4055, 2011.

[59] P Li, Z Wang, M Diao, C Guo, J Wang, C Zhao, and F Jiang. Effect of processing parameters on bond properties and microstructure evolution in ultrasonic additive manufacturing (UAM). Materials Research Express, 8(3):036507, 2021.

[60] S Choi and Y Jin. Evaluation of stored energy in cold-rolled steels from ebsd data. Materials Science and Engineering: A, 371(1-2):149–159, 2004.

[61] F J Humphreys. Reconstruction of grains and subgrains from electron backscatter diffraction maps. Journal of Microscopy, 213(3):247–256, 2004.

[62] F Bachmann, R Hielscher, and H Schaeben. Texture analysis with MTEX–free and open source software toolbox. In Solid State Phenomena, volume 160, pages 63–68. Trans Tech Publications, 2010.

[63] N Kamikawa, X X Huang, Y Kondo, T Furuhara, and N Hansen. Stored energy and annealing behavior of heavily deformed aluminium. In Materials Science Forum, volume 715, pages 367–372. Trans Tech Publ, 2012.

[64] M B Bever, D L Holt, and A L Titchener. The stored energy of cold work. Progress in Materials Science, 17:5–177, 1973.

[65] M Taheri, H Weiland, and A Rollett. A method of measuring stored energy macroscopically using statistically stored dislocations in commercial purity aluminum. Metallurgical and Materials Transactions A, 37(1):19–25, 2006.

[66] D E Schick, R M Hahnlen, R Dehoff, P Collins, S S Babu, M J Dapino, and J C Lippold. Microstructural characterization of bonding interfaces in aluminum 3003 blocks fabricated by ultrasonic additive manufacturing-methods were examined to link microstructure and linear weld density to the mechanical properties of ultrasonic additive manufacturing. Welding Journal, 89(5):105S, 2010.

[67] D Li and R C Soar. Plastic flow and work hardening of al alloy matrices during ultrasonic consolidation fibre embedding process. Materials Science and Engineering: A, 498(1-2):421–429, 2008.

[68] P Peyre, G Sierra, F Deschaux-Beaume, D Stuart, and G Fras. Generation of aluminium–steel joints with laser-induced reactive wetting. Materials Science and Engineering: A, 444(1-2):327–338, 2007.

[69] N X Randall, M Vandamme, and F J Ulm. Nanoindentation analysis as a two-dimensional tool for mapping the mechanical properties of complex surfaces. Journal of Materials Research, 24(3):679–690, 2009.

[70] R R Ambriz, D Chicot, N Benseddiq, G Mesmacque, and S D De La Torre. Local mechanical properties of the 6061-t6 aluminium weld using micro-traction and instrumented indentation. European Journal of Mechanics-A/Solids, 30(3):307–315, 2011.

[71] R Rodrıguez and I Gutierrez. Correlation between nanoindentation and tensile properties: influence of the indentation size effect. Materials Science and Engineering: A, 361(1-2):377–384, 2003.

[72] T Y Tsui, W C Oliver, and G M Pharr. Influences of stress on the measurement of mechanical properties using nanoindentation: Part i. experimental studies in an aluminum alloy. Journal of Materials Research, 11(3):752–759, 1996.

[73] B Beucia, S Queyreau, C Kahloun, D Chaubet, P Franciosi, and B Bacroix. Plastic strain-induced grain boundary migration (SIBM) in pure aluminum: SEM in-situ and AFM examinations. International Journal of Plasticity, 115:29–55, 2019.

[74] P J Wolcott, A Hehr, C Pawlowski, and M J Dapino. Process improvements and characterization of ultrasonic additive manufactured structures. Journal of Materials Processing Technology, 233:44–52, 2016.

[75] G W Critchlow and D M Brewis. Review of surface pretreatments for aluminium alloys. International Journal of Adhesion and Adhesives, 16(4):255–275, 1996.

[76] A G Truog. Bond improvement of Al/Cu joints created by very high power ultrasonic additive manufacturing. PhD thesis, The Ohio State University, 2012.

[77] H R Le and M P F Sutcliffe. Analysis of surface roughness of cold-rolled aluminium foil. Wear, 244(1-2):71–78, 2000.

[78] B Bhushan. Introduction to tribology. John Wiley & Sons, 2013.

[79] K Johnson. Interlaminar subgrain refinement in ultrasonic consolidation. PhD thesis, Loughborough University, 2008.

[80] H Ramasawmy and L Blunt. Effect of edm process parameters on 3d surface topography. Journal of Materials Processing Technology, 148(2):155–164, 2004.

[81] L Slatineanu, S Potarniche, M Coteata, I Grigoras, L Gherman, and F Negoescu. Surface roughness at aluminium parts sand blasting. Proceedings in Manufacturing Systems, 6(2):69–74, 2011.

[82] R J Mills. Abrasive Blasting with Post-Process and In-Situ Characterization. PhD thesis, Virginia Tech, 2014.

[83] C Y Kong, R C Soar, and P M Dickens. Characterisation of aluminium alloy 6061 for the ultrasonic consolidation process. Materials Science and Engineering: A, 363(1-2):99–106, 2003.

[84] I E Gunduz, T Ando, E Shattuck, P Y Wong, and C C Doumanidis. Enhanced diffusion and phase transformations during ultrasonic welding of zinc and aluminum. Scripta Materialia, 52(9):939–943, 2005.

[85] X Cheng and X Li. Investigation of heat generation in ultrasonic metal welding using micro sensor arrays. Journal of Micromechanics and Microengineering, 17(2):273, 2007.

[86] S Yadav and C Doumanidis. Thermomechanical analysis of an ultrasonic rapid manufacturing (urm) system. Journal of Manufacturing Processes, 7(2):153–161, 2005.

[87] M R Sriraman, M Gonser, H T Fujii, S S Babu, and M Bloss. Thermal transients during processing of materials by very high power ultrasonic additive manufacturing. Journal of Materials Processing Technology, 211(10):1650–1657, 2011.

[88] E De Vries. Mechanics and mechanisms of ultrasonic metal welding. The Ohio State University, 2004.

[89] D Schick, S S Babu, D R Foster, M J Dapino, M Short, and J C Lippold. Transient thermal response in ultrasonic additive manufacturing of aluminum 3003. Rapid Prototyping Journal, 2011.

[90] A Purwanto, R I Wisnuwijaya, E K Sari, and W S B Dwandaru. Non-contact temperature measurement based on wien's displacement law using a single webcam in the infrared spectrum region. Physics Education, 55(2):025017, 2020.

[91] M A Khan, N H Madsen, and B A Chin. Infrared thermography as a control tor the welding process. In Thermosense VI: Thermal infrared sensing for diagnostics and control, volume 0446, pages 154–163, 1984.

[92] M Speka, S Matteï, M Pilloz, and M Ilie. The infrared thermography control of the laser welding of amorphous polymers. NDT and E International, 41(3):178–183, 2008.

[93] J D Seidt and A Gilat. Plastic deformation of 2024-T351 aluminum plate over a wide range of loading conditions. International Journal of Solids and Structures, 50(10):1781–1790, 2013.

[94] G Venkatraman, A Hehr, L M Headings, and M J Dapino. Effect of system compliance on weld power in ultrasonic additive manufacturing. Rapid Prototyping Journal, 2021.

[95] D Yi, S Zhang, H Zhang, L Zheng, and M Norfolk. Power consumption and friction coefficient in the ultrasonic consolidation of aluminium alloys. Materials Science and Technology, 33(6):744–750, 2017.

[96] A Yevtushenko and P Grzes. Finite element analysis of heat partition in a pad/disc brake system. Numerical Heat Transfer, Part A: Applications, 59(7):521–542, 2011.

[97] A A Ward, Y Zhang, and Z C Cordero. Junction growth in ultrasonic spot welding and ultrasonic additive manufacturing. Acta Materialia, 158:393–406, 2018.

[98] A Rusinek and J R Klepaczko. Experiments on heat generated during plastic deformation and stored energy for trip steels. Materials & Design, 30(1):35–48, 2009.

[99] D Pal and B Stucker. A study of subgrain formation in al 3003 h-18 foils undergoing ultrasonic additive manufacturing using a dislocation density based crystal plasticity finite element framework. Journal of applied physics, 113(20):203517, 2013.

[100] A Chamanfar, M T Alamoudi, N E Nanninga, and W Z Misiolek. Analysis of flow stress and microstructure during hot compression of 6099 aluminum alloy (AA6099). Materials Science and Engineering: A, 743:684–696, 2019.

[101] T Han, C Kuo, N Sridharan, L M Headings, S S Babu, and M J Dapino. Effect of weld power and interfacial temperature on mechanical strength and microstructure of carbon steel 4130 fabricated by ultrasonic additive manufacturing. Manufacturing Letters, 25:64–69, 2020.

[102] H R Le, M P F Sutcliffe, P Z Wang, and GT Burstein. Surface oxide fracture in cold aluminium rolling. Acta Materialia, 52(4):911–920, 2004.

[103] M M Nagl, S R J Saunders, and V Guttmann. Experimental data on oxide fracture. Materials at High Temperatures, 12(2-3):163–168, 1994.

[104] J C Grosskreutz. Mechanical properties of metal oxide films. Journal of the Electrochemical Society, 116(9):1232, 1969.